SEARCH FOR A SUPERSYMMETRIC PARTNER TO THE TOP QUARK USING A MULTIVARIATE ANALYSIS TECHNIQUE

by

SMITA DARMORA

Presented to the Faculty of the Graduate School of
The University of Texas at Arlington in Partial Fulfillment
of the Requirements
for the Degree of

DOCTOR OF PHILOSOPHY

THE UNIVERSITY OF TEXAS AT ARLINGTON
August 2015

To my parents.

ACKNOWLEDGEMENTS

This journey would not have been possible without the support, patience and guidance of the following people. It is to them that I owe my sincere gratitude.

First and foremost, I wish to express my deepest gratitude to my advisor, Dr. Kaushik De, for his excellent guidance, caring, patience and providing me with an excellent atmosphere for doing research. His guidance, insight, and encouragement were critical for the successful completion of this study.

I would like to thank my committee members Dr. Andrew P. White, Dr. Zdzislaw Musielak, Dr. Amir Farbin, Dr. Giulio Usai and Dr. Margherita Primavera for their continual support and guidance throughout this dissertation. I also wish to remember late Dr. Nail Fazleev who served as a committee member in my comprehensive exam and gave me valuable advises for my research. I also would like to thank the physics department and the High Energy Physics (HEP) group at UTA for providing me an excellent work environment and support throughout this journey.

I owe a great debt of gratitude to Dr. Giulio Usai for his patience and guidance throughout my journey at CERN. The work in this thesis owes great deal to many people in ATALS SUSY group. In particular I would like to thank Dr. Margherita Primavera and the members of INFN research group for being very helpful throughout my research work. Their valuable suggestions during our regular research meetings have enriched my research experience. My time at CERN was also enriched by the friends and the group that became a part of my life.

This journey would not have been possible without the support of my family and friends. To my family, thank you for encouraging me in all of my pursuits and

inspiring me to follow my dreams. To my friends, thank you for listening, offering me advice, and supporting me through this entire process. I would never forget all the chats and beautiful moment I shared with my friends and classmates.

Finally, I must express my very profound gratitude to my husband Parmanand for providing me continuous support and encouragement throughout my doctoral study. This accomplishment would not have been possible without you. Thank you.

May 5, 2015

ABSTRACT

SEARCH FOR A SUPERSYMMETRIC PARTNER TO THE TOP QUARK USING A MULTIVARIATE ANALYSIS TECHNIQUE

Smita Darmora, Ph.D.

The University of Texas at Arlington, 2015

Supervising Professor: Kaushik De

Supersymmetry (SUSY) is an extension to the Standard Model (SM) which introduces supersymmetric partners of the known fermions and bosons. Top squark (stop) searches are a natural extension of inclusive SUSY searches at the Large Hadron Collider (LHC). If SUSY solves the naturalness problem, the stop should be light enough to cancel the top loop contribution to the Higgs mass parameter. The 3rd generation squarks may be the first SUSY particles to be discovered at the LHC.

The stop can decay into a variety of final states, depending, amongst other factors, on the hierarchy of the mass eigenstates formed from the linear superposition of the SUSY partners of the Higgs boson and electroweak gauge bosons. In this study the relevant mass eigenstates are the lightest chargino ($\chi_1^{\pm}$) and the neutralino (χ_1^0). A search is presented for a heavy SUSY top partner decaying to a lepton, neutrino and the lightest supersymmetric particle (χ_1^0) , via a b-quark and a chargino ($\chi_1^{\pm}$) in events with two leptons in the final state. The analysis targets searches for a SUSY top partner by means of a Multivariate Analysis Technique, used to discriminate between the stop signal and the background with a learning algorithm based on Monte Carlo

generated signal and background samples. The analysis uses data corresponding to 20.3 fb^{-1} of integrated luminosity at $\sqrt{s} = 8$ TeV, collected by the ATLAS experiment at the LHC in 2012.

TABLE OF CONTENTS

LIST OF FIGURES

LIST OF TABLES

CHAPTER 1

Theoretical Overview

1.1 Introduction and Motivation

The Standard Model (SM) of elementary particle physics constitutes the most accurate mathematical description of matter and their interactions which exists today. The behavior of all known subatomic particles can be described within a single theoretical framework called the SM. Developed in the early 1970's, it has been superbly confirmed by experimental data and has precisely predicted a wide variety of phenomena. The most obvious and current example of this is of course the recent discovery of the Higgs boson. This model incorporates the quark and leptons as well as their interactions through the strong, weak and electromagnetic forces. Only gravity remains outside the SM. Aside from omitting gravity, it's a complete theory of what we see in nature.

But, it does not answer all the questions that may raise about the fundamental interactions. Despite its incredible success, the SM has serious deficiencies. The SM offers no explanation of one of the four known forces of nature, gravity. There is no prediction of a particle that would constitute a suitable candidate for dark matter (DM). The SM also does not predict the values or origin of many of its parameters, and thus they can only be measured experimentally . The SM also offers no solution to the hierarchy problem.

The SM, being an "effective field theory", is valid at energy up to the Planck scale, at which gravity is expected to become comparable in strength to the other forces. Since gravity is not yet included in the SM, the theory will have to be gen-

eralized to include it. There are however some compelling reasons to believe that new physics might already appear at much lower scales that have become experimentally accessible in recent years with the start of proton-proton collisions in the Large Hadron Collider (LHC) experiments. One well-motivated extension of the SM is the idea of Supersymmetry (SUSY), which elegantly attempts to shed light on and cure many of the SM limitations. It introduces a symmetry between fermionic and bosonic particles and treats matter and forces identically. A supersymmetric theory is one in which the equations for force and equations for matter are identical. The crucial feature is: for every known matter particle a theory that includes SUSY predicts a new force particle and vice versa. The equations that contains SUSY explain the mysteries left by the SM like explaining why gravity is so much weaker than the other forces, why the Higgs bososn exists and even provides the possible source of the dark matter that seems to govern mystifies how all the galaxies rotate.

The Higgs boson is the detectable signature of the Higgs field which is an energy field that gives fundamental sub-atomic particles their mass. The problem is that it's hard to understand why the Higgs boson has the mass it has. From quantum mechanics the most reasonable value predicted by the SM for the mass of the Higgs boson is very large. If SUSY is real, one of the effects of extra particles predicted by the theory is that they can cancel out the very large value seen in the traditional theory. This leads to a prediction of the mass of the Higgs boson that agrees what has been observed. Another problem that a SUSY theory solves pertains to the unification of the four fundamental forces. There are reasons to believe that three forces we understand at the sub-atomic level might be different aspect of single unified force. One reason to believe this is the strength of these forces, Electromagnetic (EM), strong and weak nuclear vary as a function of the energy as we study them. Using the SM, we can predict how the strengths of these forces change when we find that at

very high energies they become similar. But the strengths of the forces do not become equal at a single energy. In contrast, if we do the same exercise using a theory that includes SUSY we find that the three forces are unified to a common strength at a single energy. Astronomers have long known that the galaxy spins faster that we can explain with known physics and galaxy masses. To address this issue scientist postulate a new kind of matter known as dark matter (DM). The difficulty is we have so far not directly observed DM. However, SUSY theories predict the series of partner particles to those familiar from the particles of the SM. The lightest SUSY particle called the Lightest Supersymmetric Particle (LSP), has exactly the same properties of the proposed DM particle.

Despite the accuracy of the SM, there are unresolved issues such as a lack of understanding of gravity at the quantum level and the mysterious nature of dark matter. In addition it's not an entirely satisfactory theory, because it has a number of arbitrary elements. For example, there are many parameters in the SM that appear in the equations, and they must be inserted by hand to make the theory fit the observation. For example, the mass of the electron, the masses of the quarks, the charge of the electron, and so forth.

1.2 Standard Model (SM)

The primary objective of particle physics is to understand the basic structure and laws of nature all the way from the largest dimensions in the universe (formation of stars and galaxies) all the way down to the smallest micro-scales. The SM of particle physics attempts to categorize all the known sub-atomic particle into groups in the same way as is done in the periodic table categorize atoms. It is a collection of renormalizable gauge quantum field theories, which can explain most of the current experimental observations as well as some cosmological phenomena in the early uni-

verse. It has been extremely successful at describing a large spectrum of experimental data across a broad range of energies.

The SM treats all of the fundamental particles as point-like entities with an internal angular momentum quantum number, spin, which classifies them into two different categories; fermions with half-integer spin and bosons with integer spin. Fermions are the constituents of matter, whilst bosons are the force carriers that mediate interactions between fermions.

1.2.1 Matter Particles

The fermions, with half integral spin, cannot exist in same space at the same time in accordance with the Pauli exclusion principle and are described by Fermi Dirac statistics. Depending on the interaction with the strong nuclear force, fermions are divided into two categories. Particles which experience this force are known as quarks. The second set of fermions are leptons, which do not interact with the strong nuclear force. Table 1.1 shows the categorization of quarks and leptons, along with their fundamental properties. The quarks and leptons are organized into three generations which are denoted by I, II and III. Each generation appears to be identical in every respect other than the particle masses. The masses of fermions increase with each generation and are grouped according to their left- and right-handed chirality states.

The three generation of quarks are up and down quarks, the charm and strange quarks, and the top and bottom quarks. All of the quarks in the universe are of the lightest two varieties, the up quark and down quark, which form the building blocks for protons and neutrons. Quarks always bind into more complex entities called mesons or baryons, collectively known as hadrons. Mesons are intermediate mass particles which are consist of a quark-antiquark pair, while three quark combinations are called baryons. Baryons are fermions, Mesons are bosons. Each of the six "flavors" of quarks

Table 1.1: The Standard Model fermions, spin-1/2 particles with their corresponding masses (particle data group). Interactions between these particles are mediated by the gauge bosons shown in table 1.2

Particle type	Generation	Name	Symbol	Charge (e)	Mass
Quarks (spin=1/2)	I	up	u	+2/3	2.3 MeV
		down	d	-1/3	4.8 MeV
	II	charm	c	+2/3	1.275 GeV
		strange	s	-1/3	95 MeV
	III	top	t	+2/3	173.07 GeV
		bottom	b	-1/3	4.18 GeV
Leptons (spin=1/2)	I	electron	e	-1	0.511 MeV
		electron neutrino	ν_e	0	<2 eV
	II	muon	μ	-1	105.7 MeV
		muon neutrino	ν_μ	0	<0.19 MeV
	III	tau	τ	-1	1.777 GeV
		tau neutrino	ν_τ	0	<18.2 MeV

can have three different "colors", which is the strong interaction analog to charge in the EM force. The quark forces are attractive only in "colorless" combinations of baryons and mesons.

Leptons are members of a class of fermions that respond only to EM, weak, and gravitational forces; with a half-integral spin. Leptons can either carry one unit of electric charge or be neutral. Six leptons are known, subdivided further into three generations each containing one charged lepton and one neutrino. The charged leptons are the electron (e), muon (μ), and tau (τ). While the electron is stable, the other two charged leptons (muon and tau) have finite lifetimes and decay via the weak interaction. Each charged lepton has an associated neutral partner, or neutrino (i.e., electron-, muon-, and tau-neutrino).

1.2.2 Forces

The universe exists because of the fundamental particle interactions. These interactions include attractive and repulsive forces, decay and annihilation. These can be categorized into macroscopic EM, gravitational forces, and the microscopic weak and strong forces. Table 1.2 summaries the three forces, showing the mass and charge properties of their corresponding mediating particles(s). The SM does not include gravitation because of its negligible force and the extremely small masses of the particles. The three forces of the SM are typically represented by a specific quantum number. The quantum number of the electromagnetic force is the electric charge, Q. The weak force has the weak isospin, T, while the strong force is connected to color charge, C. The SM is associated with the local symmetry operations of a Lie group and the interactions between two fermions are described by the exchange of intermediary particles with integer spin, called "bosons". The force mediators are the photon (γ) for EM interactions, the gluon for strong interactions and the $W^{\pm}$ and Z bosons for weak interactions. Gluons possess color charge while the $W^{\pm}$ and Z bosons carry weak isospin. Therefore these particles not only mediate the force, but interact among themselves, which leads to more complex phenomenologies compared to those observed in electromagnetism. All the forces are described in more detail in the following sections, together with their intermediary (or "gauge") bosons.

1.2.2.1 Electromagnetic Force

The theory of electromagnetism, called Quantum Electrodynamics (QED), was the first properly formulated and simplest formulation of quantum field theory. This is because the set of gauge transformations commute and therefore, the generators are Abelian. In group theory these transformations are said to belong to the $U(1)_Q$ gauge group, which means that the mediating gauge bosons in QED have no self coupling.

Table 1.2: The Standard Model bosons, integer-spin particles, with their corresponding masses (particle data group). These particles mediate intersection between the fermions in table 1.1

Force	Name	Symbol	Mass	Charge
Elecromagnetic	Photon	γ	0	0
Weak	W boson	$W^{\pm}$	80.38 GeV	1
	Z boson	Z	91.19 GeV	0
Strong	Gluons	g	0	0

The QED electromagnetic Lagrangian, $\mathcal{L}_{QED}$, describing a fermion ψ of mass m is given by:

$$\mathcal{L}_{QED} = \bar{\psi}(i\gamma^{\mu}D_{\mu} - m)\psi - \frac{1}{4}F^{\mu\nu}F_{\mu\nu} \tag{1.1}$$

The covariant derivative D_{μ} replaces the partial derivative to maintain the local $U(1)_Q$ gauge invariance, as shown in equation 1.2. This new covariant derivative introduces a new "gauge field", A_{μ}, which is connected with the Dirac field ψ.

$$\partial_{\mu} \rightarrow D_{\mu} = \partial_{\mu} + iqA_{\mu} \tag{1.2}$$

Here q is the charge of the fermion under consideration. A electromagnetic field term $F^{\mu\nu}F_{\mu\nu}$, where $F^{\mu\nu}F_{\mu\nu} = \partial^{\mu}A^{\nu} - \partial^{\nu}A^{\mu}$, describes the dynamics of the gauge field A_{μ}. The Abelian structure $U(1)_Q$ does not allow any self intersection terms for the photon field.

1.2.2.2 The Strong Interaction

The strong intersection between quarks, are formulated in the framework of quantum field theory, which we call Quantum Chromodynamics (QCD). In QCD the defining symmetry is $SU(3)_c$, the group of special unitary transformations in three

dimensions where the c stands for the color, a name for the charge related to the strong intersection. Imposing local gauge invariance under the non-Abelian $SU(3)_c$ transformations of quark states introduces the 8 gauge fields that corresponds to the 8 gluon color state. The Lagrangian is given by $\mathcal{L}_{QCD}$, of similar form of QED:

$$\mathcal{L}_{QCD} = \sum_n \bar{\psi}_n^a (i\gamma^\mu D_\mu - m_n)\psi_n^a - \frac{1}{4} G_{\mu\nu}^\alpha G_\alpha^{\mu\nu} \tag{1.3}$$

where the index α runs from 1 to 8, with the gluon gauge field strength tensor, $G_{\mu\nu}^\alpha$. γ^μ are Dirac matrices, m is the mass of quark and D_μ is the covariant derivative. The index n runs over all the quark flavors (u,d,c,s,t,b) and a labels the color charge: red, blue and green. In order to ensure gauge invariance for the fermion kinetic term, the derivative ∂_μ has to be promoted to a covariant derivative,

$$D_\mu = \partial_\mu + i g_s A_\mu^\alpha \lambda_\alpha \tag{1.4}$$

and gauge vector fields A_μ^α need to be introduced. The new gauge field have their own gauge invariant kinetic term associated with them, in which the field strength tensor is defined by

$$G_{\mu\nu}^a = \partial_\mu A_\nu^\alpha - \partial_\nu A_\mu^\alpha - g_s f^{ijk} A_\mu^j A_\nu^k \tag{1.5}$$

The λ_α are the generators of the $SU(3)_C$ group and the f^{ijk} are the structure constants of the group: $[\lambda_\alpha, \lambda_\beta] = i f_{\alpha\beta\gamma}^\gamma$. It is this non-Abelian nature which allows for gluon-gluon self interaction.

1.2.2.3 Weak Force and Electroweak Unification

The final force in the SM is the weak force, where the weak interaction is small at low momentum transfer compared to strong and EM interaction. Theory of the weak

force can be obtained by requiring that the Lagrangian describing the interactions of left handed fermion doublets be invariant under $SU(2)_L$ in the space of weak isospin, I.

The EM and weak interactions are two different aspects of unified electroweak interaction with the gauge group $SU(2)_L \times U(1)_Y$ where the gauge group $U(1)_Y$ is that of weak hypercharge Y. This is related to the $U(1)_Q$ symmetry group of QED by $Y/2 = Q - I_3$, where Q is the electric charge and I_3 is the third component of weak isospin. The electroweak Lagrangian is given by

$$\mathcal{L}_{EW} = \bar{\psi}(i\gamma^\mu D_\mu - m)\psi - \frac{1}{4}W^{\mu\nu}.W_{\mu\nu} - \frac{1}{4}B^{\mu\nu}.B_{\mu\nu} \tag{1.6}$$

where ψ are the left-handed doublets and right-handed singlets. Right handed neutrinos have not been observed in nature and are hence omitted.

$$\psi_{leptons} = \begin{pmatrix} \nu_L^e \\ e_L \end{pmatrix}, e_R, \begin{pmatrix} \nu_L^\mu \\ \mu_L \end{pmatrix}, \mu_R, \begin{pmatrix} \nu_L^\tau \\ \tau_L \end{pmatrix}, \tau_R \tag{1.7}$$

$$\psi_{quarks} = \begin{pmatrix} u_L \\ d_L \end{pmatrix}, u_R, d_R, \begin{pmatrix} c_L \\ s_L \end{pmatrix}, c_R, s_R, \begin{pmatrix} t_L \\ b_L \end{pmatrix}, t_R, b_R \tag{1.8}$$

Maintaining the gauge invariance under $SU(2)_L \times U(1)_Y$ required the introduction of the weak vector fields, W_μ and the hypercharge vector field, B_μ (Equation 1.6) via the covariant derivative:

$$D_\mu = \partial\mu + ig_W\tau W_\mu + ig_Y\frac{Y}{2}B_\mu \tag{1.9}$$

where g_W and g_Y are coupling constants for each respective field and τ represents the generators of the $SU(2)_L$ group. The corresponding gauge fields $W_\mu^\pm$, Z_μ and A_μ are linear combinations of the weak and hyperchage fields.

$$W_\mu^\pm = \frac{1}{\sqrt{2}}(W_\mu^1 \pm iW_\mu^2) \tag{1.10}$$

$$Z_\mu = cos\theta_W W_\mu^3 - sin\theta_W B_\mu \tag{1.11}$$

$$A_\mu = sin\theta_W W_\mu^3 - cos\theta_W B_\mu \tag{1.12}$$

where θ_W is the experimentally determined weak mixing angle defined as a ratio of the electrweak coupling constants g and g' ($tan\theta_W = g/g'$) and A_μ is associated photon field.

1.2.3 Electroweak Symmetry Breaking

A combination of theories of the electroweak and strong interaction may be done to form a unified theory of all fundamental forces apart from gravity. It can be described by the invariance of massless fields $SU(3)_C \times SU(2)_L \times U(1)_Y$ transformations, where all the gauge bosons responsible for mediating the forces are considered massless. This is not a problem for the gluon and photon, which mediate long range forces and must be massless. Experimentally, however, it has been shown that the $W_\pm$, Z and fermions are indeed massive. Therefore, in order to validate the SM assumption, the electroweak sector symmetry must be broken.

The mechanism of spontaneous electroweak symmetry breaking applied to a nonabelian theory was introduced by Peter Higgs [7] in 1964, and independently by Robert Brout and Francoise Englert [8], and Gerald Guralnik, C. R. Hagen, and Tom

Kibble [9] [10]. It provides a solution to the massless fields, commonly known as the Higgs mechanism.

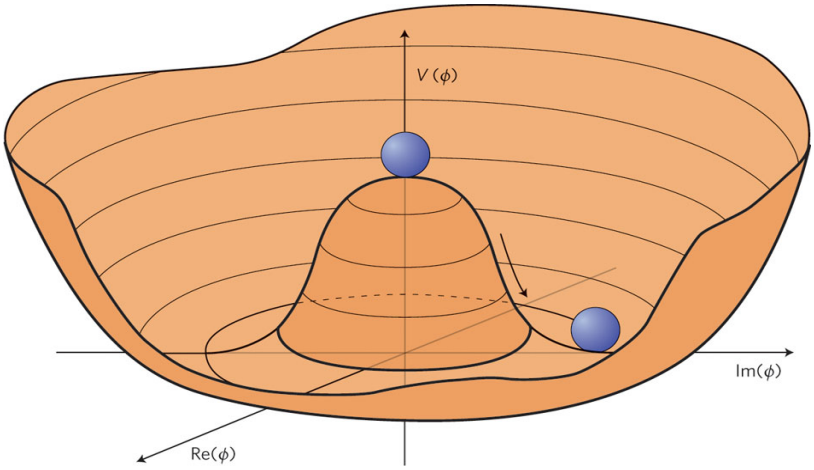

Figure 1.1: The shape of Higgs potential $V(\phi)$ in the complex (ϕ_1, ϕ_1) plane. The lowest-energy state is described by a randomly chosen point around the bottom.

The Higgs mechanism introduces a boson field, known as Higgs field, with non-zero weak isospin and weak hypercharge interacting with particles (boson and fermions). This mechanism is used to explain the masses of fermions and weak bosons. A complex scalar field (two degrees of freedom) can be written as

$$\phi = \frac{\phi_1 + i\phi_2}{\sqrt{2}} \tag{1.13}$$

with a Lagrangian density (equation 1.14) and an associated potential (equation 1.15),

$$L = (\partial_\mu \phi)^* (\partial_\mu \phi) - V(\phi) \tag{1.14}$$

$$V(\phi) = \mu^2 |\phi|^2 + \lambda |\phi|^4 \tag{1.15}$$

The first term in the Lagrangian denotes the kinematic part of the field, which contains the interaction between the field ϕ and gauge bosons of the group $SU(2)_L \times U(1)_Y$. The second term in the Lagrangian is the potential of the field ϕ, which is invariant under the gauge transformation $SU(2)_L$. If the μ and λ constants in equation 1.15 are assumed to be real, the $V(\phi)$ potential has the shape shown in figure 1.1. The term μ^2 can be understood as mass of the field ϕ, and λ is considered as the self-coupling of the field ϕ. There are two possibilities of the term μ^2 that can alter the behavior of the potential $V(\phi)$:

- $\mu^2 > 0$: The equilibrium state where $V = 0$ can only be found at $\phi = 0$, with only one Vacuum Expectation Value (VEV) of the Higgs field, is a circle on the complex plane of radius $|\phi_0|$, which is nonzero. The potential is symmetric, and no symmetry breaking is observed.
- $\mu^2 < 0$: the equilibrium state of V can be located anywhere as long as the value of the field satisfies $< \phi_{VEV} >= -\frac{\mu^2}{2\lambda}$. In this case symmetry is broken called spontaneous symmetry breaking, a mechanism where there is a symmetric Lagrangian, but not a symmetric VEV.

The VEV of the Higgs field is not invariant under gauge transformations and so spontaneously breaks the gauge symmetry, which means that the symmetry is preserved in the model but not the ground state of vacuum. This mechanism gives mass to the gauge bosons without violating gauge symmetry. The weak gauge bosons acquire mass by interacting with the Higgs field and fermions can acquire mass through Yukawa coupling to the Higgs field. The coupling constant and the mass can be different for each fermion.

In 2012, both the ATLAS [11] and CMS [12] collaborations at CERN showed evidence for the discovery of a scalar boson at a mass of 125.6 GeV, consistent with the SM Higgs [13] [14].

1.2.4 Shortcomings of the Standard Model

The SM has produced a large number of predictions which have been experimentally verified. Despite the success of the SM, many fundamental questions remain unanswered. It is not known why there are three generations of fermions or why the masses of the quarks differ by order of magnitude. Another problem is that many phenomena, such as electroweak mixing and CP violation, are determined by free parameters, which have to be fixed by experiment. Gravity is not incorporated in the SM and despite the evidence for DM, it does not postulate any candidate. Finally, the theory contains a potentially disastrous hierarchy problem, discussed here.

1.2.4.1 The Hierarchy Problem

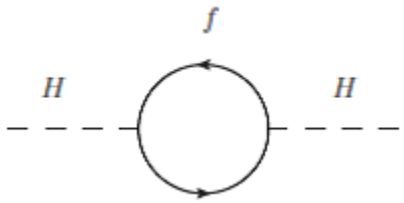

Figure 1.2: Radiative correction to the Higgs mass due to a Dirac fermion

The Higgs mass is one of the 19 free parameters of the SM, dependent on the curvature of the scalar potential at the vacuum minimum. The mass of the Higgs receives divergent radiative corrections from virtual effects of all particles that couple to the Higgs field. Radiative corrections from Feynman diagrams are depicted in figure 1.2. When computing the mass to second and higher orders, considering radiative corrections via loop diagrams, all particles which couple to the Higgs must be considered. The relevant Lagrangian contains the term $-\lambda_f H \bar{f} f$ and the corresponding

corrections to Higgs mass, m_H^2, due to loops, such as the diagram shown in figure 1.2, is given by

$$\Delta m_H^2 = \frac{|\lambda_f|^2}{16\pi^2}[-2\Lambda_{UV}^2 + 6m_f^2 ln(\Lambda_{UV}/m_f) + ...] \tag{1.16}$$

where λ_f is the fermion Yukawa coupling and Λ_{UV} is the ultraviolet momentum cut-off used to regulate the loop integral. The largest contributions comes from the top quark as $\lambda_f \simeq 1$. If Λ_{UV}^2 is of the order of the Planck scale, then the quantum corrections to m_H^2 are of order 10^{34} GeV. In other words, the mass of the Higgs will not be at electroweak scale but much more massive. Therefore, in order to achieve a Higgs boson mass at the electrweak scale (125.6 GeV), cancellations in the various contributions to m_H^2 must be precise. The requirement for this seemingly very unnatural level of cancellation is referred to as the hierarchy problem.

1.3 Supersymmetry (SUSY)

Several theories exist that provide extension to the SM in order to solve some of the issues described in the previous section. Example of such theories are Large Extra Dimensions [15] and Kaluza-Klein models. However, the focus of this section is dedicated to the theory of Superymmetry [16] [17] [18] [19] [20] [21] and [22] . All these introduce new physics at around the TeV scale.

SUSY postulates a new symmetry between fermions and bosons such that every SM boson has a fermionic "super-partner", and every SM fermion a bosonic super-partner. These SUSY particles, or sparticles, should be identical to their SM counterparts in every way, except for this difference in spin. If the masses of the additional particles are small enough they allow for the fermionic and scalar Higgs interactions to cancel out, which stabilizes the Higgs mass and hence solves the hierarchy problem. SUSY also provides a candidate for dark matter as well as a means

of unifying the fundamental forces below Planck scale. A summary of the SUSY particles is given in table 1.3.

SUSY invokes quantum field theory, and it leads to the introduction of two sets of fields based upon the gauge theory. Chiral fields associated with the SM fermions produce their bosonic SUSY counterparts. The nature of this field results in left-handed and right-handed fermions being treated differently, with right-handed fermions becoming members of these chiral fields by way of their charge conjugate. This results in the two projections being treated as separate particles in SUSY. In the case of the SM bosons, vector fields link with the associated fields of the SM gauge bosons to produce fermionic superpartners.

If SUSY were an exact symmetry, sparticles would have the same masses as their SM partners. However, no sparticles have been observed, therefore, SUSY must be a broken symmetry. To ensure that the theory still solves the hierarchy problem, the relationships between couplings must also remain unchanged. This can be achieved with the "soft" SUSY breaking mechanism, in such a way that the sparticles are not too heavy to avoid re-introducing the hierarchy problem and still able to solve the shortcomings within the SM. This breaking mechanism imposes constraints on the masses of all superpartners and sets them to a phenomenologically suitable range.

1.3.1 Addressing the Hierarchy Problem

A natural introduction to SUSY comes in the context of the hierarchy problem. In equation 1.16, the contribution to m_H^2 from fermion loops are given. Similar contribution comes from a massive complex of the form

$$\Delta m_H^2 = \frac{|\lambda_s|^2}{16\pi^2}[\Lambda_{UV}^2 - 2m_s^2 ln(\Lambda_{UV}/m_s) + ...] \tag{1.17}$$

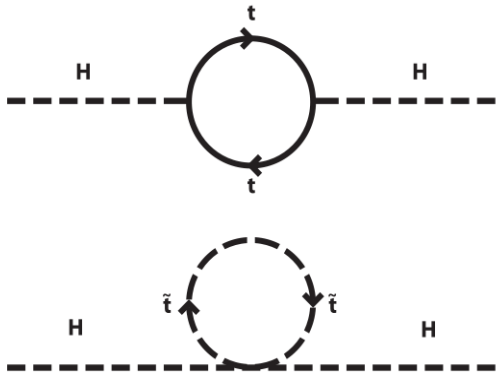

Figure 1.3: Radiative correction to the Higgs mass due to a Dirac fermion f (top), and a Scalar S (bottom).

where λ_s is the Higgs to scalar coupling of the particle with mass m_s. The form of the leading terms in equation 1.16 and 1.17 indicates that, if two scalars existed for each fermion, then the divergent parts of the equation would cancel out. The corresponding Feynman diagram for these fermion and scalar contributions are shown in figure 1.2 and 1.3. The naturalness of this cancellation is preserved provided the difference in mass between SM particles and their superpartners is not beyond $\mathcal{O}(1)$ TeV.

1.3.2 Unification and R-Parity

SUSY has some other beneficial implications. The requirement of a Grand Unified Theory (GUT), which unifies all of the fundamental forces [23], adds credence to SUSY. Therefore, the forces are manifest as distinct entities simply because this unification occurs at a very high energy scale. The evolution of each of the couplings in the SM is shown by the dashed lines in figure 1.4. Within the SM, when the running of coupling constants is extrapolated upwards, they almost meet at around 10^{15} GeV, but do not converge. However, the new particles predicted by SUSY cause the evolution of the running couplings to change. Figure 1.4 (solid lines) shows that

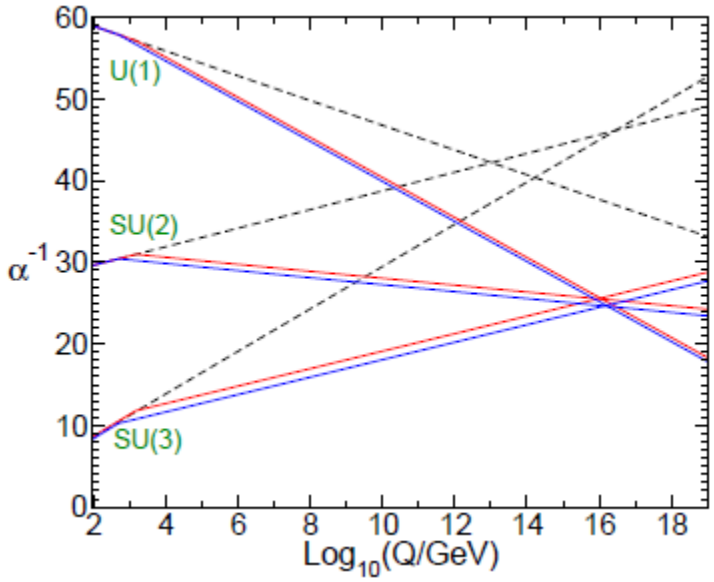

Figure 1.4: The evolution of the gauge coupling in the Standard Model (dashed line) and the MSSM solid lines.

the additional particle content of the MSSM has just the right effect on the evolution of the couplings that close to perfect unification occurs at $\sim 10^{16}$ GeV.

Theories like SUSY are constructed by specifying the particle content and symmetries, from which all the different terms of the Lagrangian can be obtained, which gives rise to lepton and baryon number violating terms. The inclusion of all such terms in the model would lead to proton decay, on which very stringent experimental limits exist [24]. One way such processes can be avoided is by imposing the requirement that R-parity (R_P), is conserved. The result of this ad-hoc requirement is that all lepton number violating terms in the supersymmetric Lagrangian are disallowed. R-Parity is defined as follows:

$$P_R = (-1)^{3(B-L)+2s} \tag{1.18}$$

where s, B and L refer to spin, baryon number and lepton number respectively. it is clear that SM particles have $R_P = +1$ and SUSY particles $R_P = -1$. The advantage of R-parity is that it can in principle be an exact and fundamental symmetry, which B and L themselves cannot while still preventing terms with an odd number of leptons of quarks. Two important consequences of R-parity conservation are the fact that SUSY particles need to be pair-produced, and that the LSP must be stable. The fact that no such stable SUSY particle has been observed implies that it must be neutral and weakly interacting. Thus, R-parity conserving SUSY predicts a stable massive neutral weakly-interaction particle, which is the required properties for a Dark Matter candidate. Such a particle would not interact with the ATLAS detector and therefore would result in substantial missing transverse momentum in an event.

1.3.3 Minimal Supersymmetric Standard Model (MSSM)

The minimal Supersymmetric Standard Model (MSSM), is the minimum set of fields and interactions necessary for a consistent SUSY theory that can reproduce the SM phenomenology [25] [26] [27] [28] [29] [30]. It solves the hierarchy problem exactly, at the cost of almost doubling the particle content of the SM. The physically observable mass states are formed from mixing the available supersymmetric states. The MSSM particle content is listed in table 1.3.

In the case of bosonic fields, each of the vector bosons and the SM Higgs have a fermionic superpartners which are jointly refereed to as gauginos and Higgsino (H_u and H_d), respectively. There are two complex Higgs doublets, rather than just one as in the SM, are

$$H_u = \begin{pmatrix} H_u^+ \\ H_u^0 \end{pmatrix}, \quad H_d = \begin{pmatrix} H_d^0 \\ H_d^- \end{pmatrix}; \tag{1.19}$$

Table 1.3: Supersymmetric particles in the MSSM.

Names	Spin	Gauge Eigenstates	Mass Eigenstates
squarks	0	$\tilde{u}_L\ \tilde{u}_R\ \tilde{d}_L\ \tilde{d}_R$	same
		$\tilde{s}_L\ \tilde{s}_R\ \tilde{c}_L\ \tilde{c}_R$	same
		$\tilde{t}_L\ \tilde{t}_R\ \tilde{b}_L\ \tilde{b}_R$	$\tilde{t}_1\ \tilde{t}_2\ \tilde{b}_1\ \tilde{b}_2$
sleptons	0	$\tilde{e}_L\ \tilde{e}_R\ \tilde{\nu}_e$	same
		$\tilde{\mu}_L\ \tilde{\mu}_R\ \tilde{\nu}_\mu$	same
		$\tau_L\ \tilde{\tau}_R\ \tilde{\nu}_\tau$	$\tilde{\tau}_1\ \tilde{\tau}_2\ \tilde{\nu}_\tau$
Higgs bosons	0	$\mathrm{H}_u^0\ H_d^0\ H_u^+\ H_d^-$	$\mathrm{h}^0\ H^0\ A^0\ H^\pm$
neutralino	1/2	$\tilde{B}_0\ \tilde{W}_0\ \tilde{H}_u^0\ \tilde{H}_d^0$	$\tilde{\chi}_1^0\ \tilde{\chi}_2^0\ \tilde{\chi}_3^0\ \tilde{\chi}_4^0$
chargino	1/2	$\tilde{W}_\pm\ \tilde{H}_u^+\ \tilde{H}_d^-$	$\tilde{\chi}_1^\pm\ \tilde{\chi}_2^\pm$
gluino	1/2	$\tilde{g}$	same
gravitino	3/2	$\tilde{G}$	same

with total eight degrees of freedom, three of which are lost in Electroweak symmetry breaking and give mass to the Z and $W_\pm$ boson of the SM. Therefore, there are five Higgs bosons in MSSM: h^0, H^0, H^+, H^-, A^0. The one that most closely resembles the Higgs bosons of the SM is h^0, which is the lightest of the five.

The neutral MSSM fermions, consisting of the neutral bino, wino and Higgsino ($\tilde{H}_u^0, \tilde{H}_d^0$), mix to form four neutral particles called neutralinos and denoted $\tilde{\chi}_1^0, \tilde{\chi}_2^0, \tilde{\chi}_3^0, \tilde{\chi}_4^0$. Similarly the charged higgsinos($\tilde{H}_u^+, \tilde{H}_d^-$) and winos ($\tilde{W}^\pm$) mix resulting in two charginos: $\tilde{\chi}_1^\pm, \tilde{\chi}_2^\pm$. In the squark sector the amount of mixing is proportional to the corresponding SM partner mass and is hence only non-negligible in the third

generation. The superpartners of the right and left handed stop ($\tilde{t}_L$ and $\tilde{t}_R$) mix to form the $\tilde{t}_1$ and $\tilde{t}_2$. Similarly sbottom $\tilde{b}_L$ and $\tilde{b}_R$ mix to form the $\tilde{b}_1$ and $\tilde{b}_2$. The same applies to sleptons and only staus ($\tilde{\tau}_L$ and $\tilde{\tau}_R$) mix significantly to form $\tilde{\tau}_1$ and $\tilde{\tau}_2$.

1.3.4 Supersymmetry Breaking

The MSSM is formulated by adding the fewest new particles to the SM, which contains 105 associated parameters with the minimal adjustments. This presents a challenge for making predictions regarding the nature and phenomenology of SUSY interactions. It is clear that the SUSY is a broken symmetry, if it exists at all. The MSSM can be refined further upon assuming that SUSY is broken due to fields as yet unobserved in the SM, which do not couple to the visible MSSM particles. Therefore it occurs in a hidden sector and the effects are propagated to the SUSY sector via some particle exchange. Some of the models based on this framework are described here. Each mechanism leads to a different phenomenology, and the models differ for example in the mass splitting between different particles, or the nature of the LSP.

The Minimal SuperGravity (mSUGRA) [31] [32] [33] [34] [35] [36] model explains how SUSY breaking could be communicated to the MSSM from the hidden sector. It is a gravity mediated model, where supergravity couplings of the fields in the hidden sector with the SM fields are responsible for the Soft Supersymmetry Breaking (SSB) terms. The introduction of mSUGRA constrains the MSSM greatly, reducing the number of associated parameters from 105 to 5. Therefore, the mSUGRA interpretation of the MSSM is referred as the constrained Minimal Supersymmetric Standard Model (cMSSM). Both the models, mSUGRA and cMSSM assume universality of the gaugino and sfermion masses at the high scale.

One of the models attempting to explain SUSY breaking is Gauge Mediated Supersymmetry Breaking (GMSB), where the SSB is transmitted to the low energy

world via a messenger sector through messenger fields which have gauge interactions. The squarks, sleptons and gauginos get their masses as a result of gauge interactions with the messenger particles, with the masses being determined by the strength of the gauge couplings and the SUSY mass scale.

Anomaly Mediated Supersymmetry Breaking (AMSB) models [37] [38] is a special case of gravity mediation, for which supergravity couplings that induce mediation are absent and the SSB is caused by loop effects. It is based on the fact that the conformal anomaly gives a general and model independent contribution to gaugino masses and generates the SSB terms. It is always present and can be the dominant contribution when there is no direct tree level coupling which transfers the SUSY breaking from the hidden sector to the observable sector.

1.3.5 Simplified Model

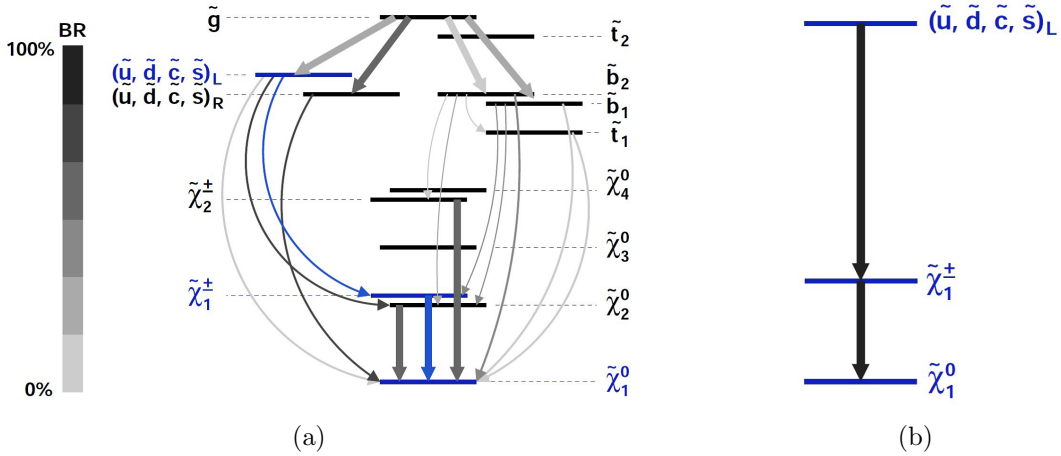

Figure 1.5: SUSY production process(a), with a simplified model decay chain (b)

The general MSSM has too many parameters to be practically scanned at any experiment. On the other hand, an extremely constrained model like cMSSM, assumes

gravity mediated SUSY breaking and imposes gaugino mass unification at a high scale, with universal scalar masses and universal trilinear couplings, thus reducing the SUSY parameter space to only 5 degrees of freedom. Large regions of the parameter space of this model have been excluded based on experimental constraints, and attention has turned to more general models.

A simplistic approach for SUSY breaking models is to focus on one or more SUSY production processes and their decay chain, which has the advantage of considering the minimal particle content necessary to reproduce such events. This opposite extreme in SUSY models complexity is referred to as a simplified model [39] [40], which considers only sparticles of interest, with all other sparticles usually being decoupled. Therefore a simplified model is not a fully SUSY model since only the parameters relevant to the single decay chain are considered.

Very strong assumptions are made in such models by placing the physical masses of most SUSY particles at a high scale of a few TeV, with only the LSP and one or two other particles kinematically accessible. The branching ratio for the process of interest are fixed at 100% and the gaugino or stop/sbottom mixing are ignored. The simplified model framework thus provides the possibility of studying the production of a certain particle and one of its decays only. This approach enables one to optimize searches for particular particles and particular decay chains.

Figure 1.5 shows a schematic representation of a SUSY production process and a example of a simplified process of interest. In the different SUSY models, there are a lot of different particles, all with different masses, with the heaviest gluions to the lightest neutralinos. The figure 1.5(a) shows how each one decays so that we get many sparticles with different masses and lot of different ways they can decay. If we pick out a process of interest, for example in figure 1.5(a), squark decaying to chargino which then decays to LSP. This separate decay chain can be studied by

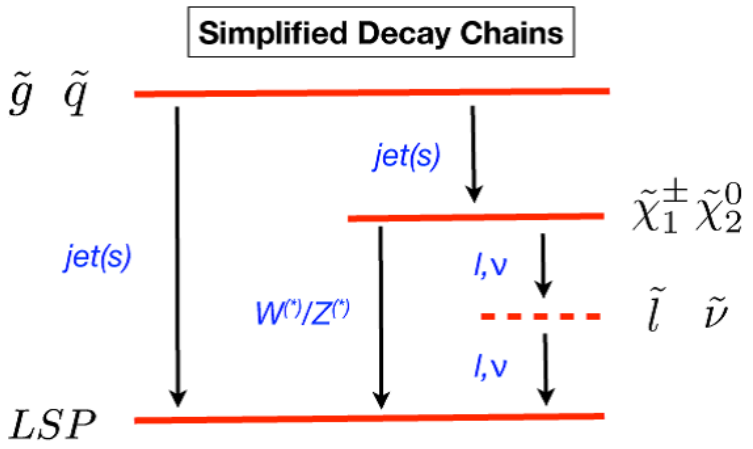

Figure 1.6: Simplified decay chain considered at ATLAS experiment [1]

itself, which suddenly simplified the view of SUSY scenario. Therefore, the simplified model can be described just by masses and cross section, which is a very simple and broad approach to design the SUSY searches.

Figure 1.6 shows the simplified decay chains considered in ATLAS experiment [1]. This approach allows to scan the whole sparticle mass plane without imposing a strict relation on the gaugino masses as are the cases in many of the high energy scale SUSY models such as mSUGRA. The results can be expressed in terms of limits on cross-section times branching ratios as a function of new particle masses, separately for each event topology.

CHAPTER 2

The Experiment

2.1 Introduction

This chapter gives a brief description of the experimental facilities used to derive precise information of the physics objects produced in pp collision. The particle accelerator and the main detector components are described.

2.2 Large Hadron Collider

The Large Hadron Collider (LHC) [41] is a synchrotron accelerator facility designed to deliver proton-proton collisions at $\sqrt{s} = 14$ TeV center-of-mass energy. The LHC is situated on the French-Siwss border, just outside Geneva and sits in an underground tunnel that is over 500 ft deep and 17 miles in circumference. It is located in the tunnel formerly used by the Large Electron-Positron Collider (LEP). The accelerator facility is hosted by the European Center for Nuclear Research (CERN). The proton beams are focused to collide in four places around the LHC ring, each housing a detector as shown in figure 2.1. The largest of the four, A Toroidal LHC ApparatuS (ATLAS) [3], and the Compact Muon Solenoid (CMS) [42], are multipurpose detectors addressing a wide range of physics topics. Another major experiment, A Large Hadron Collider beauty (LHCb) [43], is designed to mainly focus on the physics of b-quarks and the precision measurement of CP violation. The fourth experiment is A Large Ion Collider Experiment (ALICE) [44], dedicated to study the quark-gluon plasma in heavy ion collision.

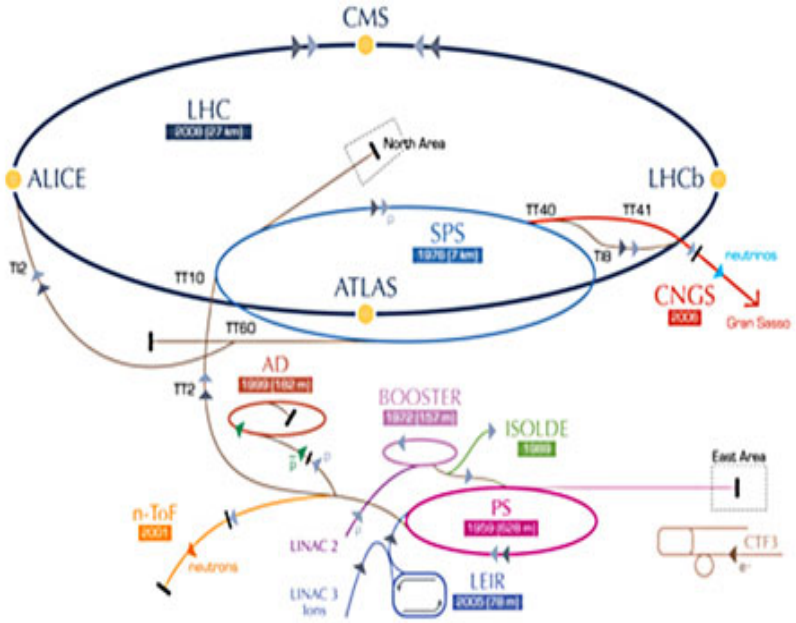

Figure 2.1: Schematic overview of the LHC accelerator complex at CERN, including a number of older accelerators used to ramp up the energy prior to injection. The yellow dots show the four collisions points, where the four large detector ATLAS, CMS, ALICE and LHCb are situated [2]

The LHC accelerator complex is shown in figure 2.1. Two high-energy particle beams travel at close to the speed of light before they are made to collide in opposite directions in separate beam pipes in LHC. The beams are guided around by a strong magnetic field maintained by superconducting electromagnets, which requires a temperature colder than outer space (-271.3^0C). The LHC is a series of several intermediate accelerators, that successively increase beam energy. The high energy protons are accelerated by a linear accelerator (LINAC) to 1.4 GeV before passing to the Proton Synchrotron (PS), which takes the energy up to 25 GeV and prepares the bunch structure with proper separation of 25 ns. Bunches then are injected into the Super Synchrotron (SPS), which further increases proton energy to 450 GeV. The beams are then injected into the LHC up to their maximal energy.

2.3 LHC Operation During 2012

An important consideration for any collider experiment is the number of events that will be produced for a given process, given by the process production cross section multiplied by the integrated luminosity, L,

$$N_i = \sigma_i \times L = \sigma_i \int L dt. \tag{2.1}$$

where N_i is the number of interactions which gives rise to a particular final state i depending on the cross-section σ_i. The instantaneous luminosity, L, of a pp collider is given by [45]:

$$L = \frac{\nu \gamma N_b N_p^2}{4\pi\epsilon\beta^*} F \tag{2.2}$$

where ν is the revolution frequency, γ is the relativistic gamma factor for the protons, N_b is the number of proton bunches in the beam, N_p is the number of protons per bunch, F is the geometric luminosity reduction factor due to the crossing angle at the interaction point, ϵ is the transverse beam emittance and β^* is the β function of the beam at the collision point. The product of ϵ and β^* essentially gives the area of the beam spot at the interaction point. In 2012, the peak instantaneous luminosity delivered to the ATLAS detector at the LHC reached $7.6 \times 10^{33} cm^{-2} s^{-1}$, 76% of its design luminosity of $10^{34} cm^{-2} s^{-1}$. In 2010 and 2011, the LHC operated at energy of 3.5TeV per beam and in 2012 this energy was raised to 4 TeV. During 2012, the integrated luminosity delivered by the LHC, recorded by ATLAS and certified as good quality, i.e. when all detector parts of ATLAS were running at nominal conditions, is shown in figure 2.2. Since March 2013 the LHC is in a Long Shutdown 1 (LS1) period for maintenance that will allow to operate the machine at 7 TeV per beam in 2015.

To maximize the number of events produced for a given process in a given time, it is important to have the largest possible instantaneous luminosity. At ATLAS the run duration is split into small sections of time over which an average luminosity can be recorded, called "lumi-block" (LBs). These are the units used to store luminosity and data quality information at ATLAS. During 2012 one LB corresponded to $\sim 60s$, and so run conditions such as stable beams and being ready for physics can be assigned on a LB by LB basis. This allows the beam conditions and detector state to be assessed with ease as a function of time.

The LHC proton beams are not continuous, but arranged in short bunches, which in turn are grouped, called bunch trains. Each beam can contain up to 2808 bunches, which intersect at the various interaction points. The nominal bunch spacing is 25 ns, however for most 2012 data taking the bunch spacing was 50 ns. In general, in each bunch crossing there is only one hard-scatter process that usually triggers the event, while the remaining inelastic interactions contribute to soft additional deposition of energy in the detector that blur the resolution of the hard process of interest. This phenomenon is called pile-up. The average number of pp collisions per bunch crossing was 20.7, and peaked at more than 40 simultaneous crossing. Figure 2.3 shows the distribution of the mean number of intersections per bunch crossing, which corresponds to the mean of the Poisson distribution of the number of intersections per crossing for each bunch.

A brief description of the ATLAS detector which was used to record events resulting from proton collision is described in the next section.

2.4 The ATLAS Detector

ATLAS [3], an acronym for "Toroidal LHC ApparatuS", is a general purpose detector to measure known processes (Standard Model) with more precision, and to

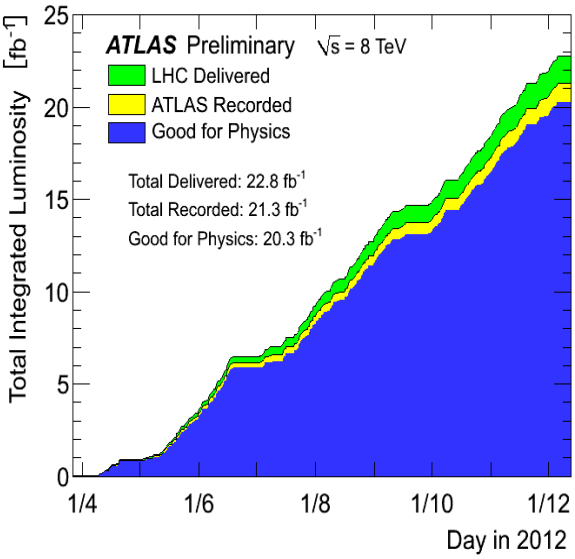

Figure 2.2: Integrated Luminosity and Data Quality in 2012. Cumulative luminosity versus time delivered to (green), recorded by ATLAS (yellow), and certified to be good quality data (blue) during stable beams and for pp collisions at 8 TeV center-of-mass energy in 2012.

search for new phenomena that are typically called Physics Beyond Standard Model. Discovery of the Higgs boson [11] is a great success of the ATLAS experiment, together with the CMS experiment. The ATLAS detector is located 92.5 m underground at intersection point 1 of the LHC tunnel and spans over 44 m length, 25 m height and weights about 7000 tons. The overall layout of the detector is shown in figure 2.4. It is comprised of three primary detection systems and built symmetrically in the backward and forward direction with respect to intersection point. The innermost layer hosts the tracking detector embedded in a 2T solenoidal magnetic field for the measurement of position and momentum of charged particles. Beyond are situated the calorimeter systems for energy measurement of both neutral and electrically charged particles. Finally, a muon spectrometer located within a large toroidal magnetic field to measure the position and momentum of muons, which can later be

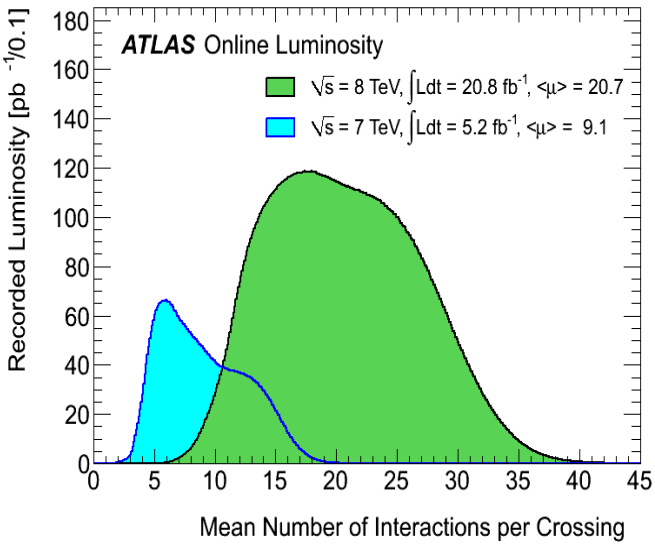

Figure 2.3: Luminosity-weighted distribution of the mean number of interactions per crossing for the 2011 (blue) and 2012 (green) data.

complemented with the information from the inner detector. The following sections provide a detailed description of each of the detector sub-systems.

2.4.1 Magnet System

Precise measurement of charged particle momenta requires a strong magnetic field. ATLAS houses two magnet systems, a hybrid system of a central superconducting solenoid and outer superconducting toroids (Figure 2.5). The central solenoid lies outside the inner detector and is extremely thin, whereas the toroid system consists of three toroids, each with eight coils, radially assembled around the beam axis. The magnetic field is responsible for bending the trajectory of charged particles. Their configuration is such that their field is mostly azimuthal and orthogonal to the muon trajectories, providing maximal bending power.

The central solenoid has an inner radius of 1.23 m, a total length of 5.8 m and sits just outside the inner detector. This solenoid immerses the inner detector in an

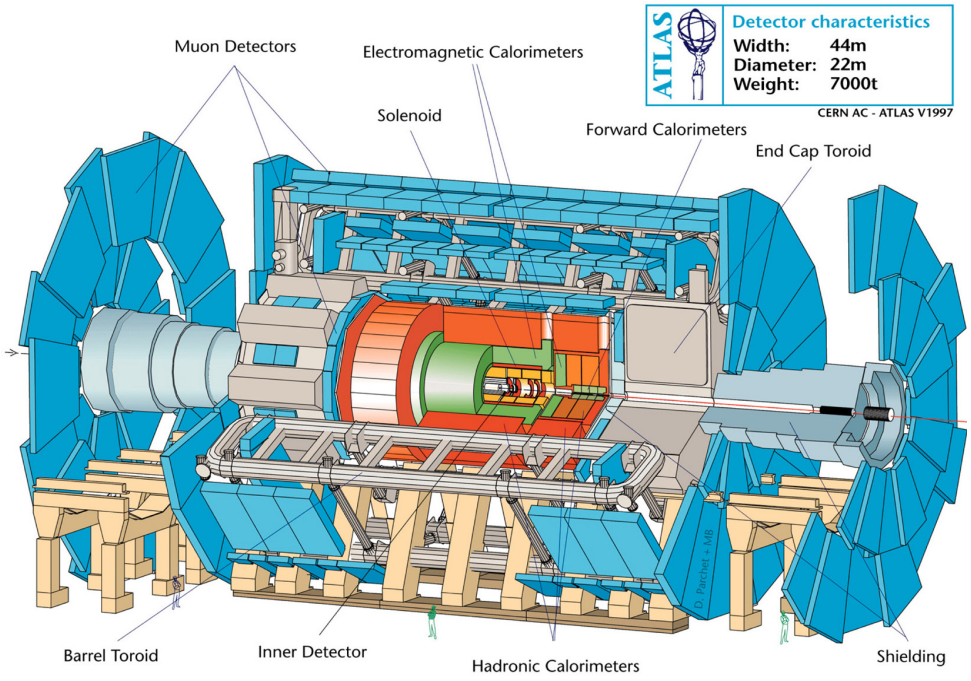

Figure 2.4: Schematic view of the ATLAS Detector and its subsystems [3]

axial 2T magnetic field, and with a thickness of only 45 mm, in order not to obstruct the calorimeters. The thickness is optimized so as to minimize the amount of material a particle must penetrate between the inner detector and the calorimeters.

The toroid system is divided into three regions, the barrel and two endcaps, arranged with an eightfold azimuthal symmetry around the calorimeters. The barrel part of the toroid is 25 m long and 5 m wide, whilst the endcap components are around 5 m long. All of the ATLAS toroids contain eight individual coils arranged at a constant radius with respect to the beam pipe at evenly spaced intervals. The barrel region produces a toroidal magnetic field of approximately 0.5 T for the central muon detectors and the endcap toroids produce a magnetic field of approximately 1T in the end-cap regions.

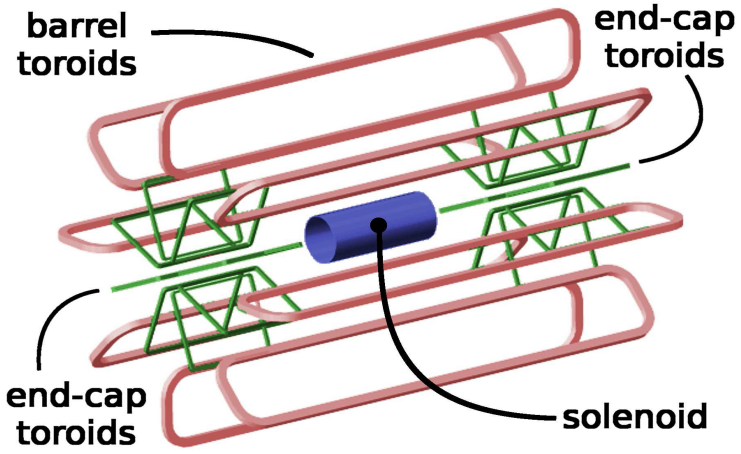

Figure 2.5: Schematic diagram of the ATLAS magnet system [4]

2.4.2 Inner Detector (ID)

The Inner detector is a composite tracking system, designed to identify and reconstruct the trajectory of the particles. The inner detector has a length of 6.2 m and a diameter of 2.1 m. Figure 2.6 shows a schematic view of the inner detector. The ID is immersed in a solenoidal magnetic field of 2T and reconstructed within the pseudo-rapidity range $|\eta| < 2.5$. Since it uses a solenoid magnet, in which charged particles are mostly deflected in the XY -plane, the ID is designed to have the highest precision in the transverse plane. It consists of the pixel detector, the semiconductor tracker and the radiation tracker which provide the first measurement of the collision decay products as shown in figure 2.7. The tube at the bottom is the beampipe. R is the distance from the center of the beampipe, the designated interaction axis.

The pixel detector is the closest to the interaction point and provide the best possible primary vertex (PV) and secondary vertex resolution. The ability to find short-lived particles, like b-hadrons, is mostly determined by the ability to separate the vertices. The pixel detector consists of three barrel layers and three endcap disks on each side of the barrel. The distances of the three barrel layers to the beam-line are

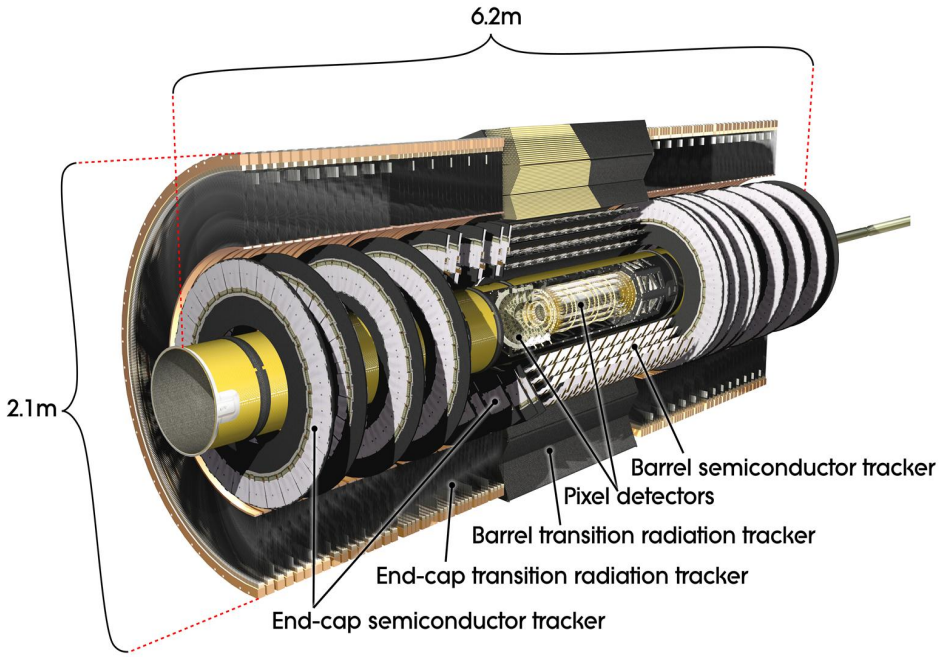

Figure 2.6: Schematic of the ATLAS Inner Detector [3]

5.05, 8.85 and 12.25 cm respectively. The endcap sit at 49.5 cm, 58 cm and 68 cm away from the interaction point. The Pixel suffers from intense radiation since it is very close to the collision point and operates at $\sim$ 150 V. The layers and disks are equipped with pixels, silicon sensors that are segmented into small rectangles. Pixels are 50 μm in size each, and are organized in modules which result in a total of 80 million silicon pixel. The pixel detector has 90% of the total number of ATLAS readout channels. The pixel size allows charged particles position resolution of approximately 115 μm along the beamline and 10 μm in the transverse direction. Since each pixel has a separate circuit and electronics, the pixel signal is known and provides a precise position measurement of the original particle.

The Semiconductor tracker (SCT) is situated around the pixel detector, where the particle density is low enough to use long narrow silicon strips, instead of pixels. The silicon strips making the coverage of a larger area more economical by reducing

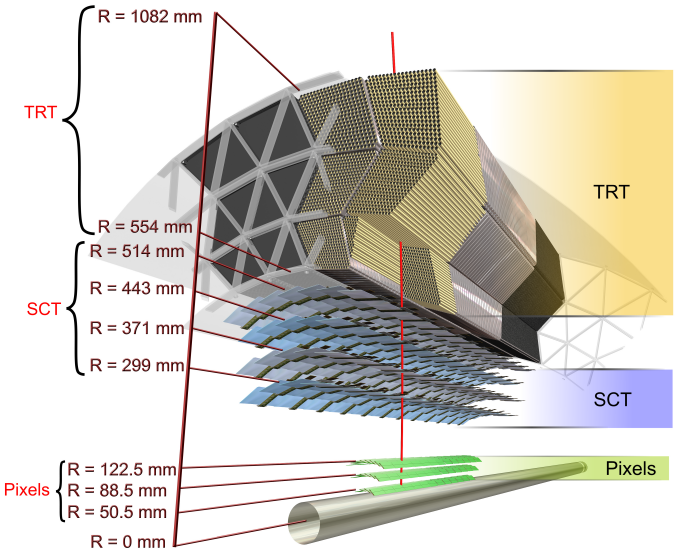

Figure 2.7: Schematic view of the different layers of the inner detector. Pixels are part of the pixel detector, SCT stands for semiconductor tracker and TRT for transition radiation tracker [3].

the number of readout-channels and covers the radii up to 52 cm. The SCT mostly contributes to momentum measurements, impact parameters and vertex positions. The silicon strips with a size of 80 μm by 12.6 cm are placed parallel to the beam line in the barrel and radially in the end-cap, which provides a precision measurement in $r-\phi$. The SCT consists of one central barrel and two end caps and the barrel is made up of 2112 modules distributed on four concentric cylinders. The SCT detector modules are equipped with two silicon strip layers with a strip pitch of 80 μm. The position measurement along the strip length is obtained by a small stereo angle between the strips in different layers. The readout of the SCT modules is binary, i.e. it registers only if a strip was hit or not, which limits the single strip resolution of the SCT to about 23 μm. The SCT, together with the pixel detector ensure accurate particle momentum measurement.

The Transition Radiation Tracker (TRT) surrounds the silicon detectors providing measurements of charged particles up to $|\eta| < 2.0$. It also allows to distinguish electrons from pions based on their transition radiation. The TRT is composed of 4 mm in diameter proportional drift gaseous tubes (straws) that have a wire in the center and are filled with a gas mixture containing Xenon. The tubes are placed parallel to the beam in the barrel region and radially in wheels in the end-cap region, providing a measurement in $r - \phi$ plane. The xenon gas mixture is ionized by the charged particles and free electrons drift to the anode, where the signal is amplified and finally readout. The signal is further enhanced due to transition radiation resulting from the passage of the particles through polymer fibers sitting between the tubes. For a given energy, electrons have a much higher Lorentz gamma factor than pions hence emit more transition radiation. By putting a threshold on the signal, the ratio of the high threshold hits to the total number of hits is a powerful variable for discriminating electrons from pions.

2.4.3 Calorimeter System

The ATLAS calorimeter system measures the energies of charged and neutral particles. A basic overview of the calorimeter system is given in figure 2.8. It is non-compensating sampling calorimeter; layers of absorber are alternated with layers of active media. The readout signal is proportional to the energy deposited in each layer of the active media. The calorimeter system is completely symmetric in ϕ and coverage extends up to $|\eta| < 4.9$. Broad η coverage is mandatory for event reconstruction, especially for accurate determination of the missing energy where weakly interacting particles are expected. The Calorimeter system is divided into two detectors: The EM Calorimeter and the Hadronic Calorimeter. The absorbed particles deposit their energy in the calorimeter cells by multiple interactions with the calorimeter materials

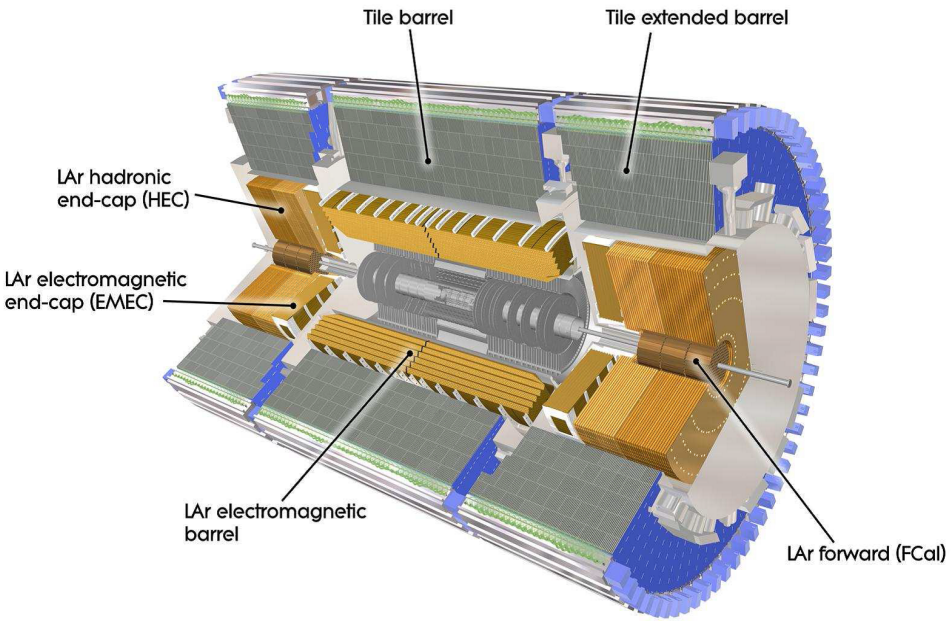

Figure 2.8: Overview of the Calorimeter System [3]

and the energy of the particles is measured in this process. Highly energetic electrons and photons are absorbed in the EM calorimeter and the hadronic calorimeter absorbs energy from particles that pass through the EM calorimeter, which are primarily hadrons.

2.4.3.1 Electromagnetic Calorimeter

The EM Calorimeter is a sampling calorimeter alternating lead absorber with liquid argon (LAr). The EM calorimeter have a fine granularity ideal for precise measurement of electrons and photons. It is divided into a barrel part defined by $|\eta| < 1.475$ and two end-caps within $1.375 < |\eta| < 3.2$. The barrel consists of two parts bound together by a small gap and each end-cap is also divided into two wheels covering different η region. In order to ensure the maximum azimuthal coverage and allow for fast read-out, the EM Calorimeter is designed with an accordion geometry

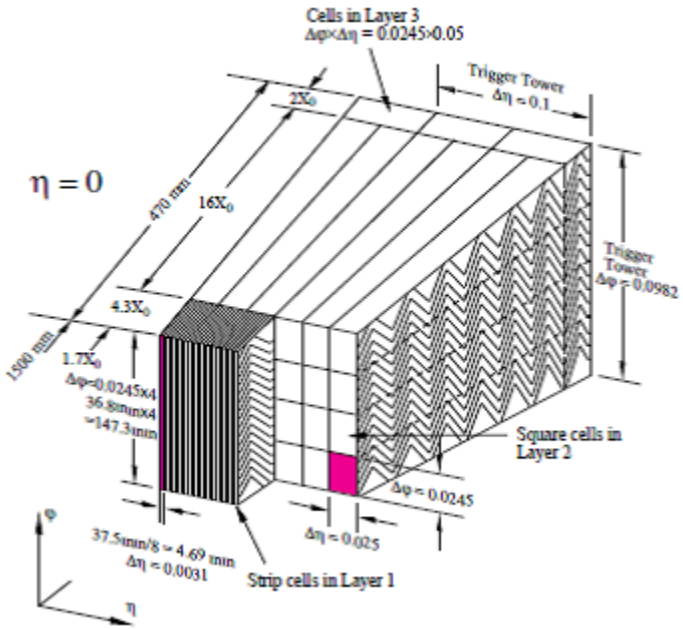

Figure 2.9: Sketch of an electromagnetic calorimeter barrel module [3]. The granularity in η and ϕ of the cells in each of the three layers is indicated.

that allows a gapless measurement in the ϕ direction as shown in figure 2.9. It's accordion shape structure consists of many layers of lead and steel that serve as absorber materials. Liquid argon is used as an active material because of its intrinsic linear behavior and stable response over time.

When an electron passing through the EM calorimeter meets the lead layer, photons are emitted due to bremsstrahlung mechanism and propagate in matter having a good chance of converting to e^+e^- pairs. A cascading avalanche of particles is produced, called an EM shower. Eventually, the particles are soft enough to lose their remaining energy by ionization and excitation. The depth of EM calorimeter is defined in terms of radiation lengths (X_0), which correspond to the mean path length required to reduce the energy of relativistic charged particles by the factor 1/e. The total thickness of the EM calorimeter is greater than 22(X_0) in the barrel and 24(X_0)

in the end cap to ensure that the complete energy of these particles is deposited in the calorimeters.

2.4.3.2 Hadronic Calorimeter

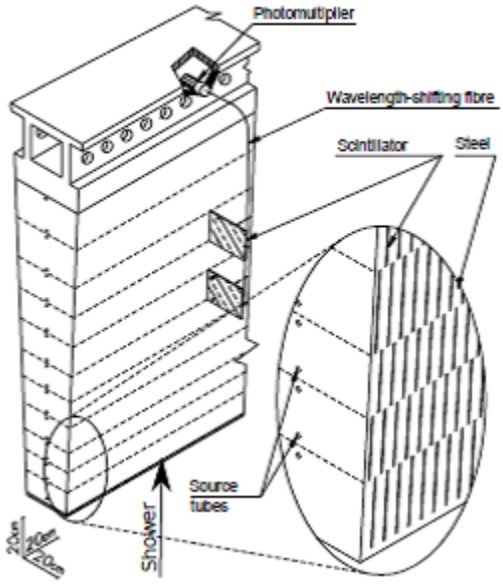

Figure 2.10: Schematic of the mechanical assembly of a single module of the Tile calorimeter showing the tile scintillators, the wavelength-shifting fibers and the photomultipliers for optical readout.

The hadronic calorimeter (HCal) is a sampling calorimeter employing steel as absorber and scintillating tiles as the active material. It is placed outside the EM calorimeter with coarser granularity sufficient for jet reconstruction and missing transverse energy measurements. The HCal consists of three different systems: the End-Cap Calorimeter (HEC), the Forward Calorimeter (FCal) and the Tile Calorimeter (TileCal). The hadronic end-caps (HEC) cover the region $1.5 < |\eta| < 3.2$ and reside in the end-cap cryostats along with the EM end-caps and forward calorimeters (FCAL). This means that the HEC has a slight overlap with the forward calorimeter

and the EM end-caps in η, minimizing the dead material in the transition region between calorimeter partitions. The HEC shares a cryostat with the end-cap EM calorimeter and also uses liquid argon as the active material. The FCal is integrated into the end-cap cryostats and consists of three modules in each end-cap.

The bulk of the hadronic calorimeter consists of a scintillator tile calorimeter (TileCal) which is divided into barrel ($|\eta| < 1$) and extended barrel ($0.8 < |\eta| < 1.7$) components. The TileCal is divided into 64 modules, each spanning $\Delta\phi \approx 0.1$ for full azimuthal coverage. The thickness of the calorimeter is chosen such that the calorimeter provides good containment of hadronic showers. At $\eta = 0$, the thickness is 11 λ, where λ is the interaction length defined as the average distance a hadronic particle travels before any inelastic interaction. The granularity is chosen to be mostly cells of dimension $\eta \times \phi = 0.1 \times 0.1$. There is a vertical gap between these two regions that provides some space for cables and is covered by the Intermediate Tile Calorimeter (ITC). The detailed description of ITC and it's calibration system is described in chapter 3. Ionizing particles produce ultraviolet scintillation light in the active material which is readout by wavelength shifting fibers, coupled to photomultipliers tube (PMT's) as shown in figure 2.10. The fibers coupled to each edge of the scintillating tiles are read out by two different PMTs to provide redundancy and sufficient information to partially equalize signals produced by particles entering the scintillating tiles at different impact positions. The thickness of the hadronic calorimeter provides good resolution for high energy jets and to limit the energy leakage into the muon spectrometer.

With increasing pseudo-rapidity, the radiation environment becomes harsher. Therefore the hadronic end-cap calorimeters and the forward calorimeters are based on the intrinsically radiation-hard LAr technology. The hadronic end-cap calorimeters at $1.5 < |\eta| < 3.2$ are copper/LAr detectors with parallel plate geometry, and each

consists of two independent wheels. The copper plates are 25 mm and 50 mm thick in the two wheels, with a LAr filled gap of 8.5 mm between plates. The HEC has a slight overlap with the forward calorimeter and the EM end-caps in η, minimizing the dead material in the transition region between calorimeter partitions.

The forward calorimeters (FCal) are located at each end-cap cryostat covering the high pseudorapidity region between $3.1 < |\eta| < 4.9$. The forward calorimeter is placed in the extreme forward region where particle flux is the highest. The design of the FCal is thus suited to deal with high radiation densities. FCal splits into three segments; an inner EM module where copper is used as the absorbing material and two outer hadronic modules where tungsten is the absorbing material. Cooper plates facilitate heat interchange, while the tungsten absorbers minimize the lateral spread of hadronic showers. The overall depth of this detector is approximately 10 nuclear interaction lengths.

2.4.4 Muon Spectrometer

The muon spectrometer is the outermost component of ATLAS detector, designed to measure muon momentum with a high precision independent of the inner detector. It is comprised of the magnetic field necessary for the momentum measurement provided by toroid magnets, one set of coils in the barrel region and two more sets of coils for the end-caps. A barrel toroid produces a magnetic field of approximately 0.5T and and two end-cap toroids produce 1T in the central and end-cap region, respectively. The muon system consists of four primary subsystems, shown in figure 2.12. There are two precision muon trackers: the monitored drift tubes (MDT) and cathode strip chambers (CSC), and two triggering subsystems: resistive plate chambers (RPC) and thin gap chambers (TGC).

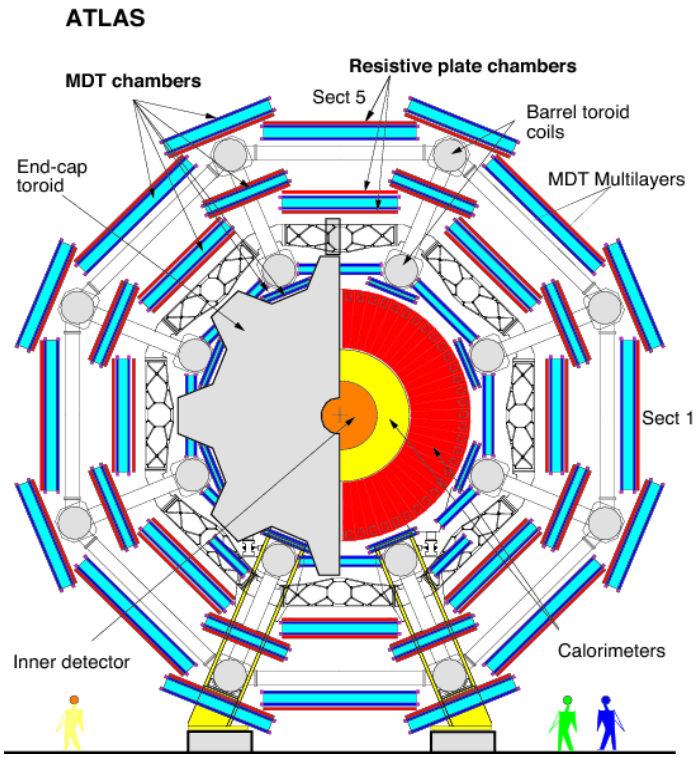

Figure 2.11: Transverse view of the muon spectrometer

Precise position measurements in the principal bending direction (η) is obtained using MDTs, which contain tubes filled with gas that is ionized when traversed by the charged muon. The MDT chambers are used in the central region $|\eta| < 2.7$, except in the innermost end-cap layer where their coverage is limited to $|\eta| < 2.0$. A typical MDT chamber consists of two multi-layers of drift tubes, which are separated by spacer bars made of aluminum. Each of these multi-layers contain four layers of tubes in the inner or three in the outer regions of the muon system. The MDT chambers use a mixture of $Ar - CO_2$ (93%-7%), kept at 3 bar absolute pressure. The gas mixture was selected for its aging properties and small likelihood of forming deposits within the tube. The direction of the tubes in the barrel and end-caps is along ϕ. Signal transmission to the electronics and connection to the HV supply system are at opposite ends.

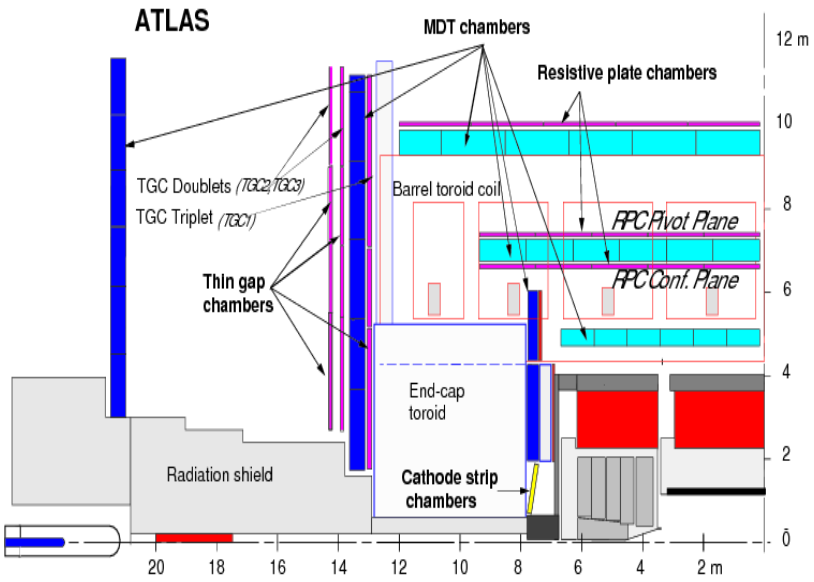

Figure 2.12: Schematic view of the muon spectrometer in the z-y (bottom) projections. Inner, Middle and Outer chamber stations are denoted BI, BM, BO in the barrel and EI, EM, EO in the end-cap.

The maximum safe counting rate per unit area for the MDTs is exceeded in the region $|\eta| > 2$. In this η region of the first layer, the MDTs are replaced by the CSCs, with a quicker response time and double resolution. They are multiwire proportional chambers with the wires oriented in the radial direction. The CSCs are better equipped to deal with the increased occupancy and radiation. The CSC system itself is segmented in ϕ, resulting in eight chambers in each of the two disks. With four CSC layers in each chamber, the average number of measurements per track is considerably less than in the MDTs.

An essential design criterion of the muon system was the capability to trigger on muon tracks. Therefore, the precision-tracking chambers have been complemented by a system of fast trigger chambers capable of delivering track information. For this purpose, in the barrel region ($|\eta| < 1.05$), RPC technology was selected, while in the end-cap ($1.05 < |\eta| < 2.4$) TGC were chosen. Both the TGCs and RPCs are designed

to deliver signals over a time spread of less than 25 ns. This way the bunch crossing responsible for the muon triggering the chamber can be identified with an efficiency of 99%.

2.5 Trigger System

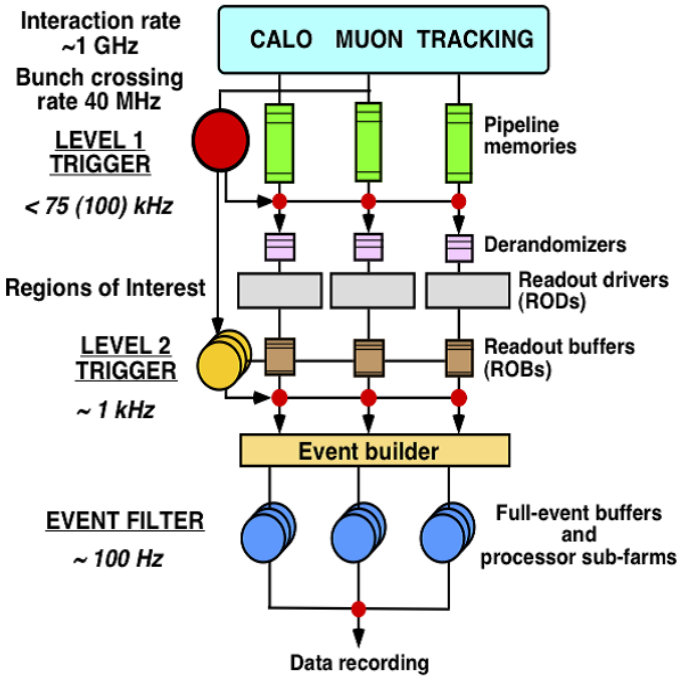

Figure 2.13: Schematic diagram of the ATLAS Trigger system [5].

ATLAS is generating more information than can be recorded to disk with full granularity, with a nominal 1 GHz LHC bunch crossing rate and $\sim$ 1 MB event size. Therefore, it is essential to have an efficient trigger system to select interesting events whilst rejecting those that are more abundant yet less physically significant. To decide if an event shall be stored, a three-level trigger system is implemented to search for interesting objects in an event for the ATLAS detector. A schematic of the system is shown in figure 2.13. Each trigger level refines the decisions made at the

previous level. These sequence of trigger levels will reduce the collision rate of almost 40 MHz to a more manageable $\mathcal{O}(100)$ Hz. As less events need to be considered at each successive stage, the allowed time to process an event increases with trigger level.

The first level, L1, is a hardware based trigger built with fast custom electronics, utilizing coarse calorimeter and muon information for the trigger decision. At this level the event accept rate is reduced to a maximum of 75 kHz. It is capable of making a decision in under 2.5 μs. In the case where the trigger is passed, the raw event data is sent to the readout stream via the RODs for the next trigger level. It also identifies possible Regions of Interest (ROI) in the detector for the second level, L2, to look at in more detail. RoI data includes also information on the type of feature identified and the criterion why the event passed that trigger stage.

The Level 2 (L2) trigger is software based which uses the fully reconstructed objects. At this level full granularity and precision is used for the trigger decision but only within particular RoIs as identified by the Level 1 trigger, thereby reducing the required data volume to take a decision to 2-6% of the total. Approximately 2 % of the total event data is available to the L2 trigger. The processing time is about 40 ms and the output rate is around 2 kHz. The rate is reduced by applying pre-scales to the data, which means that only a certain percentage of events passing the given trigger selection will actually be accepted. At L2 level, the p_T thresholds on objects are generally tighter, and the full granularity of the calorimeters are now available to use.

The final stage of the three level trigger system is the Event Filter (EF), the even rate is reduced to roughly 200 Hz. At this level, the final selection is made before physics events are written to disk, where they await further scrutiny in offline data quality. The average processing time of an event is of the order of four seconds. The level 2 and EF are collectively known as the High-Level Trigger (HLT).

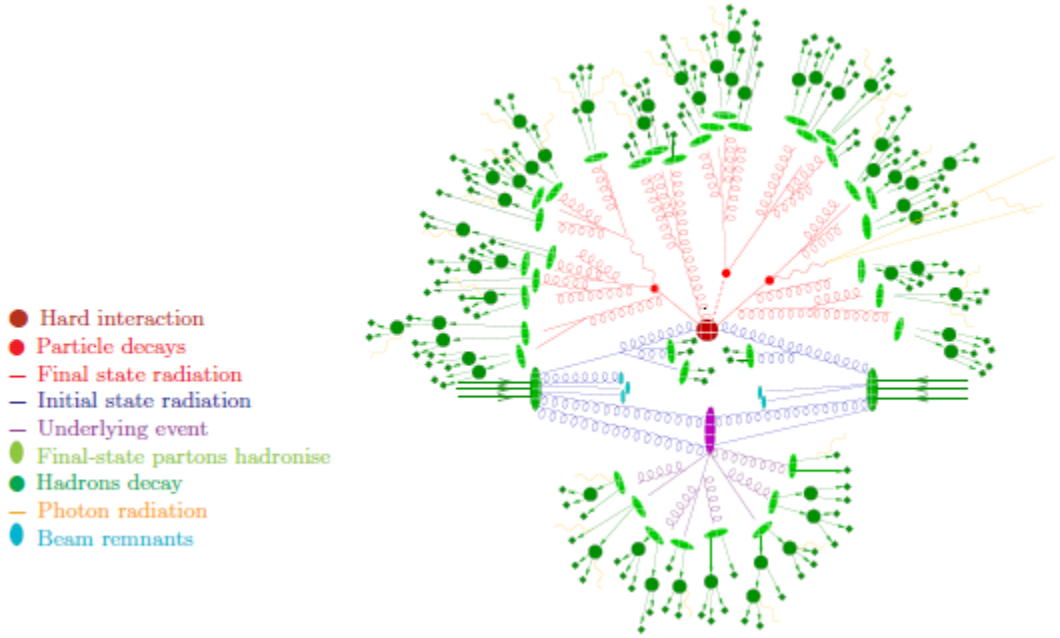

Figure 2.14: Representation of an event as produced by an event generator [6].

Proton-proton collisions require the interactions of colliding constituent quarks and gluons to be understood, with there additionally being more than one pair of interacting partons within a single proton-proton collision. In high-energy physics events are simulated using Monte Carlo (MC) event generators with computational algorithms, which uses random numbers to determine the probabilistic result of a particle interaction. The task of event generators is to simulate, as accurately as possible, the experimental characteristics of physics processes of interest. The generator level particle information is referred to as truth information.

There are several components that encompass the complete generation of an event in MC simulation. The colour coding shown in figure 2.14 corresponds to the steps into which most event generators divide the process. Only a tiny fraction

of events contain a high momentum-transfer process of interest called hard process (hard scatter). To predict the incoming partons contributing to the hard process MC generators use the parton model of the proton, with the momentum shared between constituent partons following a parton distribution function (PDF). The matrix-element computations are used to calculate the hard-process in exact perturbative QCD, where the cross-section for a specific process is calculated directly by summing the probabilities of all possible interactions.

A next stage of event generation comes from both the input and output partons from the hard-scattering process, subject to further parton emission. This phenomena is modelled in MC by the parton shower phase of event generators. Since quarks and gluons have colour charge these scattered partons in turn radiate gluons, which can then go on to emit radiation themselves. The process results in an extended showering of partons described using perturbative QCD. The parton shower evolution starts from the hard process and works downwards to lower and lower momentum scales to a point where perturbation theory breaks down. In most cases, a parton shower is also used to model initial state (ISR) and final state (FSR) radiation, where one of the incoming or outgoing partons emits radiation.

As the emitted radiation becomes increasingly soft, the coloured partons form hadrons, which take account of the confinement of a system of partons. At this stage, the MC generators are modelled as the hadronisation process. The implementation of this can be different depending on the specific generator [46] [47]. There is a very high probability that there will be other interactions, which overlap with the interaction of interest (hard interaction). This gives rise to the underlying event(UE), which is made up of secondary interactions between proton remnants. It produces soft hadrons everywhere in the event, which overlie and contaminate.

There are a variety of MC generators used for ATLAS analysis based on its suitability for the process considered. All of the MC generated samples used for this analysis have been centrally produced by the ATLAS Collaboration.

PYTHIA [48] [49] is a widely used MC generator that is capable of simulating both hard and soft interactions. It includes parton showering, hadronisation, particle decays and underlying events, as well as the evaluation of matrix elements, making it able to provide a full event view. MADGRAPH [50] is one of the example of a generator used in conjunction with PYTHIA. This leading-order (LO) matrix-element generator provides all Feynman diagrams for a specified process. POWHEG [51] [52] is a generator that calculates hard-interactions at next-to-leading order accuracy. HERWIG [53] is an event generator that is able to simulate the hard-scatter processes, which is interfaced with JIMMY [54] to provide the parton shower component. ALPGEN [55], a matrix element leading order generators, compute the exact process with additional hard radiation to a fixed order. They can accurately model events with large jet multiplicities but need to be interfaced with a parton shower algorithm to correctly handle the jet structure and soft radiation. Next Leading Order generators, like MC@NLO [56] (MC at Next to leading Order), generate events with correct NLO normalization and describe the hardest emission well. SHERPA [57] (Simulation of High-Energy Reactions of Particles) is a standalone event generator that is able to generate matrix elements, parton showers, ISR/FSR, hadronisation and the underlying event without interfacing with external packages.

These events generated at particle level need to be interpreted from an experimental standpoint, must be passed through a detector simulation. It includes a complete treatment of all the interactions with the various detector components and magnetic fields. A GEANT4 [58] simulation calculates where each particle interacts with the detector and how much energy it deposits as it passes through, a toolkit for

simulating the passage of particles through matter. When passed through the detector simulation, events are subject to the dedicated reconstruction algorithms, used to build the physics objects and calculate event level variables. Finally the events are used the collision data in physics analysis.

CHAPTER 3

Cesium Calibration of the Intermediate Tile Calorimeter

3.1 Introduction

The Intermediate Tile Calorimeter (ITC) [59] is a structural extension of the Tile calorimeter in the 680 mm of gap region between the barrel and the extended barrel calorimeter [60]. The ITC increases the volume of active material in the gap region, while still leaving room for the services and cables. The scintillators in the region $1.0 < |\eta| < 1.2$ are called gap scintillators, and the scintillators between $1.2 < |\eta| < 1.6$ are called crack scintillators as described in table 3.1.

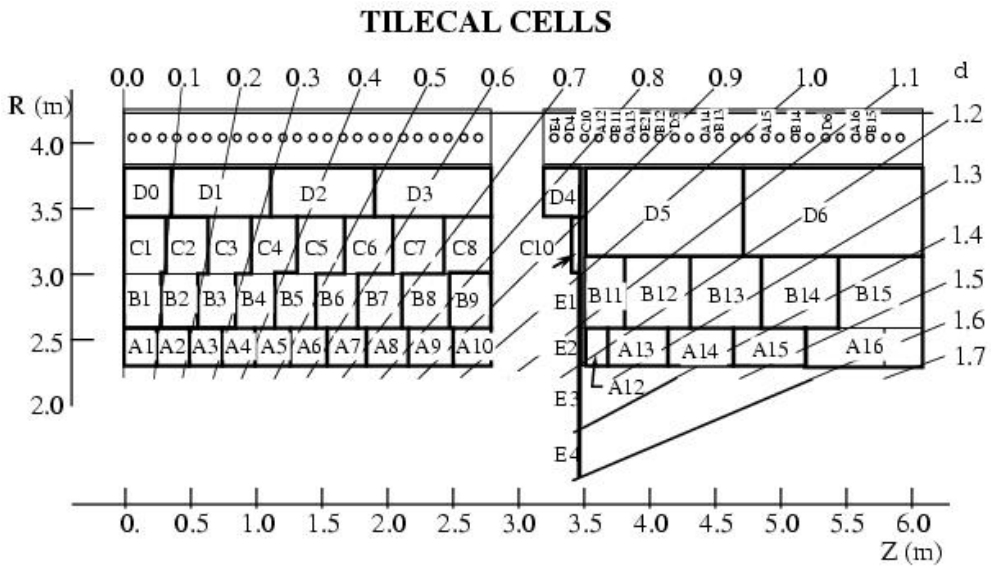

Figure 3.1: A sketch of the Tile Calorimeter cells in the barrel (left) and extended barrel (right) modules.

Table 3.1: Description of ITC cells type and parameters.

cell Type	eta position	material	Thickness	Nick-Name
D4	0.78 - 0.90	iron + scintillator	311 mm	Plug
C10	0.88 - 1.00	iron + scintillator	96 mm	Plug
E1,E2	1.0 - 1.2	scintillator	12.7 mm	Gap
E3,E4	1.2 - 1.6	scintillator	$<$ 10 mm	Crack

The ITC plug modules contain six different types of cells named D4, C10, E1, E2, E3 and E4 as shown in figure 3.1. In each extended barrel there are 64 of such modules. The Cells D4 and C10 are build with steel and scintillator tile while the E cells are made only of scintillator plates.

The standard calibration procedure is not suitable for the ITC cells due to the reduced size and the particular geometry of the cells. Therefore, we have developed a two step procedure and an optimized reconstruction method for the cesium data to be used in the cells of the ITC, where the standard cesium procedure is not optimal. There are two difficulties in applying the standard Cesium approach to the ITC cells. First, the differences in the mechanical structure result in cell response patterns that are not reconstructed efficiently by the standard method. Second and most importantly, a large fraction of the source radiation is not fully contained but leak outside the cells due to the reduced size and this fraction is not measurable due to the position of the cells at the boundary of the calorimeter.

To overcome these difficulties we use first an optimized algorithm to reconstruct the response to the Cesium source and use this response only to inter-calibrate cells of the same type. We assume that the amount of radiation leakage is similar in cells of the same type and size. Among the ITC cells there are four special D4 and eight special C10 cells as listed in table 3.2. D4 special cells are similar to normal D4 cells but of reduced size while the C10 special cells are made of single slabs of scintillator.

The response of special ITC cells is different than the normal because of less active material and treated separately in this inter-calibration procedure.

Table 3.2: Description of ITC special cells

cell type	module number	description
EBA D4	14,15,18,19	Reduced size
EBC D4	14,15,18,19	Reduced size
EBA C10	39-42 , 55-58	single piece of scintillator
EBC C10	39-42 , 55-58	single piece of scintillator

3.2 Cesium Calibration

The Cesium system is the primary tool to equalize and maintain the response of all calorimeters cells at the electromagnetic scale. It is designed to determine the quality of the optical response of each calorimeter cell, to adjust the PMTs high voltage in order to equalize the response from all cells and to monitor it with time. The objective is to keep the stability of the energy calibration at the 0.5% level. The Cesium calibration system uses a radioactive ^{137}Cs source movable by a hydraulic system. During the calibration runs the source crosses all TileCal cells, passing through holes in every scintillating tile. The ^{137}Cs source can travel through TileCal in two directions, clockwise and anti-clockwise. The channel by channel response to the energy deposited is used to equalize the response of all the cells and maintain global response of the calorimeter. The Cesium calibration tests the optical chain including aging effects in the scintillators. Cesium scans are performed every one or two months. The precision of the determinations is 0.3%.

3.2.1 ITC Cell Response

The ^{137}Cs source travels through each scintillating tile in the cell. The PMT current rises as the source approaches the tile and falls as the source exits and moves farther from the tiles. Assuming a constant source speed, the resulting shape as a function of time of PMT response to the total light collected from one scintillating tile is characterized by the sum of a gaussian function. As the source travels through many layers of scintillating tile, the overall PMT response is the sum of many such functions each one corresponding to the source traveling through each scintillating tile within the cell.

Figure 3.2 shows the PMT response as a function of time for some normal and special ITC cells. Mounted in particular positions affected by services or support structure these cells have even reduced size. All the other ITC cells have a standard size and number of scintillating tile/steel slabs and are readout by two PMT's.

In the proposed Cesium calibration methods cells of the same type and size are inter-calibrated with each others: normal D4, C10, E1 and E2 cell type are considered respect to the other cells of the same type and similarly the special cells are considered along with the other special cells of the same type.

3.3 The "UTA Integral" Method

Two different methods were developed to reconstruct the PMT response to the Cesium radioactive source. These were called: the "amplitude" and the "integral" methods. Due to the peculiar geometry of the ITC cells and their size, the standard methods above are not usable and not optimal. For this reason, we have developed more advanced approach for these cells and some dedicated algorithms. As we anticipated, one difficulty in the calibration of the ITC cells using the default integral

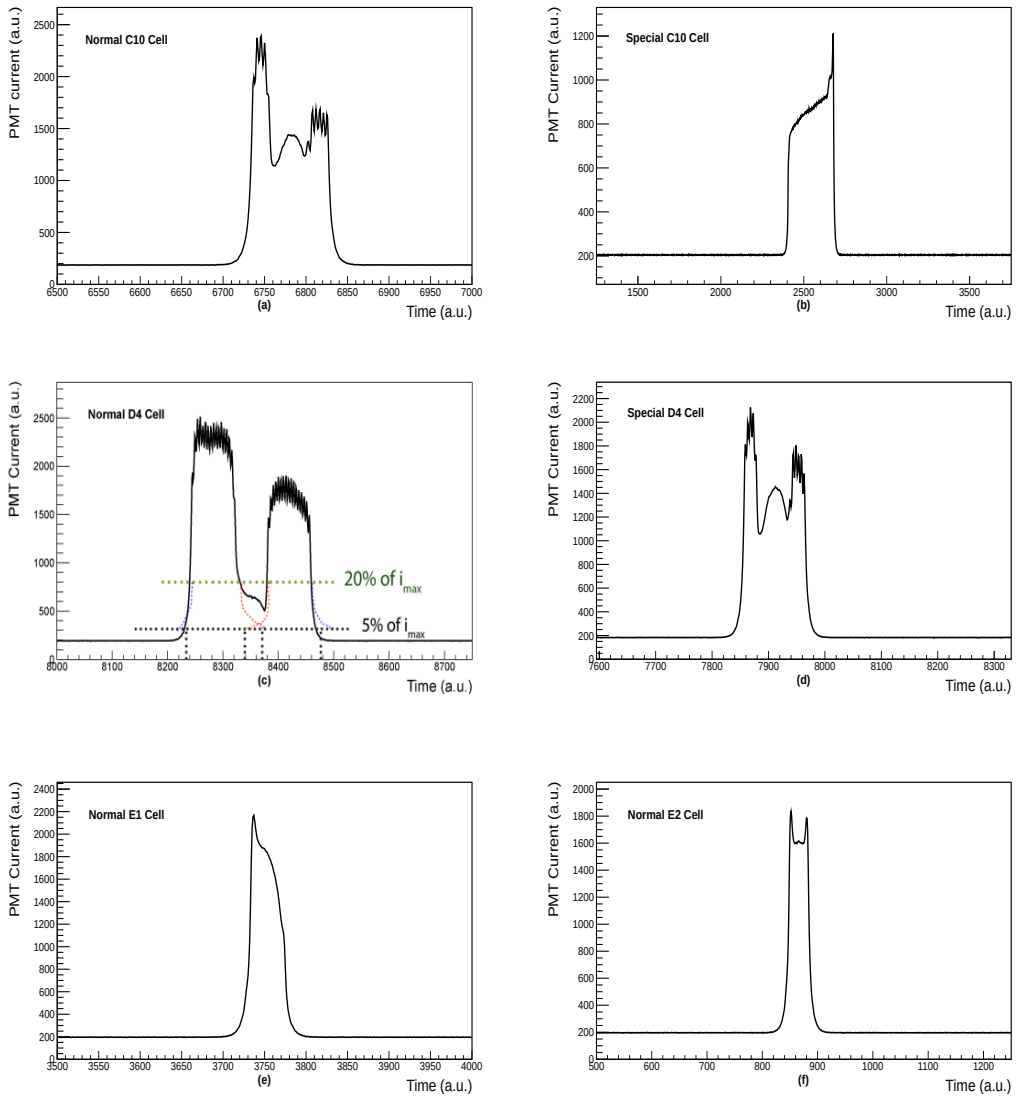

Figure 3.2: The PMT response to Cs source as a function of time for different type of ITC cells considered: (a) normal C10 cell; (b) special C10 cell of reduced size; (c) normal D4 cell; (d) special D4 cell of reduced size; (e) normal E1 cell; (f) normal E2 cell.

method is the instability in the extraction of the PMT response and the second is the lack of an adequate model of the Cs response in these cells.

We decided to factorize these uncertainties and use the Cs only to inter-calibrate cells of the same type. We consider the integral of the PMT current over the baseline

as an effective measurement of the light yield of the cell, including the contribution measured when the source is outside the cells. This integral of the PMT current pattern can be defined in an easy and stable way and used only to compare cells among themselves. In this way we are neglecting small differences in the structure of the cell as well as assuming that the energy leakage is, on average, similar for same cells type, which are reasonable and minimal assumptions.

First the baseline current (pedestal value) is measured and subtracted, then the numerical integration of the PMT current is computed using the Simpson formula, while extending the integration between two limits that are defined when the measurements cross a defined threshold shown in the figure 3.2 (c). The pedestal is defined as the average PMT current when the source is far from the cell.

The PMT current patterns are very similar in the different modules (depending on the local movement direction of the source) and some simple logic with a large threshold is applied to the PMT response over the entire run time to determine the range of interest, where the "interesting" peaks lie. A sufficiently large threshold is needed to rule out the possibility of a leakage signal when the source is in an adjacent layer. While these leakage currents are small compared to the true response of the source, they are large compared to normal noise fluctuation. Therefore, to determine the threshold value, the entire range is scanned to find the maximum value of the signal. Half of the signal maximum is considered as the threshold to determine the interesting region in the data. Then windows of different sizes are defined for the different cell types using the knowledge of the signal extension.

Then finally the smaller threshold is applied to define the limits for the numerical integration. The systematic effect due to the threshold values that define the integration limit was studied. Various thresholds between 5 and 100 ADC counts above the pedestal were used to determine the responses of all ITC cells. There is no

large dependence in the inter-calibration precision. The threshold was finally fixed at 50 ADC counts above the pedestal for all ITC cells. This correspond to about ten sigma in terms of the RMS of noise fluctuations and about 2 % of the maximum current for most of the cells.

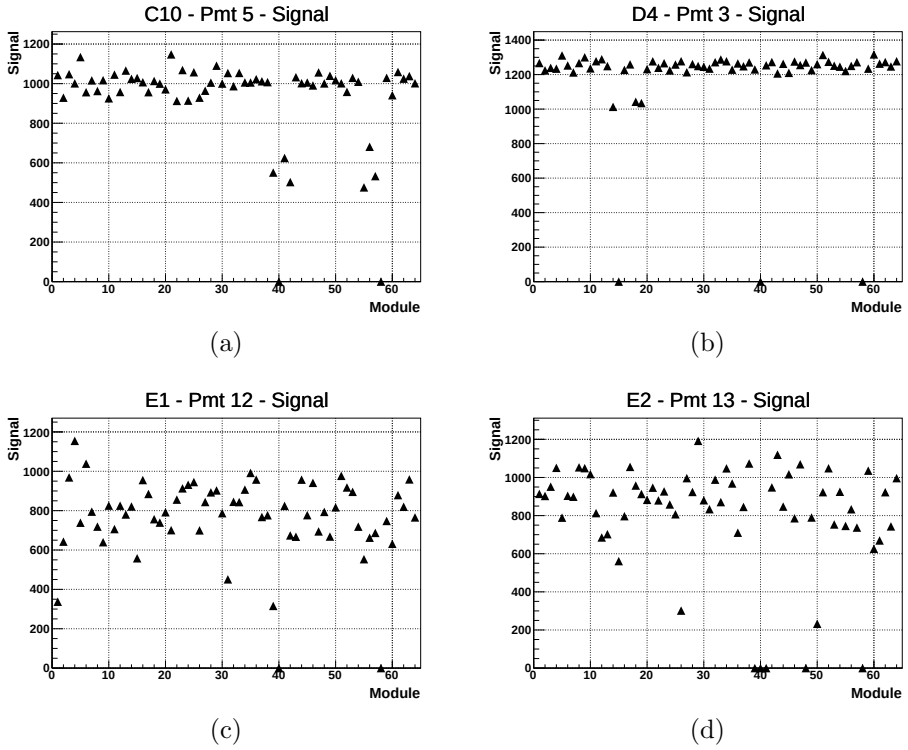

Figure 3.3: Examples of the response parameters extracted in the ITC cells C10 (a), D4(b), E1(c) and E2(d) in the EBA modules. The response is defined as the ratio of the integral value and the width. The lower response of the special C10 and D4 cells is clearly identifiable.

The cell response (signal) is defined for each cell as can be seen in figure 3.3. The signal width is the distance between the integration limits, defined as the number of time measurements with the PMT response above the threshold. The signal integral is the numerical integration of the currents within the two limits. The response is

defined as the ratio of the integral value and the width (equation 3.1). Special modules have in general lower responses.

$$Response_i = \frac{Integral_i}{Width_i} \tag{3.1}$$

The response of the different cells can be equalized by changing the High Voltage (HV) or applying an inter-calibration constant. The preferred method for these cells (that are not used in the analog LVL1 trigger) is to apply inter-calibration constants. The constants are defined for each read out channel by the ratio of the response defined above for each PMT and the average response of PMTs reading out that cell type (equation 3.2). The average response used is determined separately for normal and special cells.

$$k_i = \frac{response_i}{< response >} \tag{3.2}$$

We can think of this step as a ϕ inter-calibration; all the cells of the same type are inter-calibrated but the scale between different type of cells (D4 with respect to C10 or E1/E2 and also respect to all the normal cells) is not affected.

Overall the ITC cells energy scale is fixed using the relative cell response in cosmic rays as explained in the note [61]. In this way the unknown factors due to the Cs energy leakage in the different cells is factorized out. In the same note we perform a validation of the Cs reconstruction method described above, comparing the Cs response and the muon response as obtained in the same cells. A good correlation is observed indicating that the Cs method above is a robust estimation of the cells light yield.

3.4 Analysis Results

3.4.1 ^{137}Cs response of ITC cells

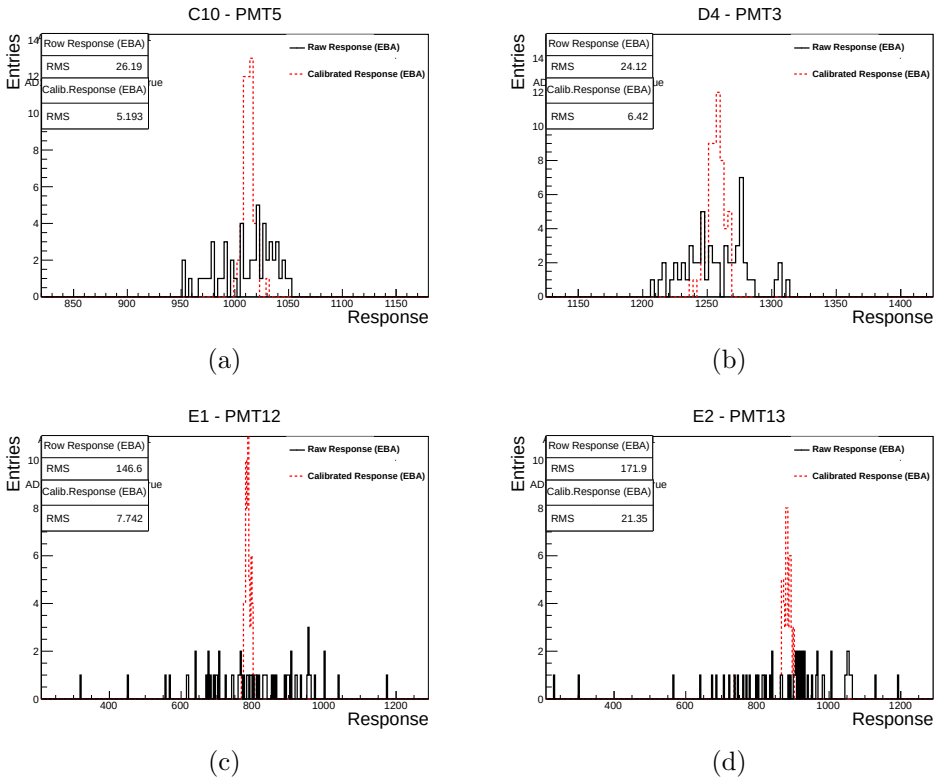

Figure 3.4: Comparison between the calibrated and the un-calibrated (raw) response for ITC cells in EBA.

To test the effectiveness of new algorithm, a set of calibration constants are obtained using several runs with magnetic field on, and applied to other runs. Figure 3.4 shows a comparison between the raw response and the calibrated response of the ITC. The comparison of the RMS before and after the calibration show a significant reduction in the dispersion of the cell response. The cells D4 and C10 have been already calibrated in the past using the standard method, which is reflected by the

dispersion of the raw response of the cells being smaller than the dispersion of the E1 and E2 that were never calibrated.

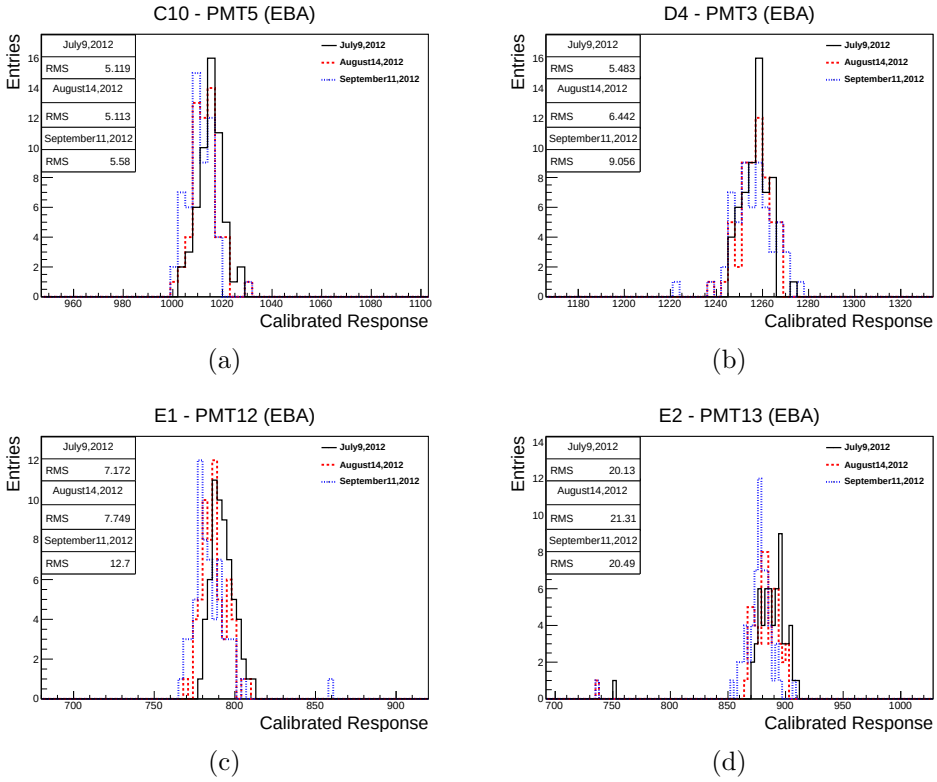

Figure 3.5: Evolution for three consecutive runs for the extended barrel side A. Same set of intercalibration values were applied to all the runs.

The resulting calibration constants were implemented in the database. Cesium response and constant have been calculated for many runs starting from June 2010 to February 2013 and we can study the evolution of the response. Figure 3.5 shows this evolution for three consecutive runs for the EBA, where the inter-calibration constants applied in all these runs are fixed. These plots shows that the RMS of the response increase as a function of time. Therefore, new constant values are needed to inter-calibrate the response periodically.

The relative difference between the runs is shown in figure 3.6 using one run and one set of calibration constant as reference so that the evolution of the cells inter-calibration can be seen. A maximum difference of 1% is observed for ITC cell C10 and D4, whereas, a maximum difference of 2% is observed for E1 and E2. Some special cases exist where the relative difference is larger in one of the run, this is possibly due to the bad data or acquisition errors in few channels.

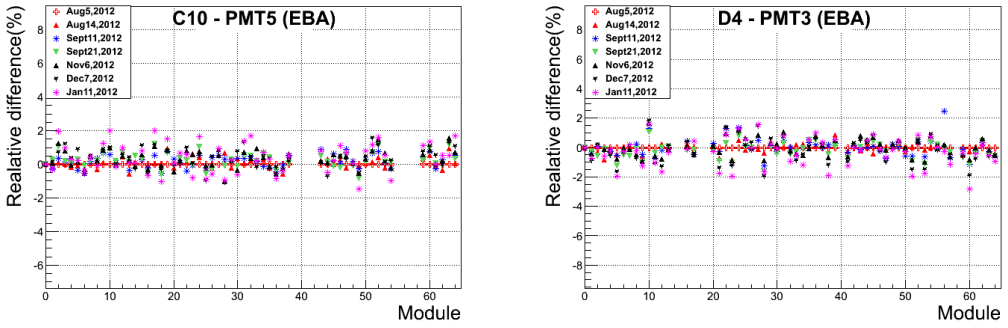

(a) (b)

(c) (d)

Figure 3.6: Percentage relative difference between all the 2012 inter-calibration constants and the January reference run for EBA ITC cells.

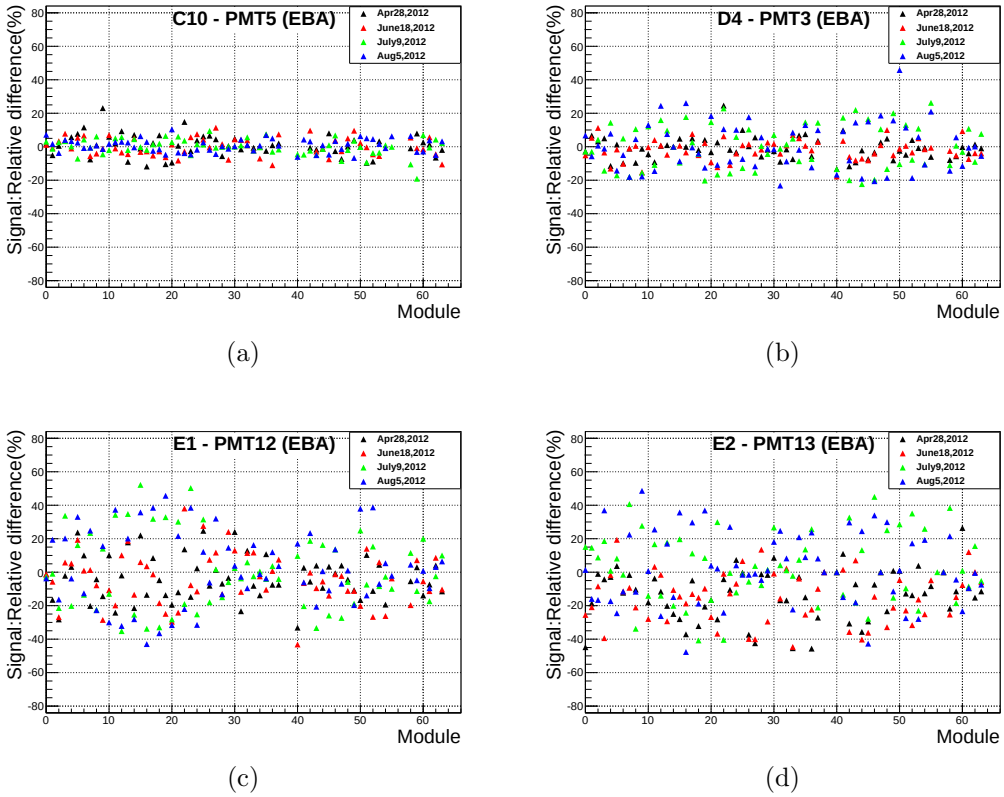

Figure 3.7: The relative difference between runs with source moving in opposite direction for the the cells C10(a), D4(b), E1(c) and E2(d) for EBA. Few independent runs are shown

3.4.2 Systematic Effects due to the Source Movement Direction

The ^{137}Cs source can travel through the calorimeter in two directions, clockwise or counterclockwise. Locally the source travels in opposite direction in even and odd modules, since for a given direction, the source entrance point in each modules alternates. In principle there should be no effect due to the source movement direction but some small systematic effects are possible due to the intrinsic speed of the current integrator circuitry in the 3in1 cards and local non-uniformities in the speed.

The effect of direction was studied comparing data runs acquired with source moving in both directions. To avoid the instability or decay effects, only runs taken

on the same day were taken into account. The response of the cells obtained with both directions is compared in figure 3.7 using several set of runs. There is clearly an appreciable effect that can be estimated of the order of 1-2% for the cell C10 and D4, and reach a maximum of 4% differences for the E1 and E2. The largest effect is noticeable for vertically oriented modules. In order to reduce these systematic effects, two cesium runs are needed with the source traveling in two directions and then the two corresponding constants are averaged in the analysis. This is always the case for the EB modules, two full runs with the capsule running both ways are always taken.

3.5 Time Evolution of the ITC Cell Response

The evolution of the ITC cell response as a function of time is presented in this section. The cell response is obtained using a set of Cs runs taken between June 2010 and February 2013, with magnetic field on. The average response of ITC cells as a function of time is shown in figure 3.8. The points are normalized to the activity of ^{137}Cs source in June 2010. The error bars represents the uncertainty on the average over all of the modules, and the line represents the ^{137}Cs decay curve (-2.3%/year). The RMS/mean of the cells distribution as a function of time is shown in figure 3.9. The dispersion of the cell response increases with the time as is observed in the rest of the calorimeter.

The inter-calibration procedures described above and the results shown in the previous sections aimed at a better uniformity of the detector response at a given time (when the Cs run is taken) and did not change the absolute PMT response to the ^{137}Cs decay between the different runs.

Now it is clear from the figure 3.8 that the average response of the cells change with time. The light yield of the scintillator degrade and the gain of PMTs change over time and also this can be monitored and corrected using the Cs. So to calibrate

the ITC together with the inter-calibration constant that didn't change the average detector response we provide a factor to take into account the global drift of the response between two runs.

The change observed in the PMT response between any two time period (t_1 and t_2), is described by the ratio of the two measurements in equation 3.3.

$$C(t_1, t_2) = \frac{< Measurement(t_2) >}{< Measurement(t_1) >}; for\ t_2 > t_1 \tag{3.3}$$

The correction factor to be applied is defined as in equation 3.4 where the response of each run is corrected to take into account the natural ^{137}Cs decay using the known decay rate of a ^{137}Cs source is 2.3% per year (half-life of 30.17 years).

$$T(t_1, t_2) = \frac{< \frac{CsResponse(t_2)}{2^{-\frac{t_2 - t_0}{\tau}}} >}{< \frac{CsResponse(t_1)}{2^{-\frac{t_1 - t_0}{\tau}}} >}; \tau = 10987\ days \tag{3.4}$$

The evolution of the ITC cell responses over few years, obtained using the runs described above, is shown in figure 3.10. The plots basically show the deviation of measured response from expected Cesium decay curve for the period June 2010 to February 2013. Only normal ITC cells are taken into the account in the average excluding this way few special ITC cells.

A moderate up-drift of order 0.5% is observed during 2010 for most of the ITC cells. After the 2010 technical stop we can say as a global tendency that some up-drift, around 1-2 % is still observed in C10 and D4 cells while some down-drift is seen in the cells E1 and E2 (maximum 4%). One other general tendency that we observe some oscillation with reduction of the response during data taking and recovering during shut down periods. Similar behavior is observed in the rest of the calorimeter.

3.6 Conclusion

We studied a new procedure and developed some simple and fast algorithm to improve the calibration of the ITC cells. The Cs reconstruction method used as default in the rest of the calorimeter (integral method) does not give reliable and robust estimations in these cells due to the many peculiarities described, while other more sophisticated approach (like the amplitude method) were never tried.

The procedure and algorithm described in this chapter uses the Cs data for the cell inter-calibration, while cosmic rays data were used for the initial setting of the scale between the different types of cells. This simple approach helps to calibrate these special cells and reduce the non uniformity to a figure of the order of one percent or smaller.

The time evolution of the ITC cells response extracted using this method shows a similar behavior to the rest of the calorimeter cells in term of down-drift and up-drift of the response during periods of data taking and shutdown as well as a monotonic increasing in the dispersion of the cells response as a function of the time.

The calibration constants for these cells have been provided with our stand-alone programs regularly along all of the LHC Run-1 and integrated into the database together with all of the other detector constants. For Run-2 this approach will be fully integrated in the standard Cs Calibration procedures with the implementation being currently finalized.

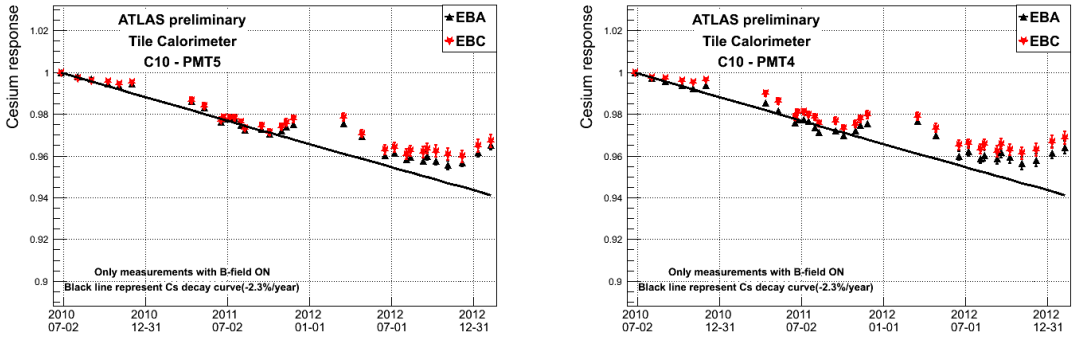

(a)

(b)

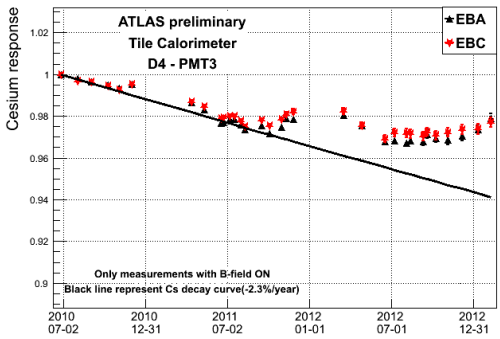

(c)

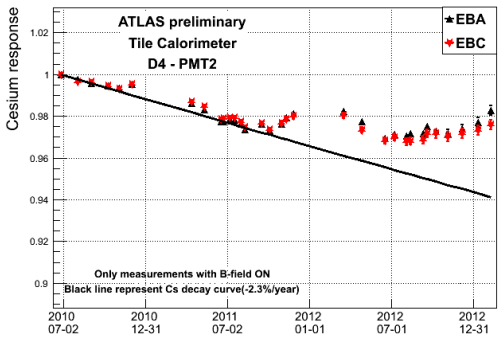

(d)

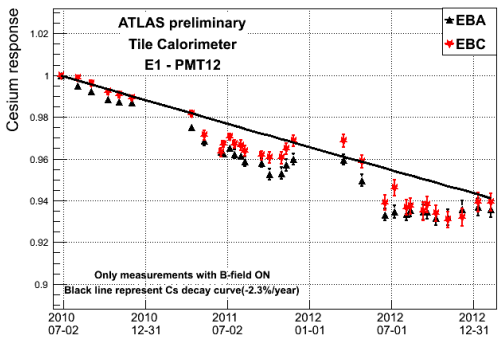

(e)

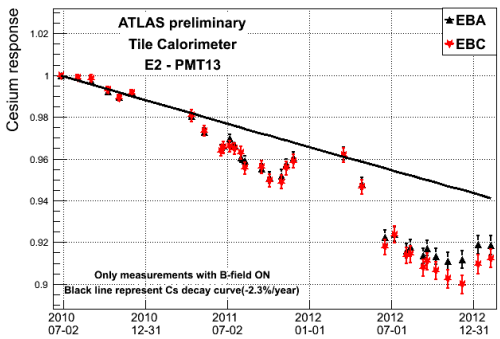

(f)

Figure 3.8: Evolution of the ITC cells average response as a function of time for C10(a,b), D4(c,d), E1 and E2(e,f). Cells in bad modules have been excluded in the average. The error bars represents the RMS of the distribution of the different cells. The black line represents the Cesium decay curve (-2.3%/year). Black and red points correspond respectively to EBA and EBC.

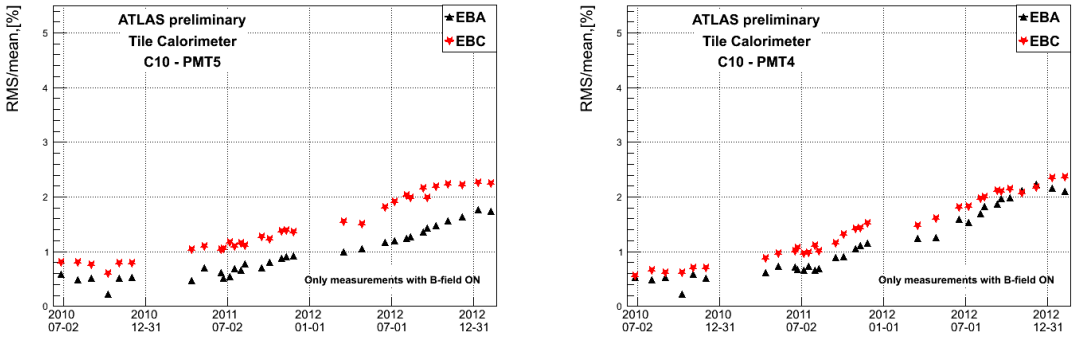

(a)

(b)

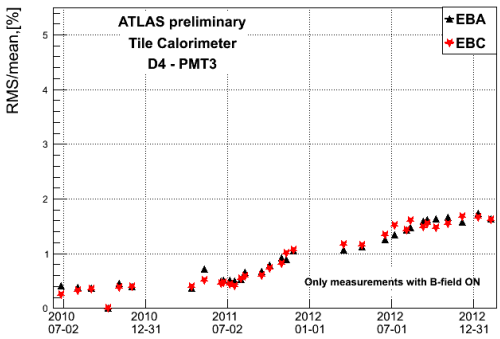

(c)

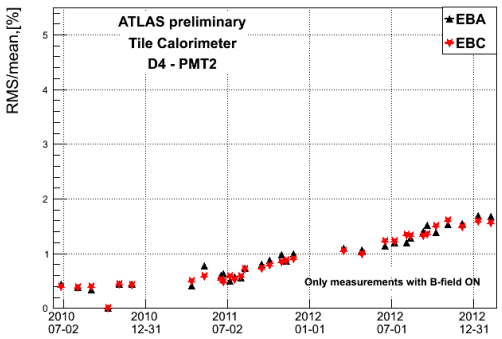

(d)

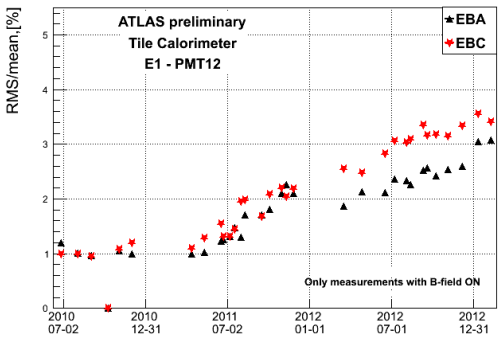

(e)

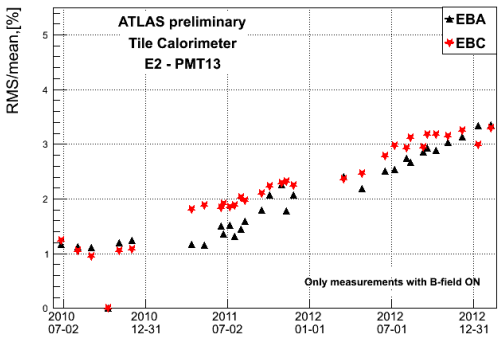

(f)

Figure 3.9: The relative dispersion of the distribution of the cell response (RMS/mean) as a function of time for C10(a,b), D4(c,d), E1 and E2(e,f). Black and red lines correspond respectively to EBA and EBC.

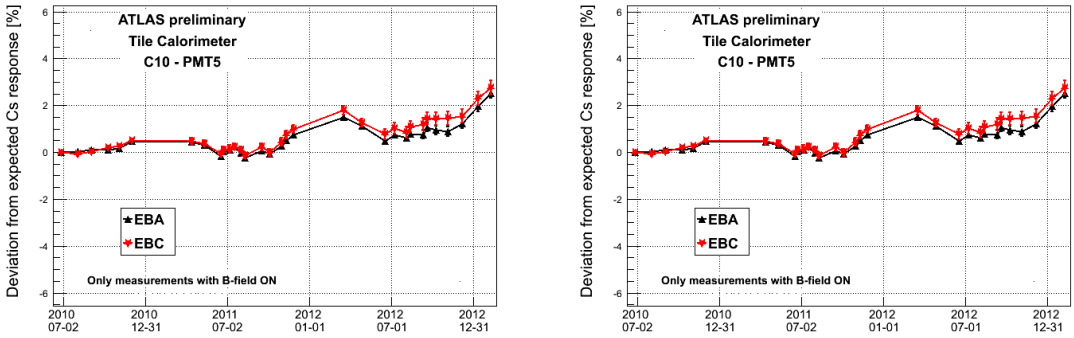

(a)

(b)

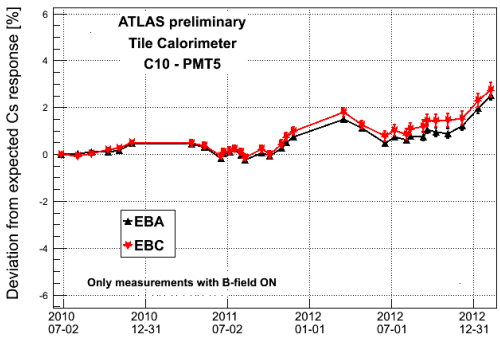

(c)

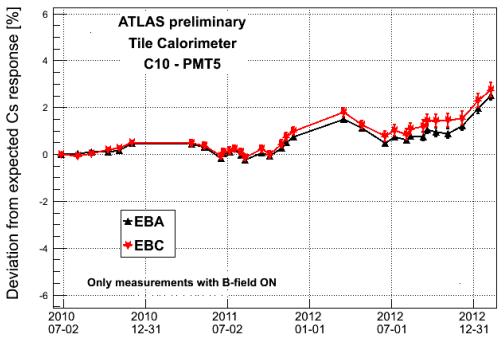

(d)

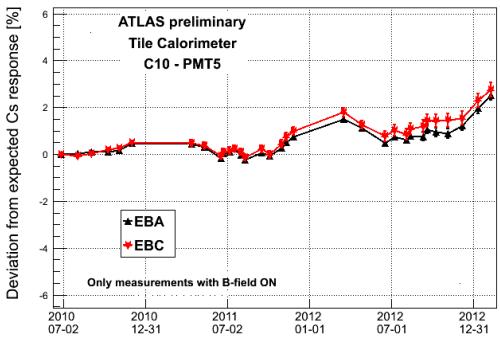

(e)

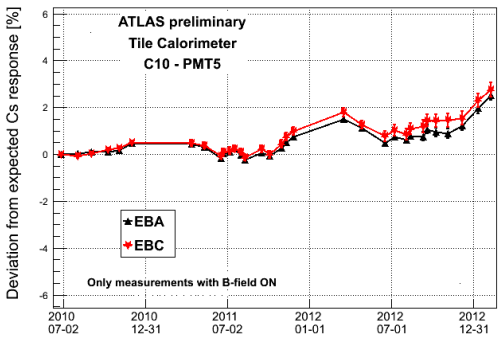

(f)

Figure 3.10: Deviation of measured Cesium response from the expected cesium decay for C10(a,b), D4(c,d), E1 and E2(e,f). Black and red lines correspond respectively to Side A and Side C.

CHAPTER 4

Third Generation SUSY Searches

4.1 Introduction

In SUSY, the left- and right-handed third generation squarks, $\tilde{q}_R$ and $\tilde{q}_L$, can mix to produce two mass eigenstates, $\tilde{q}_1$ and $\tilde{q}_2$. The lightest of which can, in the case of maximal mixing, be significantly lighter than the first and second generation quarks. Considerations of naturalness and its impact on the SUSY particle spectrum suggests that top squarks (also called stop) cannot be too heavy, to keep the Higgs boson mass close to the electroweak scale [62]. More specifically, naturalness considerations [63] [64] [65] [66] require that these squarks are lighter than approximately 500 GeV. Thus $\tilde{q}_1$ could be pair-produced with relatively large cross-section at the Large Hadron Collider. The previous Tevatron and LHC searches [67] [68] [69] [70] [71] [72] set limits for such particles between 100 GeV and $\sim$ 700 GeV depending on the SUSY scenario.

Figure 4.1 shows the production cross section for several SUSY processes at $\sqrt{s} = 8$ TeV. It is clear that for a given mass scale first and second generation squark and gluino pair production has a considerably larger cross section than stop pair production. However, if the stop is much lighter, for example $m_{(\tilde{t})} < \frac{1}{3} m_q/m_g$, they will have a higher cross section. Therefore, searches with stops become more important with increased luminosity.

The top squark can decay into a variety of final states depending, amongst other factors, on the hierarchy of the mass eigenstates (s)particles involved in the

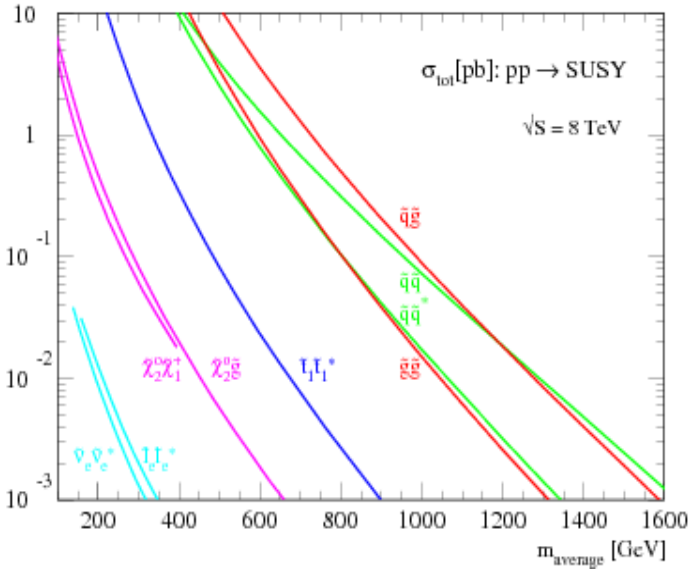

Figure 4.1: Sparticle production cross sections as a function of the sparticle mass (or average mass for e.g. multiple squarks), $m_{average}$ at $\sqrt{s} = 8\text{TeV}$

decay chain. In our study the relevant mass eigenstates are the lightest chargino $\tilde{\chi}_1^{\pm}$ and the $\tilde{\chi}_1^0$.

$$\tilde{t}\tilde{t} \rightarrow \tilde{\chi}_1^+ b \tilde{\chi}_1^- b \rightarrow W^{(*)+} \tilde{\chi}_1^0 b W^{(*)-} \tilde{\chi}_1^0 b \rightarrow l^+ \nu \tilde{\chi}_1^0 b l^- \nu \tilde{\chi}_1^0 b \tag{4.1}$$

where $\tilde{t}$ is the scalar top quark, $\tilde{\chi}_1^{\pm}$ and $\tilde{\chi}_1^0$ are, respectively, chargino and neutralino, and the second one is expected to be the lightest supersymmetric particle (LSP). The LSP is assumed to be stable for R-Parity conservation and is a candidate for dark matter. The decay mode in equation 4.1 corresponds to figure 4.3, and can happen only if $m(\tilde{t}) - m(b) \geq m(\tilde{\chi}_1^{\pm})$, i.e. it requires the chargino to be real. The final state under study contains two b-jets, two W bosons, real (a) or virtual (b), and two invisible particles, which is the same final state as for the production and decays of pairs of top quarks, which thus constitute an irreducible background. Since only the leptonic decay mode of the W(*) is considered, the events are characterized by the presence of two isolated leptons (electrons, muons) with opposite charge, and two b-

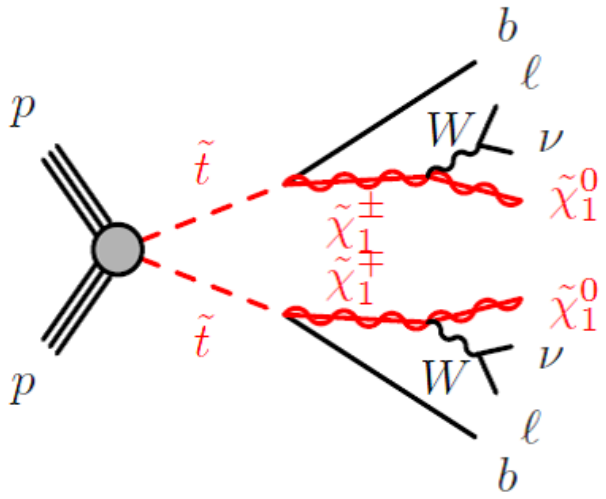

Figure 4.2: Feynman diagrams representing the processes considered in the analysis. The figure illustrates the 2-body decay of the stop to a bottom quark and a chargino ($\tilde{t} \to bW\tilde{\chi}_1^0$). The processes consider the signature with two leptons in the final state.

quarks. This signature occurs only in $\sim 4.6\%$ of the events, which is the probability that both top W(*) decay leptonically (Figure 4.2). Significant missing transverse momentum p_T^{miss}, whose magnitude is referred as E_T^{miss}, is also expected from the neutrinos and nueutralinos in the final state events.

4.2 Analysis Overview

In this analysis, a bino-like $\tilde{\chi}_1^0$ is assumed, and the lightest top squark is chosen to be the partner of the left-handed top quark ($\tilde{t_L}$ component), the only coloured particle contributing to the production processes. The kinematics of the $\tilde{t} \to b + \tilde{\chi}_1^{\pm}$ decay mode depend upon the mass hierarchy of the $\tilde{t}$, $\tilde{\chi}_1^{\pm}$ and $\tilde{\chi}_1^0$ particles (figure 4.3). In order to be sensitive to all the possible mass splitting, two different strategies are designed to search for $\tilde{t}$ pair production. One strategy is to target large mass splitting $\tilde{\chi}_1^{\pm} - \tilde{\chi}_1^0$, which is larger than W boson mass, and the other mass splitting $\tilde{\chi}_1^{\pm} - \tilde{\chi}_1^0$ is

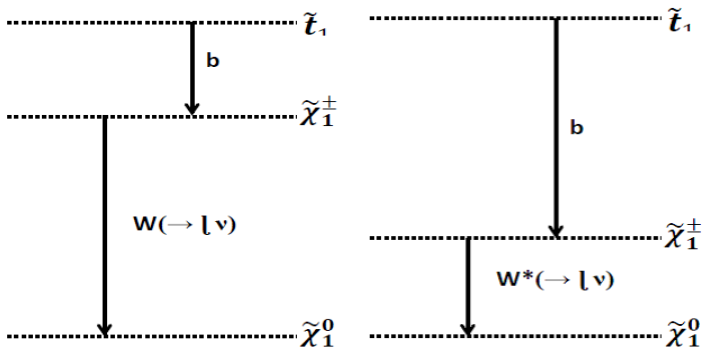

(a) (b)

Figure 4.3: Scalar top quark decay modes in [equation 4.1]: through real (a) or virtual (b) W boson production.

smaller than the W boson mass. Two different strategies target two different scenarios treated separately in the analysis. :

- mass spectrum with soft leptons (Figure 4.3a)
- mass spectrum with hard leptons (Figure 4.3b)

4.3 Data-set and Monte Carlo Samples

4.3.1 Monte Carlo Samples

MC simulations are used to assess the sensitivity to specific SUSY signal models, as part of the background determination for the search optimization process, and to set exclusion limits on particular signal models. All Monte Carlo datasets were produced by the Atlas simulation framework that models the interaction of the generated shower of particles with a simulation of the detector. GEANTt4 [58] or AtlFast-II [73] are used for detector simulation. MC datasets emulate different beam conditions and a realistic modeling of the pile-up conditions observed in the data. They were produced with a pp $\sqrt{s} = 8$ TeV, and a variable number of pp interactions

per bunch crossing. MC generators used to simulate each of the different background processes, including the used cross section calculated for $\sqrt{s} = 8$ TeV.

4.3.1.1 Signal Samples

Supersymmetric particle production processes are generated using MADGRAPH-5.1.4.8 [74] interfaced to PYTHIA-6.426 [75] with the PDF set CTEQ6L1 [76]. The grid of signal points for the decay shown in figure 4.1 is generated in the context of simplified models where the stops are produced in pairs, and assumed 100% Branching Ratio (BR) when they decay into $b - \chi_1^{\pm}$. The BR is the fraction of events for a chosen particle measured to decay in a certain way. Including the relevant mass hierarchy, the SLHA input files [77] are included for this purpose. In this framework the stop mass is fixed to 300 GeV and the two free parameters are the mass of the chargino and the mass of the lightest neutralino. In order to target scenario 1 with the soft leptons, we consider only the grid points shown in blue stars which are filtered with $E_T^{miss} > 60$ GeV in the region highlighted by the black dashed line. For the hard leptons, only the points with black diamonds, filtered with a request of at least 1 lepton with $p_T > 10$ ("Lepton filter") in the region highlighted by the blue dashed line are considered. The trigger strategies to select events in these two scenarios are chosen accordingly. The granularity of the considered grid is chosen to cover all the topologies of the channel of interest with a reasonable number of model points. Both $\chi_1^{\pm}$ and χ_1^0 masses are varied in steps of at-least 50GeV, while steps of 25 GeV or less are used in lower mass region.

4.3.1.2 Background samples

Monte Carlo simulated event samples are used to describe all the backgrounds which produce events with two prompt leptons. The SM background samples used in

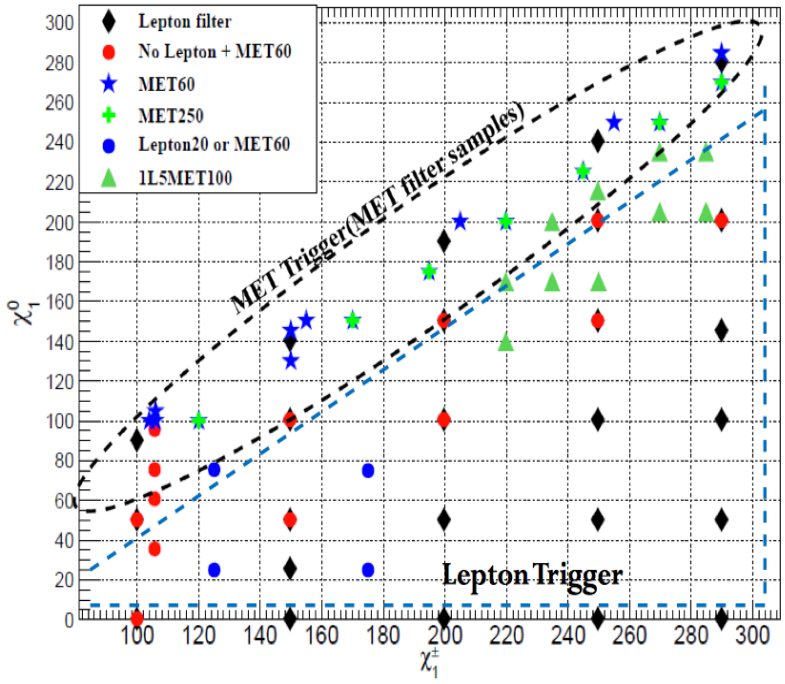

Figure 4.4: Grid of signal points in the $m(\chi_1^0) - m(\chi_1^\pm)$ plane, while $m_{\tilde{t}} = 300$ GeV. Only the points shown with blue stars in the region highlighted by the black dashed line and with black diamonds in the region highlighted by the blue dashed line are considered for the analysis. The trigger strategies to select events in these two scenarios are chosen accordingly:"MET trigger" and "Lepton Trigger" for scenario 1 and 2 respectively.

the analysis are listed in table 4.1. The role of each sample, i.e. whether it is used as baseline or only in the systematics evaluation, is also specified for each background process. The cross sections recommended by the SUSY working group (`SUSYTools version 00-03-20`) have been used for all samples. Different initial-state (ISR) and final-state radiation (FSR) are used to generate additional samples in order to evaluate the effect of their systematic uncertainties.

Top-quark pair and single top events were generated using MC@NLO-4.06 [78] [79], interfaced with HERWIG-6.520 [53] for the fragmentation and the hadronization process, and using JIMMY-4.31 [54] for the underlying event description. Diboson samples(WW, WZ and ZZ) are generated with POWHEG-1.0 [51] and interfaced to

PYTHIA-6.426. The samples generated with SHERPA-1.4.1 are used to estimate the systematic arising from the choice of event generator. Samples of Z produced with jets are generated with SHERPA-1.4.1 [6], while ALPGEN-2.14 [55] and JIMMY-4.31 are used for evaluation of systematic uncertanities. Samples of ttZ and ttW were generated using MADGRAPH-5.1.4.8 interfaced to PYTHIA-6.426. DrellYan samples are generated with SHERPA-1.4.1. Higgs boson production is simulated with PYTHIA-8.165, including all decay modes.

4.3.2 Recorded Data

The data sample used in this analysis was recorded by the ATLAS detector during the the year of 2012 with the LHC operating at a pp center-of-mass energy of $\sqrt{s} = 8$ TeV. Data were collected based on the decision of a three level trigger system. Application of data-quality requirements results in an integrated luminosity of $20.3fb^{-1}$ for the "MET trigger" selection and $20.1fb^{-1}$ for the "Lepton trigger" selection. Data stream and triggers for soft lepton and hard lepton channels are summarized in table 2.3.

Egamma and Muon data streams events are selected with both single and dilepton triggers, without any changes during the data taking periods. The single lepton triggers are the lowest un-prescaled triggers. The di-lepton triggers enlarge the overall acceptance with respect to only single lepton trigger with the lower threshold. Di-electron candidates are taken from the Egamma stream only and the di-muon candidates are taken from the Muon stream only. Di-lepton triggers requiring the simultaneous presence of an electron and muon are selected from both streams.

Table 4.1: List of Standard Model Monte Carlo samples used in the analysis.

Process	dataset ID	generator	Role
$t\tilde{t}$	110001	MC@NLO	baseline
Wt	108346	MC@NLO	baseline
Zt	179991-179992	MadGraph	baseline
WW	126928-126936	Powheg	baseline
$ZZ(\rightarrow 4l)$	126937-126942	Powheg	baseline
$ZZ(\rightarrow 2l2\nu)$	126949-126951	Powheg	baseline
WZ	129477-129494	Powheg	baseline
Z+jets ($m_{ll} > 40$ GeV)	167749-180551	Sherpa	baseline
Drell-Yan	173041-46	Sherpa	baseline
(8 GeV$< m_{ll} <$ 40 GeV)			
$t\tilde{t} + W$	119353-119354	MadGraph	baseline
$t\tilde{t} + Z$	119355-119356	MadGraph	baseline
$t\tilde{t} + WW$	119583	MadGraph	baseline
$ggH \rightarrow ZZll\nu\nu$	160655	Powheg	baseline
$ggH \rightarrow WW2l$	161005	Powheg	baseline
$WH \rightarrow WWl\nu$	161105	Powheg	baseline
$WH \rightarrow b\bar{b}l\nu$	161805,161816	Pythia	baseline
$ZH \rightarrow WW2l$	161155	Powheg	baseline
$ZH \rightarrow b\bar{b}2l$	161827,161838	Pythia	baseline
$t\tilde{t}$	117209-117210	AcerMC	systematics
$t\tilde{t}$	105860	Powheg+Jimmy	systematics
$t\tilde{t}$	117050	Powheg+Pythia	systematics
WW	126892	Sherpa	systematics
WZ, ZZ	126893-126895	Sherpa	systematics
Z+jets ($m_{ll} > 40$ GeV)	107650-107675	Alpgen	systematics
Z+heavy jets	109300-109313	Alpgen	systematics

Table 4.2: Data streams and triggers used in the analysis.

Channel	**Triggers**	**Data stream**
2 Soft Lepton	MET trigger	JetTauEtmiss
at least 1 Hard Lepton	di-lepton and single-lepton triggers	Egamma and Muons

4.4 Definition of Primary Objects

Particle candidates are used in the event selection and to define all the different analysis regions represented by objects reconstructed from calorimetric and tracking measurements. In the following section the definitions of physics objects relevant to the analysis are described. These definitions agree with `SUSYTools-00-03-20` package and with the prescriptions provided by the combined performance groups for the considered data periods.

4.4.1 Jets

Quarks and gluons are not directly observable due to the short range of the strong force and colour confinement. Energetic partons produced in collisions hadronise creating collimated bunches of hadrons known as jets that to some extent reflect the kinematics of the underlying partons. The initial energy of the high-energy quark is now shared among the hadrons in the jet. But for a quark with sufficiently high energy only a small amount of the quarks initial energy is used in forming the hadrons; most of it is carried in their kinetic energy. The total energy and direction of the resulting jet is quite similar to the initial energy and direction of the initial quark.

In ATLAS jets are reconstructed from energy deposits in the calorimeter cells that are fed to clustering algorithms. Jets are reconstructed using the anti-kt jet algorithm [80] with four-momentum recombination and radius parameter R = 0.4 in $\eta - \phi$. Jets are calibrated using local cluster weighting (LCW)+ jet energy scale (JES)

Table 4.3: Jet selection criteria.

Cut	Value/Description
Preselected Jets	
Algorithm	AntiKt4LCTopo
Acceptance	$p_{\mathrm{T}} > 20$ GeV, $\|\eta\| < 2.5$
Overlap	$\Delta R(j, e) > 0.2$
Signal Jets	
Acceptance	$p_{\mathrm{T}} > 20$ GeV, $\|\eta\| < 2.5$
Quality	JVF > 0.5 for jets with $p_{\mathrm{T}} < 50$ GeV and $\|\eta\| < 2.4$

scheme. Jets in this analysis are always contained within $|\eta| < 2.5$ and have a pT of at least $p_{\mathrm{T}} > 20$ GeV. To suppress pile-up jets, an additional cut on the Jet Vertex Fraction (JVF) is applied, asking for $JVF > 0.5$ for jets with $p_T < 50$ GeV and $|\eta| < 2.4$. The jet vertex fraction quantifies the fraction of the total jet momentum of the event that originates from the reconstructed primary vertex.

The identification of jets resulting from the fragmentation and hadronisation of b-quarks is performed through the use of b-tagging algorithms. To identify that the selected jet candidates contain a b-hadron decay (b-jets), we used a neural-network-based algorithm. These algorithms use tracking information to attempt to identify the secondary vertex due to the displacement between the primary interaction and the topology of b- and c-hadron decays inside a jet [81]. The efficiency for tagging b-jets in MC sample of $t\tilde{t}$ events using this algorithm is 70% with rejection factors of 137 and 5 against light quarks and c-quarks, respectively.

4.4.2 Electrons

Electron candidates are identified as clusters of energy deposits in the electromagnetic calorimeter that can be matched with a well-measured track. To meet the analysis needs, further selection criteria are defined considering different quality clas-

sifications of electron candidates. Electrons are selected using three main classes of quality cuts: loose, medium and tight, each with increasingly strict requirements and hence decreasing efficiency and fake rate [82]. A series of cleaning cuts are used to retain real electrons only.

Electrons are selected using the standard `egamma` algorithm. If the track contains at most three silicon hits, η is taken to be η^{clust}, otherwise η is taken to be η^{track}. The electron transverse energy E_{T} is computed as: $E^{\text{clust}}/\cosh(\eta)$. A smearing procedure is applied to the electron energy in MC, while a residual energy scale correction is applied to the electron energy in data.

Table 4.4: Baseline electron and muon selection criteria for MET trigger.

Electron Baseline	
Algorithm	AuthorElectron
Acceptance	$E^{\text{clust}}/\cosh(\eta) > 7$ GeV , $\|\eta\| < 2.47$ (if no. silicon hits > 4, $\eta = \eta^{\text{track}}$ else $\eta = \eta^{\text{clust}}$)
Quality	`mediumPP`
Overlap	$\Delta R(j, e) > 0.4$
Electron Signal	
Isolation	"mediumIso"
Muon Baseline	
Algorithm	STACO, combined or segment-tagged muon
Acceptance	$p_{\text{T}} > 6$ GeV, $\|\eta\| < 2.4$
Quality	`Loose`
Overlap	$\Delta R(j, \mu) > 0.4$
Muon Signal	
Isolation	"mediumIso"

For soft dilepton selection in MET trigger, electron candidates are required to have $p_{\text{T}} > 7$ GeV and $|\eta| < 2.47$ and must satisfy "medium++" requirements.

Table 4.5: Baseline electron and muon selection criteria for lepton trigger.

Electron Baseline	
Algorithm	AuthorElectron
Acceptance	$E^{\text{clust}}/\cosh(\eta) > 10$ GeV , $\lvert\eta\rvert < 2.47$ (if no. silicon hits > 4, $\eta = \eta^{\text{track}}$ else $\eta = \eta^{\text{clust}}$)
Quality	`mediumPP`
Overlap	$\Delta R(j, e) > 0.4$
Electron Signal	
Quality	`tightPP`
Isolation	"tightIso"
p_{T}	25 GeV (only for the leading electron)
Muon Baseline	
Algorithm	STACO, combined or segment-tagged muon
Acceptance	$p_{\text{T}} > 10$ GeV, $\lvert\eta\rvert < 2.4$
Quality	`Loose`
Overlap	$\Delta R(j, \mu) > 0.4$
Muon Signal	
Isolation	"tightIso"
p_{T}	25 GeV (only for the leading muon)

Electron candidates are required to be isolated, which reduces the number of electrons selected that arise from heavy hadron decays and fake electrons from hadrons that mimic electron signatures. In order to achieve higher efficiency for soft electrons while maintaining low fake rate, they are also required to satisfy the isolation "mediumIso". In events selected with Lepton trigger each of the two hard electrons is required to be "tight++", have $p_{\text{T}} > 10$ GeV and $|\eta| < 2.47$, and satisfy tight isolation. In order to correct for differences in efficiency between data and MC, a multiplicative event weight is applied for each selected electron to the overall event weight.

4.4.3 Muons

Muon candidates are constructed from track segments found in the muon chambers and the inner detector. They are required to have a hit in the innermost pixel layer, at least one hit in any pixel layer, at least 6 hits in the SCT and extension of the track in the TRT. The analysis utilizes the STACO algorithm as "combined" or "segment-tagged". "Combined" refers to the tracks that were independently reconstructed in both the Muon Spectrometer (MS) and Inner Detector (ID), and "segment-tagged" uses the MS to tag ID tracks as muons, without requiring a fully reconstructed MS track. Muon quality cuts are also defined as loose, medium and tight [83].

Muon candidates are required to have $p_{\mathrm{T}} > 6$ GeV and $|\eta| < 2.4$, and satisfy the isolation mediumIso for soft leptons in events selected with MET trigger. In events selected with Lepton trigger each of the two hard muons are required to have $p_{\mathrm{T}} > 10$ GeV and $|\eta| < 2.4$, and satisfy tight isolation. For MC, a smearing procedure must be applied to the muon p_{T}. In order to correct for differences in efficiency between data and MC, a multiplicative event weight is applied for each selected muon in MC. To avoid the presence of a "cosmic" muon, their longitudinal and transverse impact parameters must be within 1mm and 0.2 mm of the primary vertex respectively. Finally, muon candidates are required to be isolated: $\sum p_{\mathrm{T}}(\mathrm{tracks})$ in a cone of $\Delta R < 0.2$ must be less than 1.8 GeV (excluding the muon track).

Identification criteria for Jets, Electron and Muon are listed in table 4.3, 4.4 and 4.5.

4.4.4 Transverse missing energy

The presence of undetected particles can be inferred if an event has significant missing transverse momentum, E_T^{miss}. It is defined by the momentum imbalance in the plane transverse to the beam axis, where momentum conservation is expected.

$$\vec{E_T^{miss}} = -\sum_{visible\ particles} \vec{p_T} = \sum_{invisible\ particles} \vec{p_T} \tag{4.2}$$

where its magnitude is denoted by E_T^{miss}.

This sum runs over high granularity objects to improve the angular resolution. The reconstruction strategy of these well localized measurements are calibrated according to the reconstructed physics object to enhance the energy resolution. Significant E_T^{miss} is a key signature for searches in SUSY scenarios because the LSP escapes detection.

The calculation of missing transverse energy $E_{\mathrm{T}}^{\mathrm{miss}}$ is based on the modulus of the vector sum of the transverse momenta of the reconstructed objects (jets and leptons) and TopoClusters not assigned to any reconstructed object. The $E_{\mathrm{T}}^{\mathrm{miss}}$ algorithm, called `MET_EGAMMA10NoTAU`, uses calorimeter cells with $|\eta| < 4.9$, where the cells are calibrated according to the object they belong to. The muons are from the STACO container. Cluster associated with medium++ electrons with $p_T > 10GeV$, and those associated with jets with $p_T > 20GeV$ make use of the electron and jet calibration (LCW+JES) of these respective objects. Clusters of calorimeter cells with $abs(\eta) < 2.5$ not associated with these objects are calibrated using both calorimeter and tracker information [84]. The last (CellOut) term is calculated from topological calorimeter clusters at the LCW scale which are not included in any reconstructed object.

4.4.5 Overlap Removal

When jets, electrons and muons passing the object selection overlap with each other, a classification is required to remove one of them. The classification procedure removes the overlapping objects and veto the non prompt leptons to avoid the

classification of the same object in more than one particle collection and double counting. All steps are defined according to the standard SUSY Working Group overlap removal. The following scheme is applied throughout the analysis:

1. If an electron and a jet are found within $\Delta R(j, e) > 0.2$, the object is interpreted as an electron and the overlapping baseline jet is rejected.
2. If a baseline electron and a baseline jet surviving step 1 are found within $\Delta R(j, e) > 0.4$, the object is treated as a jet and the baseline electron is rejected.
3. If a baseline muon and a baseline jet surviving step 1 are found within $\Delta R(j, \mu) > 0.4$, the object is treated as a jet and the baseline muon is rejected.
4. If a baseline electron and a baseline muon surviving step 2 and 3 are found within $\Delta R(j, \mu) > 0.01$, event is rejected.
5. If a baseline electron and a baseline muon surviving step 2, 3 and 4 are found within $\Delta R(\mu, e) > 0.05$, electron with lowest p_T is rejected.

4.4.6 Pile-up Re-weighting

MC samples are often generated prior to data taking, before the exact LHC running conditions are known. With the simulation of events, a best guess of the pile-up scenario can be made. In order to match the running conditions in data, a scheme was devised to re-weight MC events. The method involves the average number of pile-up interactions (μ), computed from beam parameters where the MC events were produced with a wide variety of values of μ. The actual value of pileup-interaction in data is very different, therefore, the events in MC samples are re-weighted so that they match the data distribution of μ.

Events in MC are re-weighted using the `PileUpReweighting-00-02-05` package. The MC events are reweighed to the μ distribution corresponding to the 2012 data sample used in the analysis with a 10% scaling factor.

4.5 Event Selection

4.5.1 Trigger

The off-line event selection is designed to deliver good efficiency, starting from the choice of the triggers that the event had to satisfy in the on-line selection. Triggers used in the analysis are based on lepton criteria (soft or hard).

Both single and dilepton triggers are used for the hard leptons. The triggers used in the selection, which requires at least two good quality leptons in the final state, along with the corresponding offline p_T threshold. These are the p_T thresholds imposed on selected leptons such that they fall in the trigger efficiency plateau. Events with two leptons of different flavours might pass both the single muon and single electron triggers and thus be recorded in both the Muons and Egamma streams. In order to remove the overlap between the streams, events which pass both the single muon and single electron triggers are removed from the Muons stream and taken from the Egamma stream.

The single and di-lepton triggers are not suitable for the soft lepton because of high thresholds. Therefore, the triggers based on the missing transverse energy requirements are used to select the events for the JetTauEtmiss stream. Two triggers are employed depending on their availability in different periods. One of the triggers (EF_xe80T_tclcw) was inactive during the first few runs,leading to the efficiency on the plateau to be at 90% only. This has been taken into account by applying a 0.9 weight to MC events using a random number generator procedure. The use of EF_xe80T_tclcw loose effectively reduces the luminosity by 0.2 fb^{-1} to a total luminosity of 20.1 fb^{-1}.

All the used trigger items in the analysis are reported in table 4.6.

In MC12 simulation, the same triggers used for the data are considered

Table 4.6: Trigger items used in the analysis.

Single Electron	EF_e24vhi_medium1 or EF_e60_medium1
Single Muon	EF_mu24i_tight or EF_mu36_tight
Double Electron	EF_e24vh_medium1_e7_medium1 or EF_2e12Tvh_loose1
Double Muon	EF_mu24_tight_mu6_EFFS or EF_2mu13 or EF_mu18_tight_mu8_EFFS
Electron-Muon	EF_e12Tvh_medium1_mu8 or EF_mu18_tight_e7_medium1
MET trigger	EF_xe80T_tclcw_loose or EF_xe80_tclcw_loose

4.5.2 Event Cleaning

Several "cleaning requirements are employed to reduce non-collision backgrounds. A number of cleaning cuts are applied to ensure that data without any possible problem are selected:

1. Data quality flags defined to assess the beam stability, state of each sub-detector, noisy channels, trigger system and performance of object reconstructionare stored and collected into a GoodRunsList (GRL). The first type of events are required to have been recorded in "good luminosity blocks listed in the "GRL.
2. In LAr calorimeter, the global noise bursts appear and disappear on a time scale smaller than a luminosity block. The events taken during improper function of the LAr and Tile calorimeters are rejected.
3. TileTrip events must be rejected. These trips are considered a tolerable DQ defect as the energy in an unpowered module is extrapolated from its neighbors during off-line reconstruction [85] [86].
4. Dead tile events are rejected which prevents fake E_T^{miss} arising from non-operational cells in the Tile and the HEC calorimeters. The event must not contain any selected jet with $p_T > 40$ GeV and the fraction of energy in bad cells (BCH CORR JET)≥ 0.05 and $\Delta\phi(jet, E_T^{miss}) < 0.3$.

5. Multiple pp collisions or pile-up may result in several reconstructed primary vertices per event. The primary vertex must be associated with at least five tracks in order to ensure that it is well reconstructed.
6. Muons with a longitudinal impact parameter larger than 1 mm or transverse impact parameter larger than 0.2 mm with respect to the primary vertex are believed to be of cosmic ray origin and the event is rejected. The cut is applied after overlap removal to avoid removal of muons from heavy flavor decays.
7. Some jets measured with the calorimeter may not be produced by protonproton collisions, called fake jets. These events are also rejected if they contains at least one jet with $p_T > 20$ GeV failing the VeryLooseBad criteria defined by the JetEtMiss group [87].
8. The leading jets (up to two of them) with $p_T > 100$ GeV and $|\eta| < 2$ must have a charged track p_T fraction $f_{ch} > 0.02$, and, if the EM fraction f_{EM} is > 0.9, it must have $f_{ch} > 0.05$. This cut is very effective at rejecting events where the leading jets have not been generated by a hard interaction, the probability of having noncollision backgrounds in events with more than four jets is found to be negligible [88].
9. The energy weighted mean time of jets is required to be smaller than 5 ns.
10. In order to correct for the different electron and muon reconstruction efficiencies in data and MC, an event weight is applied in MC events to each signal lepton.

4.5.3 Final Selection

Events are required to contain exactly two opposite charge leptons.The dilepton invariant mass m_{ll} is asked to be greater than 8 GeV for soft leptons and 20 GeV for hard leptons in order to remove low-mass resonances and to take into account, in case of SF, the lack of Monte Carlo simulated Drell-Yan samples for very low-mass.

To reduce the Z+Jet background for the SF, a cut $(M_{ll} - 90) > 20GeV$ is applied only for hard leptons.

To reach the efficiency plateau for the trigger items used in the analysis, for MET triggered events $E_T^{miss} > 120\ GeV$ is requested. For Lepton triggered events, at least one lepton must satisfy the leading requirement (> 25 GeV for electrons and for muons).

Then, in both cases, events are retained only if they contain at least two jets with > 20 GeV. For the soft leptons, b tagging is applied only in the Signal region to reduce the Z+Jet background.

4.5.4 Cutflow

In the following section, the list of the applied cuts is provided for MET trigger and Lepton trigger, along with corresponding cutflow chart (figure 4.5). The numbers of data events, and MC events are shown in the table 4.7, 4.8,4.9 and 4.10. In the latter case, the numbers relative to both the main background sources and a point of the signal grid used as a reference are provided.

1. **GRL:** GoodRunLists selection applied.
2. **LArError!=2, TileError!=2 and CoreFlags**: Select events with no error from the LAr and Tile quality assessment.
3. **Smart Veto**: Reject events failing the smart LAr veto.
4. Reject events containing one or more jets that point to the dead-FEB region of the LAr Calorimeter.
5. **Trigger selection:** Select events satisfying the appropriate trigger requirements. No trigger matching is required.
6. **Jet Cleaning**: Reject events with one or more jets failing the jet quality criteria.

7. **Primary Vertex:** Select events where the first primary vertex is associated with at least 5 tracks.
8. **Cosmic Veto:** Reject events that contain at least one muon failing the cosmic rejection cuts.
9. **Exactly two leptons:** Select events with exactly two leptons.
10. **2 tight leptons:** Selected leptons are required to be tight according to the CP prescriptions.
11. **Sign:** keep events only if the two leptons have opposite charges.
12. **Lepton invariant mass(m_{ll})**: Only accept events where the invariant mass of the leptons exceeds 20 GeV lepton trigger events and 8 GeV for MET trigger events.
13. **Leading lepton** p_T: Only accept events where the most energetic lepton exceeds 25 GeV for lepton trigger events.
14. **Two Jets > 20 GeV:** Two Jets with at least 20 GeV are required.
15. **Z veto:** Reject events if the invariant mass of the leptons lies within 20 GeV of the Z mass (defining $m_Z = 91$ GeV) for lepton trigger events.

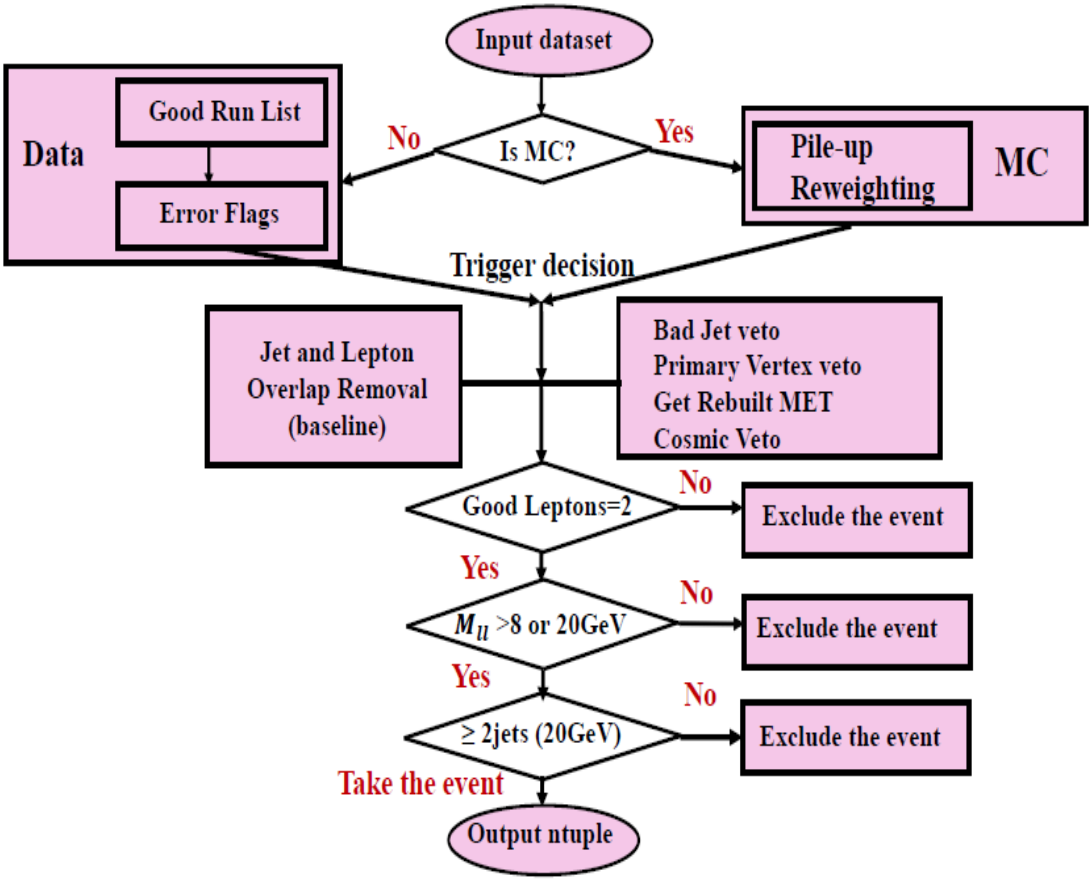

Figure 4.5: Analysis cutflow

Table 4.7: Number of data events triggered with Lepton trigger passing the analysis cuts in 2012 periods A-L .

Cuts	**Egamma stream**	**Muon Stream**
Total	521920023	408188609
GRL	498707550	381185339
LArError==0,TileError==0 and CoreFlags	497615014	390350034
Trigger	347701567	263776989
Jet Cleaning	346417262	263013860
Primary Vertex	343028646	259145841
Cosmic muon veto	341409748	250180747
Energy averaged time	338835365	248014728
Bad Leading Jet	338438339	247895898

	$e^{\pm}e^{\mp}$	$\mu^{\pm}\mu^{\mp}$	$e^{\pm}\mu^{\mp}$
Two Baseline Leptons 10 GeV OS	10268387	13721259	3089336
Two "Tight Leptons" OS	6644638	11011280	225296
Leading Leptons $p_T > 25$ GeV	6070228	9478653	143478
$m_{ll} > 20$ GeV	5988062	9445410	139871
Two Jet $p_T > 20$ GeV	527829	820039	64505

Table 4.8: Number of data events triggered with MET trigger passing the analysis cuts in 2012 periods A-L .

Cuts	**JetTauEtmiss Stream**
Total	749085795
GRL	702046079
LArError==0, TileError==0 and CoreFlags	700303143
Trigger	70290549
Smart Veto	68330592
Jet Cleaning	66023620
Primary Vertex	65921788
Cosmic muon veto	65511717
Energy averaged time	65250309
Bad Leading Jet	63220627

	$e^{\pm}e^{\mp}$	$\mu^{\pm}\mu^{\mp}$	$e^{\pm}\mu^{\mp}$
Two Baseline Leptons 7/6 GeV OS	51338	307656	89536
$m_{ll} > 8$ GeV	49102	255042	66155
Two Jet $p_T > 20$ GeV	21730	146441	48735
$E_T^{miss} > 120\ GeV$	7000	5920	12501

Table 4.9: Expected number of MC Lepton triggered events for some of the main background sources to opposite-sign ee (top), $\mu\mu$ (middle), $e\mu$ (bottom) channels for an integrated luminosity of 20.3 . The number of expected events for the point of the signal grid with stop mass of 300 GeV, chargino mass of 250 GeV and neutralino mass of 50 GeV is also listed.

Cuts ↓ MC →	$t\tilde{t}$	Dibosons	Z	MC total	Signal(250,50)
Total no. of Events	539146	212279	82773597.7	106617020	22504.3
Cuts ↓ MC → ($e^{\pm}e^{\mp}$)	$t\tilde{t}$	Dibosons	Z	MC total	Signal
Trigger	236212	67967.4	18843332	20216649	7464.4
Jet Cleaning	235535	67854.8	18775143	20144663	7431.2
Primary Vertex	235352	67012.7	18203513	19551962	7430.0
CosmicVeto	233966	66816.6	18179706	19525356	7383.2
Bad Leading Jet	233036	66274.3	18050046	19386409	7372.4
2 OS Tight Leptons (10 GeV)	27849	7958.4	6939278	7298825.2	288.2
Leading lepton ($p_T > 25$ GeV)	27168	7573.4	6647840	6813742.4	285.5
2 Jets $p_T > 20$ GeV	26487	7359.0	5810823	5912106.2	284.0
$m_{ll} > 20$ GeV	27368	1183.3	486453.3	528811.9	216.6
Cuts ↓ MC → ($\mu^{\pm}\mu^{\mp}$)	$\tilde{ttbar}$	Dibosons	Z	MC total	Signal
Trigger	243199	70264	19863276	21880515	7406.5
Jet Cleaning	242538	70157	19798236.5	21810688	7368.5
Primary Vertex	242342	69211	19087548.9	21055056	7367.1
CosmicVeto	240033	68585	18682947.7	20627720.5	7275.7
Bad Leading Jet	239191	68008	18487300.1	20415080.4	7249.4
2 OS Tight Leptons (10 GeV)	36720	11558.4	10658517.6	11519936.9	329.9
Leading lepton ($p_T > 25$ GeV)	35385	10692.1	9986394.1	10265272.6	326.4
$m_{ll} > 20$ GeV	35366	10663.3	8795158.2	8959878.7	325.5
2 Jets $p_T > 20$ GeV	30508	1571.4	697128.3	765888.5	264.6
Cuts ↓ MC → ($e^{\pm}\mu^{\mp}$)	$t\tilde{t}$	Dibosons	Z	MC total	Signal
2 OS Tight Leptons 10 GeV	64150.8	13938.9	90053.6	175972.3	638.8
Leading lepton ($p_T > 25$ GeV)	62150.4	12952.3	59501.0	141608.1	631.3
2 Jets $p_T > 20$ GeV	60589.9	12530.9	55058.5	134766.7	624.4
$m_{ll} > 20$ GeV	52310.2	1704.2	6083.8	63219.8	484.7

Table 4.10: Expected number of MC MET triggered events for some of the main background sources to opposite-sign ee (top), $\mu\mu$ (middle), $e\mu$ (bottom) channels for an integrated luminosity of 20.1 . The number of expected events for the point of the signal grid with stop mass of 300 GeV, chargino mass of 150 GeV and neutralino mass of 130 GeV is also listed.

Cuts ↓ MC	$t\tilde{t}$	Dibosons	Z	MC total	Signal
Total	539146	212279	82773597	106617020	33642
Trigger	185951	64210	17695	1056476	26249.5
Jet Cleaning	185457	63988	17656	1050470	26114.6
Primary Vertex	185322	63928	17570	1047859	26089.8
CosmicVeto	182980	63196	17477	1031115	25954.2
Energy averaged time	182874	63156	17426	1030292	25947.2
Bad Leading Jet	181954	62707	17316	1024596	25804.0
Exactly 2 baseline leptons	70863	6641	7005.4	490679	600.4
Cuts ↓ MC → $(e^{\pm}e^{\mp})$	t	Dibosons	Z	MC total	Signal
2 OS Baseline Leptons (7 GeV)	14053	1675.7	6894.7	24434.2	107.4
$m_{ll} > 8GeV$	13940	1646.2	4006.9	21344.5	95
2 Jets $p_T > 20GeV$	12054	467.9	2250.6	15820	88.0
$E_T^{miss} > 120GeV$	4574	227.9	495	5647	64
Cuts ↓ MC → $(\mu^{\pm}\mu^{\mp})$	t	Dibosons	Z	MC total	Signal
2 OS Baseline Leptons (6 GeV)	17572	1365.1	471222	519040	147.7
$m_{ll} > 8GeV$	17419	1280.5	237131.9	284210	132.3
2 Jets $p_T > 20GeV$	15789	752.6	124466.8	156576	94.0
$E_T^{miss} > 120GeV$	4313.0	227.9	571.6	5435.4	89.0
Cuts ↓ MC → $(e^{\pm}\mu^{\mp})$	t	Dibosons	Z	MC total	Signal
2 OS Baseline Leptons (7/6 GeV)	35345	3205.1	7554.5	53062.7	236.7
$m_{ll} > 8GeV$	35069.6	3173.7	7494.3	49333.7	218.9
2 Jets $p_T > 20GeV$	30702.3	1000.5	3872.3	37760.2	2112.2
$E_T^{miss} > 120GeV$	8736.1	329.8	894.2	10538.0	167.9

CHAPTER 5

Signal from Background Separation

5.1 Multivariate Analysis Technique

Multivariate analysis (MVA) is a statistical tool to separate the signal from the background as much as possible, using the information provided by many variables. It provides a better method to enhance the signal-to-background ratio with respect to the cut-based analysis by combining multiple random variables and study their distributions simultaneously. This may reduce the complexity of many problems and allow to take correlations between the different variables into account.

MVA is based on machine learning methods able to separate a given signal from backgrounds (classification) or to estimate the most compatible value of a given observable given a set of input variables correlated with the observable of interest (regression). Classification is a supervised learning process, which is represented by a mathematical model. The aim is to predict class labels of objects with a specific set of input variables available for discrimination. It offers parameters that can be trained, using a training data sample of which all elements class labels are known. A regression is the process that estimates the parameter values of a function, which predicts the value of a response variable in terms of the values of other variables [89].

There are variety of multivariate analysis methodologies to choose from, which work quite differently with its own unique characteristics. Most MVA methods have three phases: training, testing.

We teach MVA how to discriminate between signal and background events during the training. The training program is provided MC background and signal

samples so that it can learn the characteristics of each. Once a classifier is trained, it can be applied to any event, and return a classification response. The response is usually a single numerical value which gives the idea of "signal-like" or "background-like" distribution.

For unbiased results, we use a testing sample which is orthogonal to the training sample. During the testing phase, we observe the classifier performance to check its response and how well it separates signal from background. To do this, we optimize the classifier by choosing the cut on the classifier response which maximizes our significance. An overtraining check is usually done to avoid that the training step was specific to the input sample. MVA can be fit to more degrees of freedom than exist in the distribution it is being trained on, called overtraining. In this case, the classifier becomes sensitive to the statistical fluctuations in the training sample and poor performance on any sample it was not trained on. The distributions of the training and testing samples can be compared to test the overtraining. The two distributions should match to within statistical errors to avoid overtraining.

In the application phase we implement the classifier response during the final analysis. At this phase, the data classification uses a reader class, which reads and interprets the weight files. Application is applied to the data to be analyzed and use the cut on MVA classifier response as the final cut for the analysis.

5.2 Boosted Decision Trees (BDT)

Several discrimination methods implemented in MVA were tested, but the best discriminating power was achieved with a Boosted Decision Trees technique (BDT) using a Gradient boosting algorithm (BDTG) [90].

Boosted Decision Trees (BDT) is a type of multivariate analysis classifier in which a binary tree structure is built in order to separate signal from background

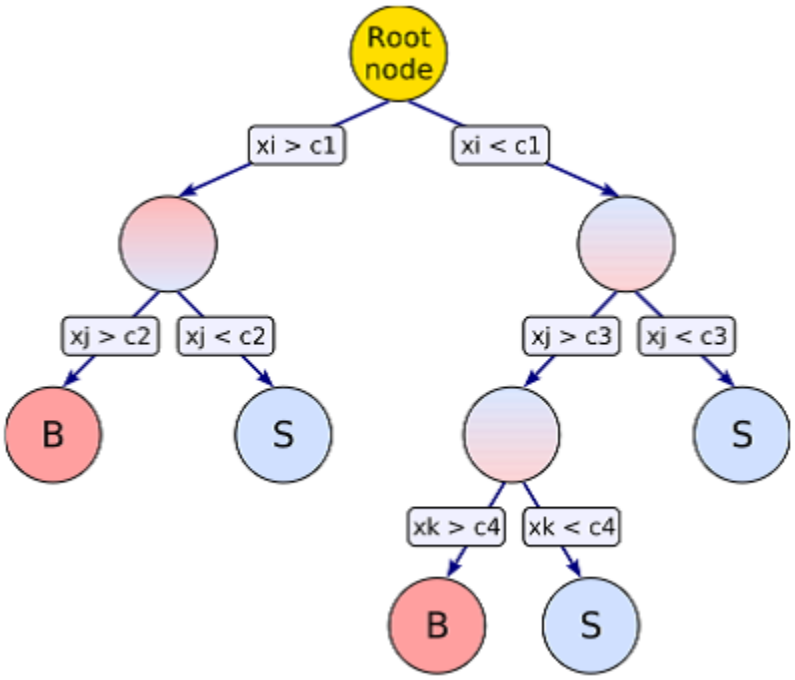

Figure 5.1: Illustration of a Boosted Decision Tree structure.

events. Each event is classified by running it through several decision trees. It starts with a root node and the sequential and successive binary cuts are applied in the different nodes until the last ones, called leafs, which classify the events as background or signal, like shown in figure 5.1.

For every event, the classification starts at the root node level, and proceeds downwards. A binary test cut is applied on the variable x_i and the events are split into two other nodes depending on whether they pass the cut or not. Based on the results of each test, the events proceed down to one of two nodes, which applies another test. This process continues until either some maximum depth or number of nodes is reached, or prescribed signal purity is achieved. Each event is then classified

into signal-type (S) or background-type(B) depending on the majority of events of each kind. The node purity is defined as:

$$p = \frac{\sum_S W_S}{\sum_S W_S + \sum_B W_B} \tag{5.1}$$

where $W_{S(B)}$ is the weight of the signal (background) event and $\sum_{S(B)}$ is the sum over the signal (background) events. To test at each node is chosen such that it maximizes the separation between background and the signal events in its daughter node. We use the Gini index G(p) which parametrizes the degree of separation, defined as:

$$G(p) = p(1-p) \tag{5.2}$$

where p is the purity of the nodes (equation 5.2). The growing process iterates the spiting procedure by maximize the gain, as follows. First, the total number of background and signal events are normalized separately. The decision tree is then grown node by node. The training procedure selects the variable and the cut value to maximize the gain in the Gini index G(p) between the parent node and the sum of the indices of the two daughter nodes. The daughter nodes now become parents, and the process is iterated until either the tree is grown to a maximum size, or the tree reaches a predefined purity.

Decision trees are known to be sensitive to the statistical fluctuations in the input variables used to create the tree structure. Also, decision trees are prone to overtraining. These problems can be alleviated by applying the boosting procedure. The boosting process produces multiple small decision tress, each trained with a different set of event weights applied to the training samples. The set of trees are collected into a single boosted tree classifier and the response is a weighted average

of the individual tree response. The idea behind the boosting is that the events that were misclassified during the training of a decision tree are given a higher common event weight in the training of the following tree.

There are two choices of boosting method: AdaBoost (Adaptive) and GradientBoost. AdaBoost is a powerful, commonly used boosting method, but its exponential loss-function can lead to instability in noisy settings. The gradient boosting potentially ensures more robustness to BDT method, without spoiling the performance. We used GradientBoost in this analysis.

5.3 Toolkit for the Multivariate Analysis (TMVA)

The Toolkit for Multivariate Analysis (TMVA) provides a ROOT-integrated [89] environment for the application of multivariate classification. TMVA consists of object-oriented implementations in C++ of a number of multivariate methods and visualization scripts. The training and testing steps are performed with datasets where the true event classification is known. After applying few additional preselection cuts (section 5.4) helps to reduce the analysis execution time without affecting the final performance, both signal and background MC samples were split in two halves. The first half was used for the training phase and the second half for the testing. In particular, odd-numbered events were used for the training while even-numbered events were used for testing and performance evaluation. With the goal of maximizing the sensitivity of the analysis, different discrimination methods were applied in TMVA with several signal samples, corresponding to all the points on the signal grid. The parameters of each method were tuned in order to improve the discriminating power. All baseline background processes in table 4.1 were used for the training. Given the total integrated luminosity, the weight associated to each single event in both signal and background samples properly took into account the cross section of the corre-

sponding process, as well as the correction factors. In the training phase, similar to what done for the electron-muon pairs (DF), same flavour muon and electron pairs were collected in a single sample (SF). In the case of the SF channel, the training took a more relevant advantage of the increased statistics with respect to the choice of considering muons and electrons separately. Events with negative weights (simulated MC@NLO samples) were ignored in the training while they were considered in the application phase.

5.4 Pre-selection Cuts

Two different sets of pre-selection cuts are applied to MET triggered events and to Lepton triggered events, in addition to the event selection. The pre-selection cuts are applied before analyzing them with the multivariate technique in order to remove low-mass resonances, take into account the lack of MC simulated Drell-Yan samples for very low-mass in the case of SF and optimize the signal sensitivity over the $m(\chi_1^0) - m(\chi_1^\pm)$ plane:

- **(MET Trigger: MC1)** $m_{ll} > 8\ GeV$;
- **(Lepton trigger: LC1)** $>$ 50 GeV, $m_{ll} > 20\ GeV$ and $m_{eff} >$ 200 GeV . In case of SF a Z veto is applied: lepton invariant mass (m_{ll}) outside the window [71 GeV, 111 GeV] is requested;
- **(Lepton trigger: LC2)** $>$ 50 GeV, $m_{ll} > 20\ GeV$ and $m_{eff} >$ 300 GeV. In case of SF a Z veto is applied: lepton invariant mass (m_{ll}) outside the window [71 GeV, 111 GeV] is requested;

Table 5.1: Expected number of SM background events (statistical errors only) and their composition after preselection cuts MC1, LC1, LC2, in DF channel and in SF channel.

Process	DF MC1	DF LC1	DF LC2	SF MC1	SF LC1	SF LC2
total SM	5956.81	38965.5	23195.31	6155.47	33709.9	21059.12
$t\tilde{t}$	94.2%	89.8 %	90.8 %	93.2 %	74.0 %	80.2 %
$t\tilde{t}$ W,$t\tilde{t}Z$, $t\tilde{t}WW$	0.4 %	0.2 %	0.3 %	0.4 %	0.2 %	0.3 %
Z	0.7 %	3.2 %	2.3 %	1.2 %	14.5 %	10.4 %
Wt, Zt	4.4 %	4.6 %	4.2 %	4.7 %	3.8 %	3.8 %
Drell-Yan	0.01 %	0.01 %	0.0 %	0.06 %	4.8 %	2.9 %
$WW + WZ + ZZ$	0.3 %	2.5 %	2.3 %	0.4 %	2.2 %	2.2 %
H	0.03 %	0.1 %	0.1 %	0.1 %	0.2 %	0.2 %

5.5 Discriminative Variables

Discriminative variables for the multivariate analysis are chosen aiming at the following requirements:

- The distribution of the variables are expected to be different as much as possible in signal and background events;
- Their distributions in data are expected to be accurately reproduced by MC simulation;
- The input variables are not highly correlated to each other.

Several variables were considered as input for the training procedure, but finally 12 were used, according to their effectiveness in discriminating signal from background and to their agreement in data-MC comparison. The details of these variables are given below.

- Missing transverse energy (E_T^{miss})
- leptonic m_{T2}
- hadronic m_{T2}
- $\Delta\phi(l_1 - l_2)$, the ϕ angle between the two leptons

- $\Delta\eta(l_1 - l_2)$ between the two leptons
- $\Delta\phi(E_T^{miss} - l_1)$, the ϕ angle between (E_T^{miss}) and the most energetic lepton
- $\Delta\phi(j_1 - l_1)$, the ϕ angle between the most energetic jet and the leading lepton
- $\Delta\phi(E_T^{miss}, p_{Tb}^{ll}$, he ϕ angle between (E_T^{miss}) and p_{Tb}^{ll} (where p_{Tb}^{ll} is the vectorial sum p_{Tb}^{ll} =(E_T^{miss}) + $\mathrm{p}_T^{l_1} + p_T^{l_2}$)
- $\sum_{i=1,2} p_T^{l_i}$, the scalar sum of the transverse momenta of the two leptons
- $\sum_{i=1,2} p_T^{j_i} / \sum_{i=1,2} p_T^{l_i}$, where $\sum_{i=1,2} p_T^{j_i}$ is the scalar sum of the transverse momenta of the two most energetic jets
- $E_T^{miss} / \sum_{i=1,2} p_T^{l_i}$
- M_{ll}, lepton invariant mass (used only for hard leptons).

In particular, $\sum_{i=1,2} p_T^{l_i}$, $\sum_{i=1,2} p_T^{j_i} / \sum_{i=1,2} p_T^{l_i}$ and $E_T^{miss} / \sum_{i=1,2} p_T^{l_i}$ variables are quite sensitive to the mass splittings $\tilde{t} - \tilde{\chi}^{\pm}$ and $\tilde{\chi}_1^{\pm} - \tilde{\chi}_1^0$. e.g., signal points with small $\Delta m(\tilde{\chi}_1^{\pm} - \tilde{\chi}_1^0)$ are expected to be characterized by leptons of low momenta and large $(E_T^{miss}) / \sum_{i=1,2} p_T^{l_i}$ values.

A reasonable agreement is observed for the all the input variables between data and MC. All the input variable distributions are shown after cuts MC1 (Figures 5.10 and 5.11) and LC1 (Figures 5.12 and 5.13) for the 2012 data and for all background sources with two isolated leptons. DF and SF distributions are shown separately. For comparison, the distributions for the reference signal point with a scalar top mass of 300 GeV and $m(\tilde{\chi}_1^{\pm}, \tilde{\chi}_1^0)$ = (150,130) GeV (Figures 5.10 and 5.11) and for the signal point with a scalar top mass of 300 GeV and $m(\tilde{\chi}_1^{\pm}, \tilde{\chi}_1^0)$ = (250,50) GeV (Figures 5.12 and 5.13) are also reported in the plots. Only statistical errors are shown in the figures. The residual discrepancies are found to be fully within systematic errors for DF and SF channels.

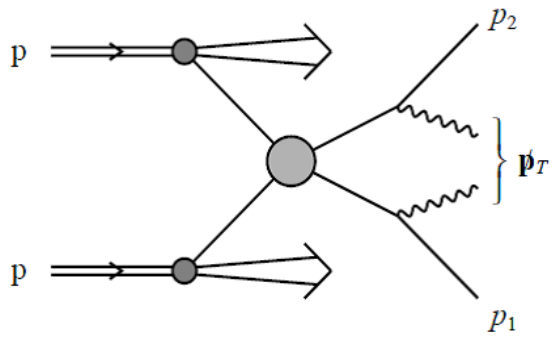

Figure 5.2: Event topology of the variable m_{T2}, where two particles are pair-produced which both decay semi-invisibly. The visible decay products have momenta p_1 and p_2, whilst the invisibly decaying particles have combined missing transverse momentum of p_T

5.5.1 Stransverse Mass (m_{T2})

The "Stransverse Mass" (m_{T2}), is an event variable used to bound the masses of an unseen pair of particles which are presumed to have decayed semi-invisibly into particles which were seen [91] [92]. Therefore, m_{T2} is a function of the momenta of two visible particles and the missing transverse momentum in an event. This quantity is defines as:

$$m_{T2}(p_{T_1}, p_{T_2}, q_T) = \min_{q_{T_1}+q_{T_2}=q_T} \{max[m_T(p_{T_1}, q_{T_1}), m_T(p_{T_2}, q_{T_2})]\} \tag{5.3}$$

where m_{T2} is the stransverse mass, p_{T_1} and p_{T_2} are the transverse momentum vectors of two particles, which are assumed to be massless and p_{T_1} and p_{T_2} are the vectors with $q_T = q_{T_1} + q_{T_2}$. The minimization is performed over all the possible decompositions of the q_T. For the leptonic m_{T2}, if the transverse momenta of the two leptons in each event are p_{T_1} and p_{T_2}, and E_T^{miss} as q_T, $m_{T2}(l_1, l_2, E_T^{miss})$ is bounded above by the W boson mass [93] [94]. The upper bound is strongly correlated with the mass difference between the chargino and the neutralino. For the hadronic m_{T2},

the transverse momenta of the two jets in the event are p_{T_1} and p_{T_2}, and the lepton transverse momenta are added vectorically to the E_T^{miss}) in the event to form q_T, resulting $m_{T2}(j_1, j_2, l_1 + l_2 + E_T^{miss})$. It has very different kinematic limit where the top quark decay bound is strongly correlated to the mass difference between the top squark and the chargino.

5.6 Reference Points and Parameter Optimization

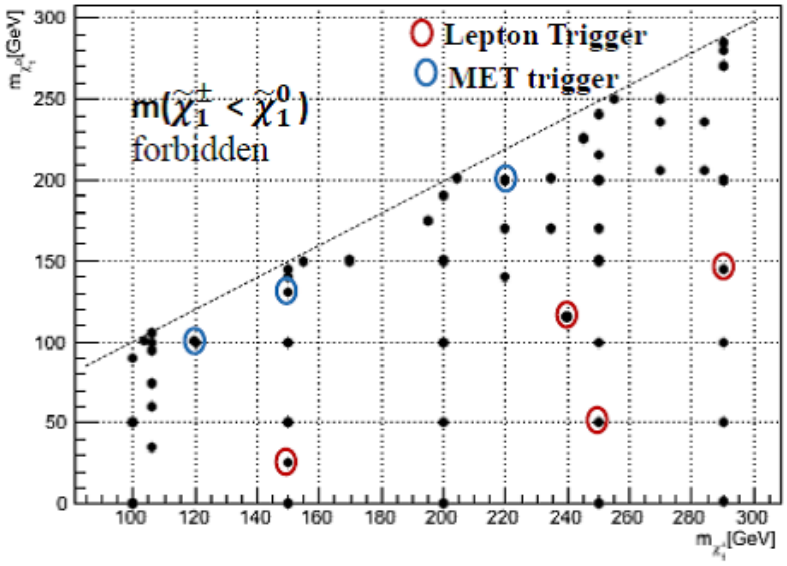

Figure 5.3: The grid of signal points in the $m(\tilde{\chi}_1^{\pm}) - m(\tilde{\chi}_1^0)$ for the $m(\tilde{t}) = 300$ GeV. The reference point chosen for soft leptons are in blue, while the ones for hard leptons are in red.

In order to teach TMVA how to discriminate signal from the background, seven different reference points are used all over the grid listed in table 5.2. Three points correspond to the soft leptons and four points corresponds to the hard leptons. MVA reference points are chosen to increase discrimination power and sensitivity across the

plane and keep statistics. These points are considered, to obtain the final definition of signal regions.

Table 5.2: Reference points (RP) chosen for DF and SF trainings in MET and Lepton triggered events.

	Trigger	Event category	$m_{\tilde{\chi}_1^\pm}$ (GeV)	$m_{\tilde{\chi}_1^0}$ (GeV)
RPA	MET	DF, SF	120	100
RPB	MET	DF, SF	150	130
RPC	MET	DF, SF	220	200
RPD	Lepton	DF	150	25
RPE	Lepton	DF, SF	250	50
RPF	Lepton	SF	240	120
RPG	Lepton	DF	290	145

For the analysis, a number of nominal parameters are used to control the BDTG process. Given the presently available Monte Carlo statistics, the number of individual decisions (`nTrees`) range between 200 and 1200 for DF and SF channel. The BDTG classifier response distribution can be changed based on the choice of `nTrees`. As `nTrees` decreases, the classifier response is compressed in a smaller range than the usual [-1,+1] interval. The default value of `nCuts`=20 realizes a good compromise between computing time and granularity. `nCuts` is a parameter which decides the granularity of the input variables in order to set a cut value which optimize the separation for each tree. Usually a larger granularity doesn't increase noticeably the performance of the method. `NNodesMax` is the maximum value of nodes inside each single tree. For Gradient boosting a limited `NNodesMax` is recommended. In this analysis, `NNodesMax`=5 considered to avoid the overtraining problems.

The BDTG classifier response distribution, shown in figure 5.4 after cuts LC2 and MC1 as an example, indicates that there is an excellent separation between the

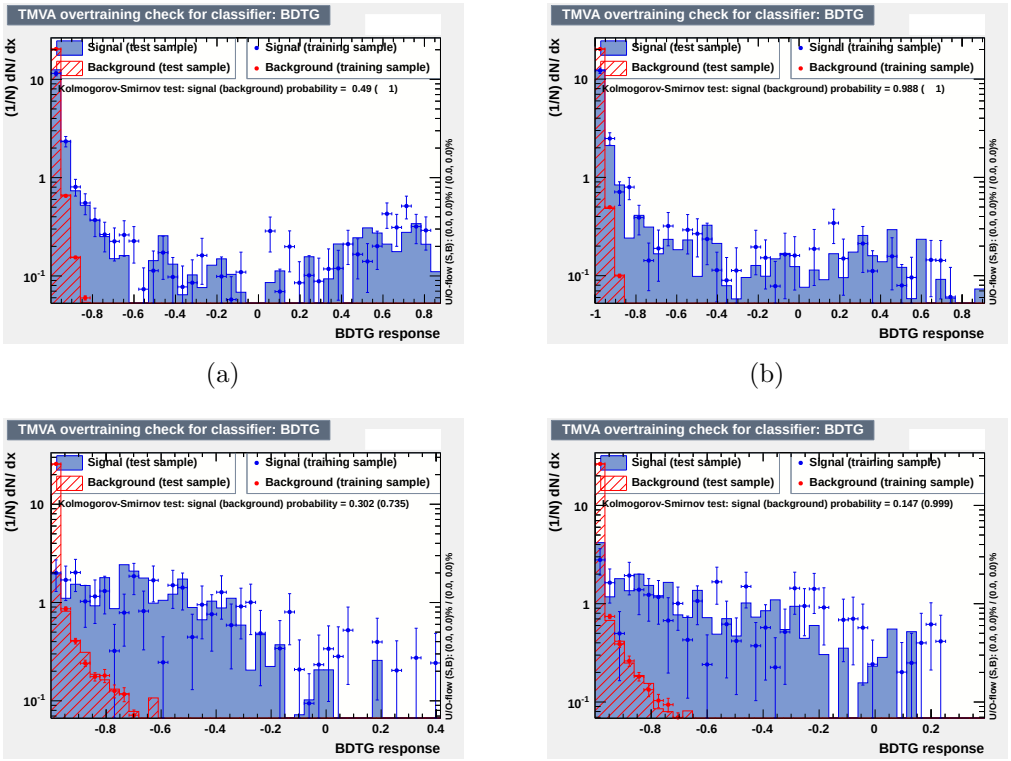

Figure 5.4: BDTG classifier response distributions for trained (dots) and tested (histogram) events are shown after cuts LC2 (a) for DF and (b) for SF channels and after cuts MC1 (c) for DF and (d) for SF. The plots on top refer to the signal point with a scalar top mass of 300 GeV and $m(\tilde{\chi}_1^{\pm}, \tilde{\chi}_1^0) = (250,50)$ GeV and the one on bottom to the signal point with a scalar top mass of 300 GeV and $m(\tilde{\chi}_1^{\pm}, \tilde{\chi}_1^0) = (150,130)$ GeV. Signals are in blue, while backgrounds are in red.

background and the signal reference point RPE, while the discrimination becomes less pronounced for the point RPB. In figure 5.4, BDTG classifier response distributions for trained (dots) and tested (histogram) events are shown for trained (dots) and tested (histogram) events after cuts LC2 and MC1. Signal is in blue while background is in red. Training and the testing distributions are in good agreement. Figure 5.5 shows the resulting background rejection versus signal efficiency for DF (left) and SF (right) channels after cuts LC2 and MC1, for RPE and RPB as provided in the output of the training procedure. These curves suggest that at a fixed efficiency value,

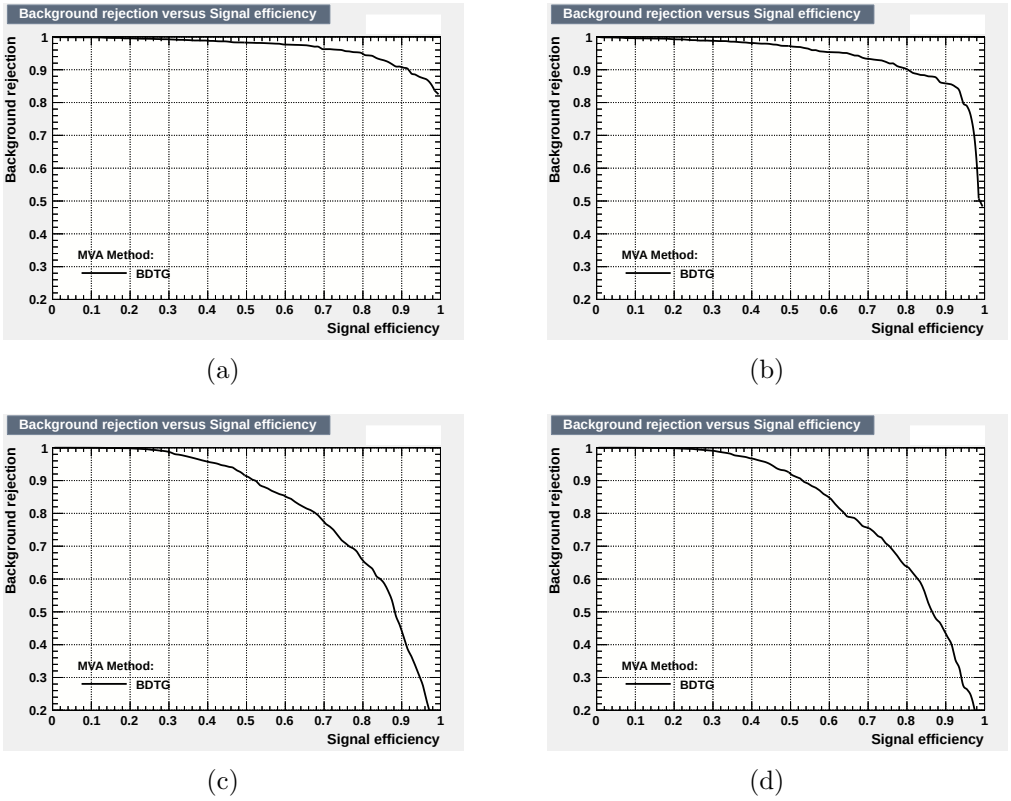

Figure 5.5: Background rejection versus signal efficiency using BDTG method. The plots on top refers to the signal point with a scalar top mass of 300 GeV and $m(\tilde{\chi}_1^{\pm}, \tilde{\chi}_1^0)$ = (250,50) GeV and to DF(left) and SF(right) channels. The plots on bottom to the signal point with a scalar top mass of 300 GeV and $m(\tilde{\chi}_1^{\pm}, \tilde{\chi}_1^0)$ = (150,130) GeV and to DF(left) and SF(right) channels.

the rejection for DF is higher than for SF. However, this doesn't imply that the final sensitivity obtained with DF is higher than for SF channel.

For every reference point training is performed, which gives the corresponding "rank" of the input variables. The ranking is based on their discrimination power and their correlation with the BDTG value, shown in table 5.3, 5.4, 5.5 and 5.6. This variable ranking is different for DF and SF channels and depends on the reference signal point. For example, for the reference points chosen close to the grid diagonal,

Table 5.3: Ranking of the input variables to the signal point with a scalar top mass of 300 GeV and $m(\tilde{\chi}_1^{\pm}, \tilde{\chi}_1^0) = (250,50)$ GeV for DF channel

Rank	Variable	Variable Importance
1	leptonic m_{T2}	2.876e-01
2	E_T^{miss}	1.972e-01
3	$\sum_{i=1,2} p_T^{l_i}$	1.189e-01
4	hadronic m_{T2}	1.022e-01
5	$\sum_{i=1,2} p_T^{j_i} / \sum_{i=1,2} p_T^{l_i}$	5.712e-02
6	$\Delta\phi(E_T^{miss}, p_{Tb}^{ll})$	5.376e-02
7	$\Delta\phi(E_T^{miss} - l_1)$	5.218e-02
8	M_{ll}	5.088e-02
9	$\Delta\phi(l_1 - l_2)$	5.046e-02
10	$\Delta\phi(j_1 - l_1)$	5.011e-02
11	$E_T^{miss} / \sum_{i=1,2} p_T^{l_i}$	1.593e-02
12	$\Delta\eta(l_1 - l_2)$	1.445e-02

the variables $\sum_{i=1,2} p_T^{l_i}$, $\sum_{i=1,2} p_T^{j_i} / \sum_{i=1,2} p_T^{l_i}$ and $E_T^{miss} / \sum_{i=1,2} p_T^{l_i}$ are higher in raking compare to other reference points.

In figure 5.6 and 5.7, the linear correlation coefficients among the different input variables are shown after cuts LC1 and MC1 for DF and SF channel for signal (on the left) and background (on the right). It can be observed that all variables are generally poorly (anti)correlated except in some expected cases. There is no negative impact of highly correlated variable because of robustness of BDTG method. A similar behavior was observed for all other reference points.

Some of the input variable distributions (E_T^{miss}, m_{ll}) are shown, after the event selection, in figure 5.8 for DF and SF channels and the reference signal points RPA and RPB for MET triggered events. The same variables are shown in figure 5.9 for DF and SF channels and the reference signal points RPD, RPE and RPF for Lepton triggered events.

Table 5.4: Ranking of the input variables to the signal point with a scalar top mass of 300 GeV and $m(\tilde{\chi}_1^{\pm}, \tilde{\chi}_1^0)$ = (250,50) GeV for SF channel

Rank	Variable	Variable Importance
1	leptonic m_{T2}	1.900e-01
2	hadronic m_{T2}	1.226e-01
3	M_{ll}	1.112e-01
4	E_T^{miss}	1.088e-01
5	$E_T^{miss}/\sum_{i=1,2} p_T^{l_i}$	9.185e-02
6	$\Delta\phi(j_1 - l_1)$	8.226e-02
7	$\Delta\phi(E_T^{miss}, p_{Tb}^{ll})$	6.917e-02
8	$\Delta\phi(l_1 - l_2)$	6.048e-02
9	$\Delta\eta(l_1 - l_2)$	4.437e-02
10	$\Delta\phi(E_T^{miss} - l_1)$	4.304e-02
11	$\sum_{i=1,2} p_T^{j_i}/\sum_{i=1,2} p_T^{l_i}$	3.995e-02
12	$\sum_{i=1,2} p_T^{l_i}$	3.629e-02

Table 5.5: Ranking of the input variables to the signal point with a scalar top mass of 300 GeV and $m(\tilde{\chi}_1^{\pm}, \tilde{\chi}_1^0)$ = (150,130) GeV for DF channel

Rank	Variable	Variable Importance
1	$E_T^{miss}/\sum_{i=1,2} p_T^{l_i}$	3.901e-01
2	$\sum_{i=1,2} p_T^{j_i}/\sum_{i=1,2} p_T^{l_i}$	3.156e-01
3	$\Delta\phi(E_T^{miss} - l_1)$	5.988e-02
4	hadronic m_{T2}	5.332e-02
5	$\Delta\phi(j_1 - l_1)$	3.726e-02
6	leptonic m_{T2}	3.354e-02
7	$\sum_{i=1,2} p_T^{l_i}$	2.954e-02
8	$\Delta\phi(l_1 - l_2)$	2.801e-02
9	E_T^{miss}	2.744e-02
10	$\Delta\eta(l_1 - l_2)$	2.525e-02
11	$\Delta\phi(E_T^{miss}, p_{Tb}^{ll})$	0.000e+00

Table 5.6: Ranking of the input variables to the signal point with a scalar top mass of 300 GeV and $m(\tilde{\chi}_1^{\pm}, \tilde{\chi}_1^0) = (150,30)$ GeV for SF channel

Rank	Variable	Variable Importance
1	$E_T^{miss} / \sum_{i=1,2} p_T^{l_i}$	4.797e-01
2	$\sum_{i=1,2} p_T^{j_i} / \sum_{i=1,2} p_T^{l_i}$	3.436e-01
3	$\Delta\phi(E_T^{miss} - l_1)$	5.669e-02
4	hadronic m_{T2}	4.957e-02
5	$\Delta\phi(l_1 - l_2)$	4.150e-02
6	$\Delta\eta(l_1 - l_2)$	3.327e-02
7	$\Delta\phi(E_T^{miss}, p_{Tb}^{ll})$	2.839e-02
8	E_T^{miss}	2.232e-02
9	$\Delta\phi(j_1 - l_1)$	1.986e-02
10	$\sum_{i=1,2} p_T^{l_i}$	1.680e+00
11	leptonic m_{T2}	1.001e+00

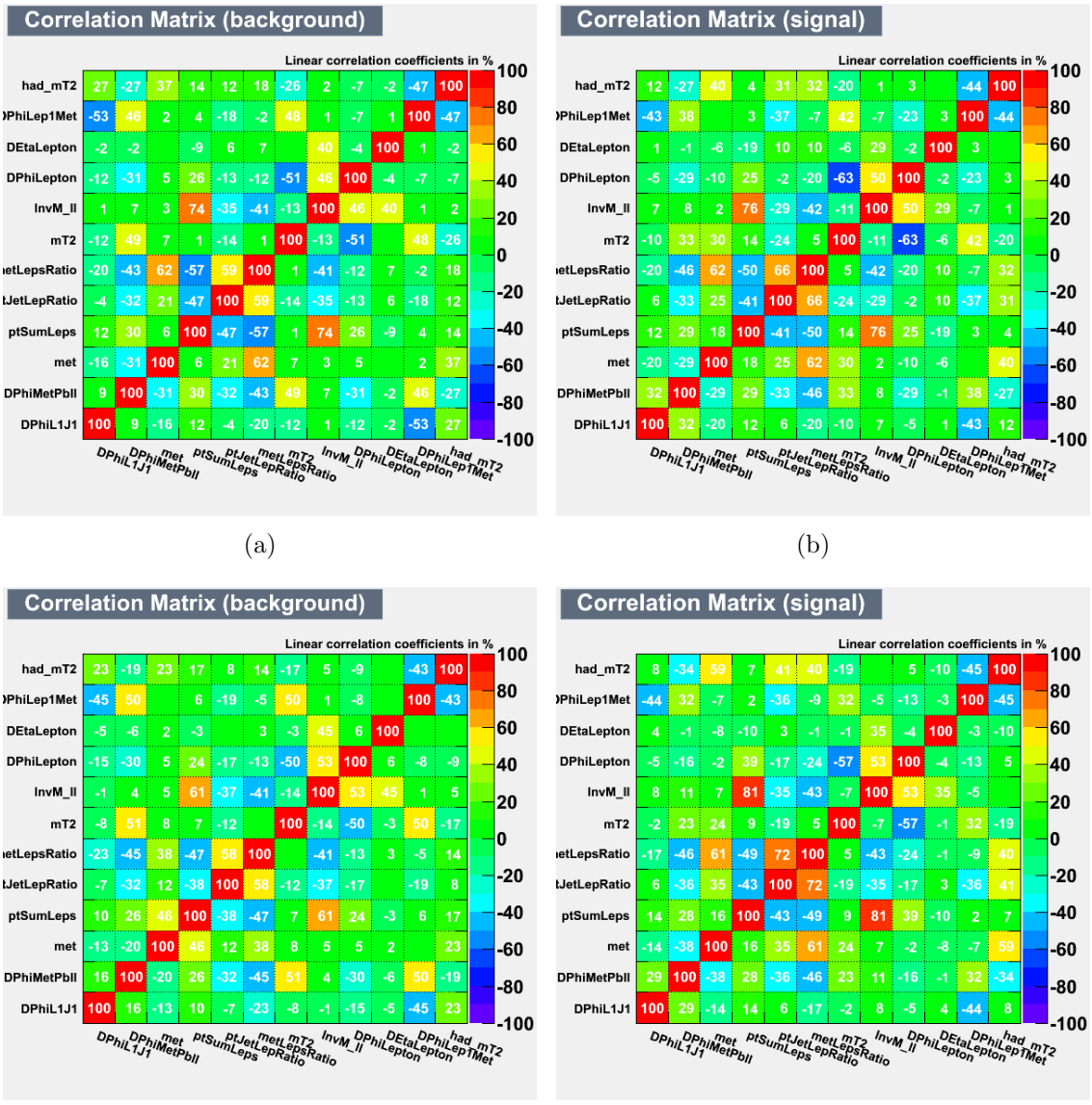

Figure 5.6: Linear correlation coefficients among the different input variables for the training after cuts LC1 for DF (a,b) and SF (c,d). Coefficients for signal are on the left and for background on the right. The plots refer to the signal point with a scalar top mass of 300 GeV and $m(\tilde{\chi}_1^{\pm}, \tilde{\chi}_1^0) = (250,50)$ GeV.

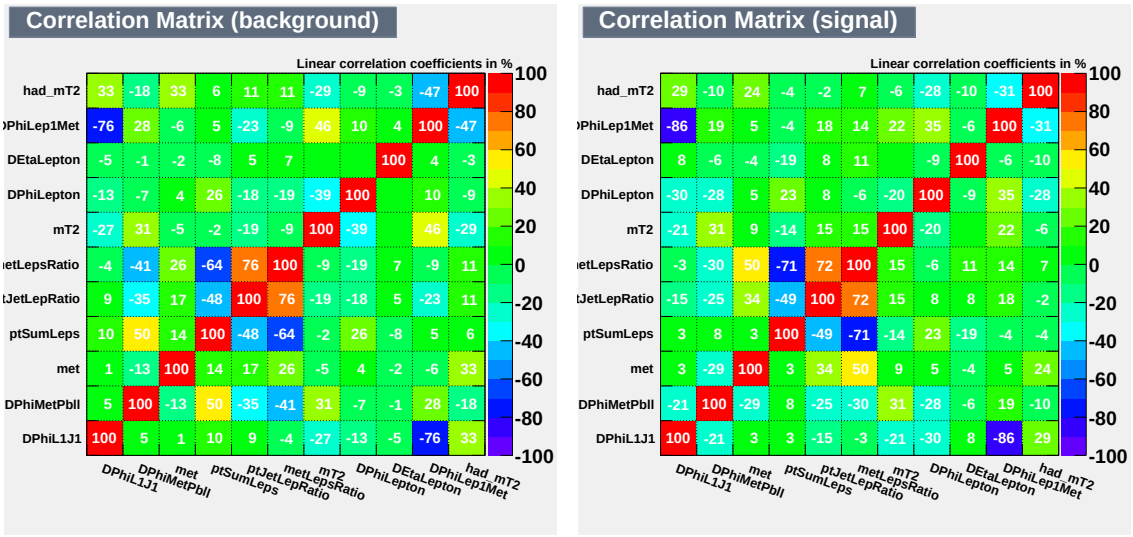

(a) (b)

(c) (d)

Figure 5.7: Linear correlation coefficients among the different input variables for the training after cuts MC1 for DF (a,b) and SF (c,d). Coefficients for signal are on the left and for background on the right. The plots are refer to the signal point with a scalar top mass of 300 GeV and $m(\tilde{\chi}_1^{\pm}, \tilde{\chi}_1^0) = (150,130)$ GeV.

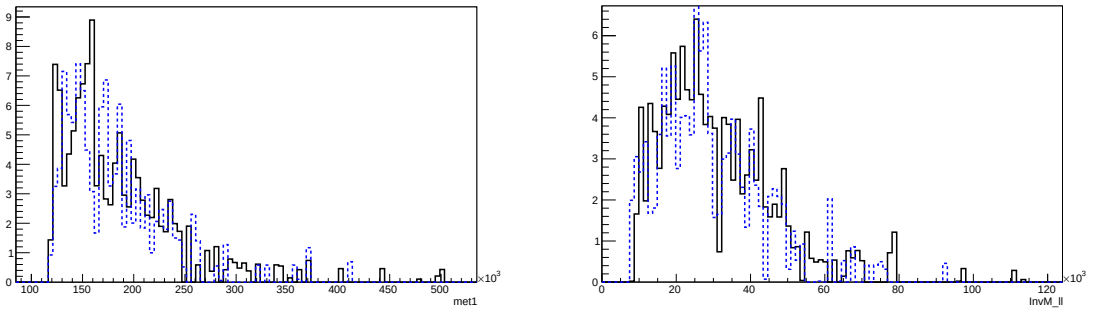

(a)

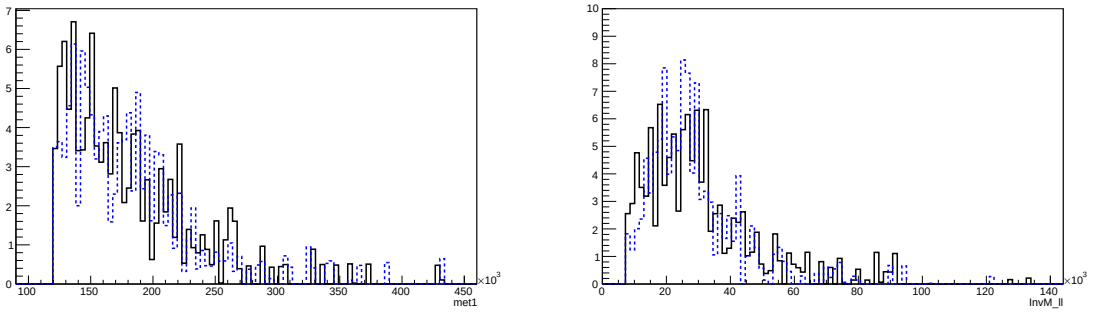

(b)

Figure 5.8: Distributions of some of the input variables (E_{Tmiss}, m_{ll}) after the event selection for DF (a) and SF (b) channels and the reference signal points RPA (full line) and RPB (dashed line) for MET triggered events.

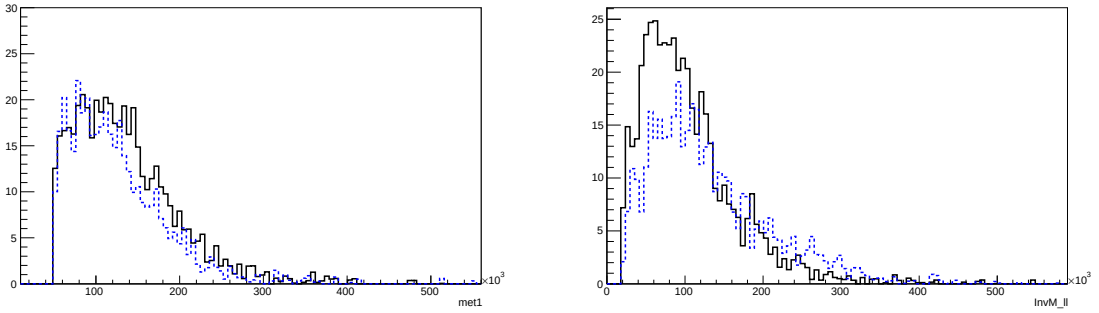

(a)

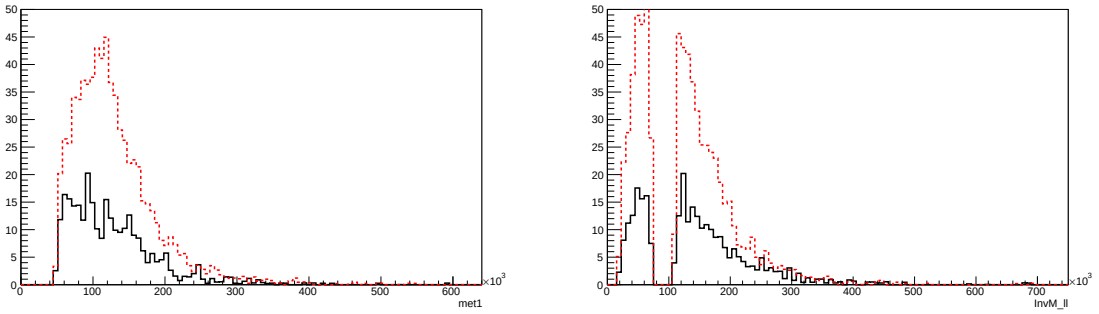

(b)

Figure 5.9: Distributions of some of the input variables (E_T^{miss}, m_{ll}) after the the event selection for DF (a) and SF (b) channels and the reference signal points RPD (full line), RPE (dashed blue line) and RPF (dashed red line) for Lepton triggered events.

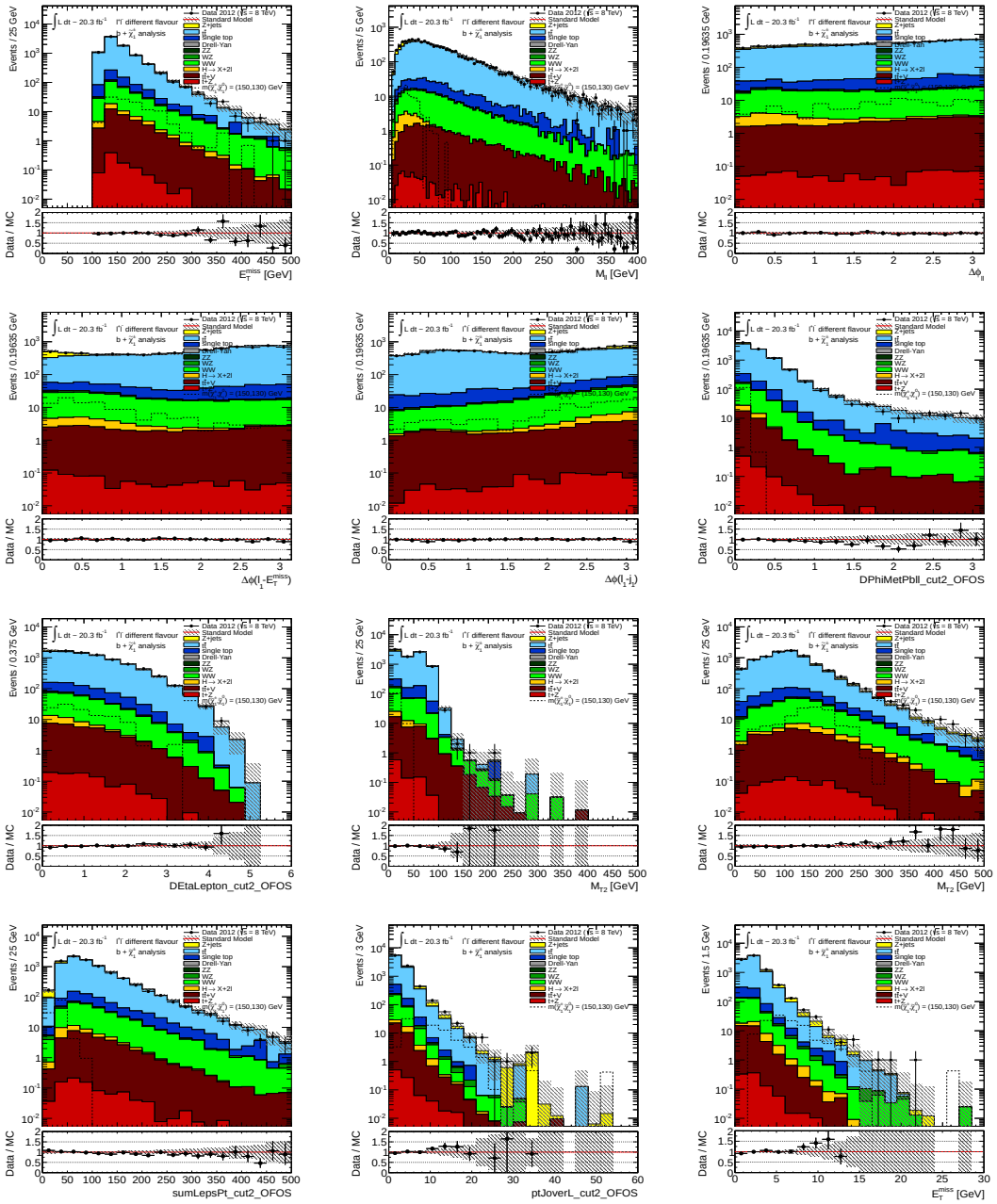

Figure 5.10: Distributions of several variables after cuts MC1 for DF channel in data and in Monte Carlo, among which there are all 11 input variables to the MVA. From top left to bottom right: E_T^{miss}, m_{ll}, $\Delta\phi(l_1 - l_2)$, $\Delta\phi(-l_1)$, $\Delta\phi(j_1 - l_1)$, $\Delta\phi(-p_{Tb}^{ll})$, $\Delta\eta(l_1 - l_2)$, leptonic M_{T2}, hadronic M_{T2}, $\sum_{i=1,2} p_T^{l_i}$, $\sum_{i=1,2} p_T^{j_i} / \sum_{i=1,2} p_T^{l_i}$, $/\sum_{i=1,2} p_T^{l_i}$. For comparison, the distributions for the reference signal point with a scalar top mass of 300 GeV and $m(\tilde{\chi}_1^{\pm}, \tilde{\chi}_1^0) = (150,130)$ GeV are also shown. Only statistical errors are shown.

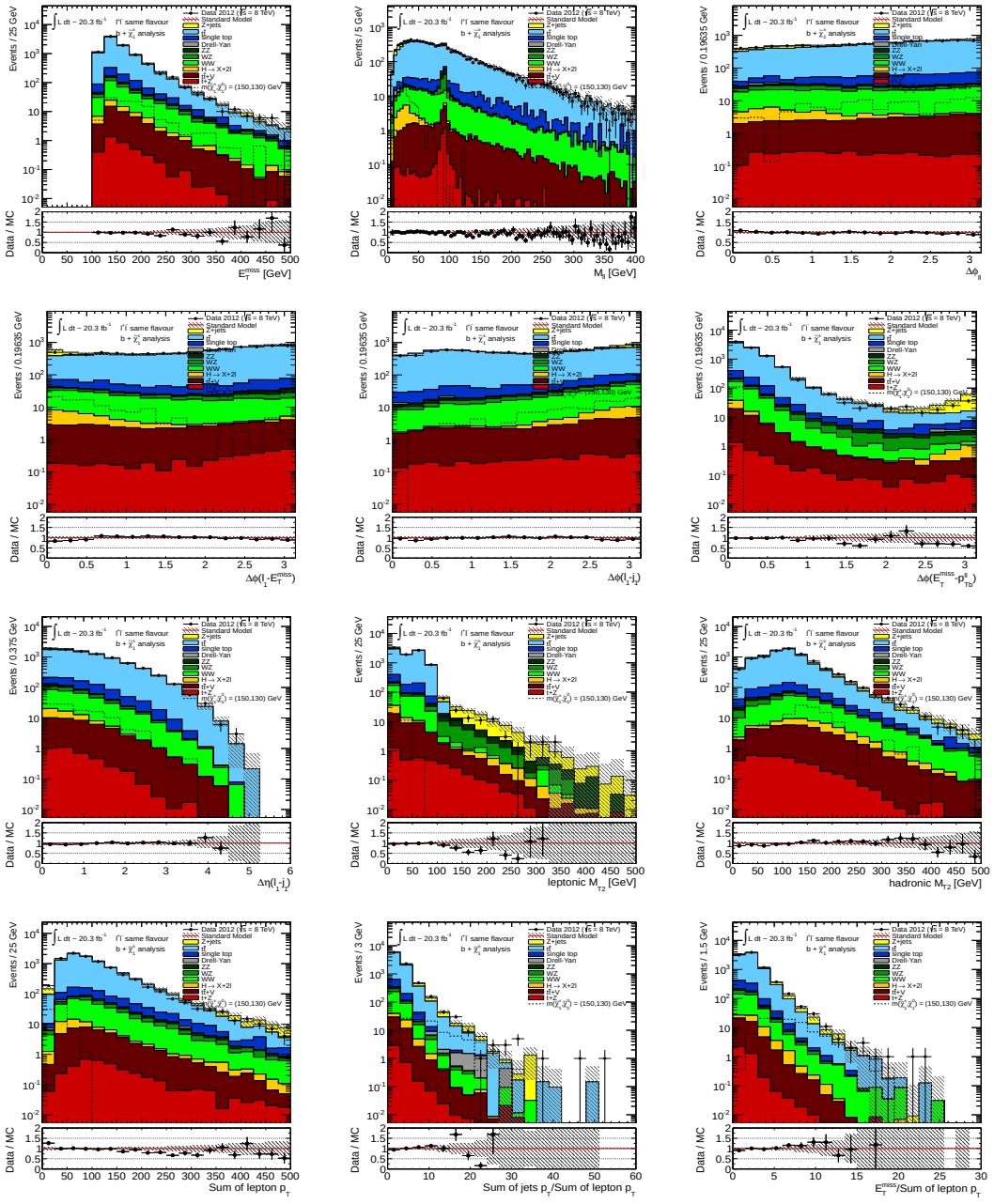

Figure 5.11: Distributions of several variables after cuts MC1 for SF channel in data and in Monte Carlo, among which there are all 11 input variables to the MVA. From top left to bottom right: E_{Tmiss}, m_{ll}, $\Delta\phi(l_1 - l_2)$, $\Delta\phi(-l_1)$, $\Delta\phi(j_1 - l_1)$, $\Delta\phi(-p_{Tb}^{ll})$, $\Delta\eta(l_1 - l_2)$, leptonic M_{T2}, hadronic M_{T2}, $\sum_{i=1,2} p_T^{l_i}$, $\sum_{i=1,2} p_T^{j_i} / \sum_{i=1,2} p_T^{l_i}$, $/\sum_{i=1,2} p_T^{l_i}$. For comparison, the distributions for the reference signal point with a scalar top mass of 300 GeV and $m(\tilde{\chi}_1^{\pm}, \tilde{\chi}_1^0) = (150,130)$ GeV are also shown. Only statistical errors are shown.

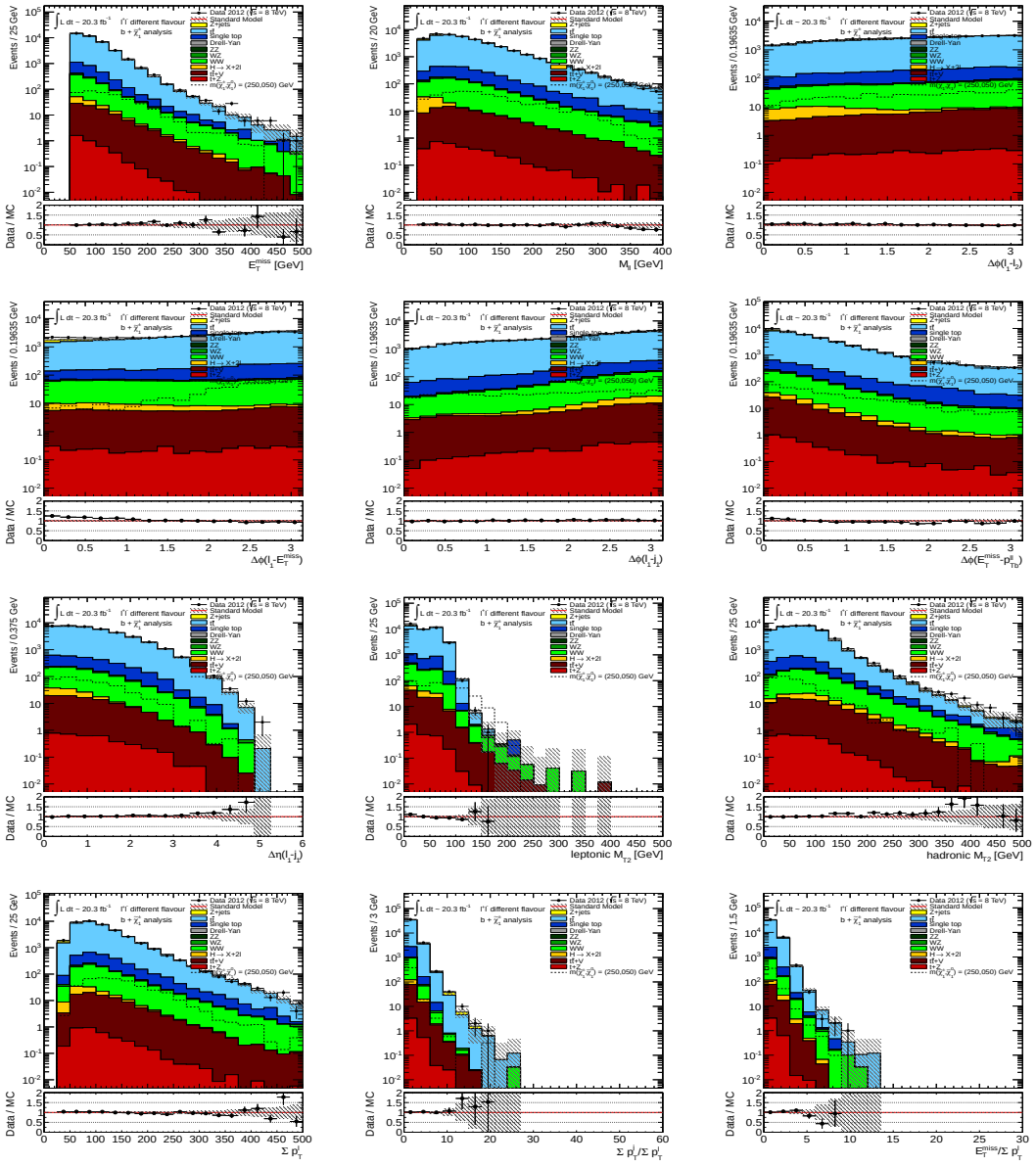

Figure 5.12: Distributions of several variables after cuts LC1 for DF channel in data and in Monte Carlo, all 12 input variables to the MVA. From top left to bottom right: , m_{ll}, $\Delta\phi(l_1-l_2)$, $\Delta\phi(-l_1)$, $\Delta\phi(j_1-l_1)$, $\Delta\phi(-p_{Tb}^{ll})$, $\Delta\eta(l_1-l_2)$, leptonic M_{T2}, hadronic M_{T2}, $\sum_{i=1,2} p_T^{l_i}$, $\sum_{i=1,2} p_T^{j_i}/\sum_{i=1,2} p_T^{l_i}$, $/\sum_{i=1,2} p_T^{l_i}$. For comparison, the distributions for the reference signal point with a scalar top mass of 300 GeV and $m(\tilde{\chi}_1^{\pm}, \tilde{\chi}_1^0) =$ (250,50) GeV are also shown. Only statistical errors are shown.

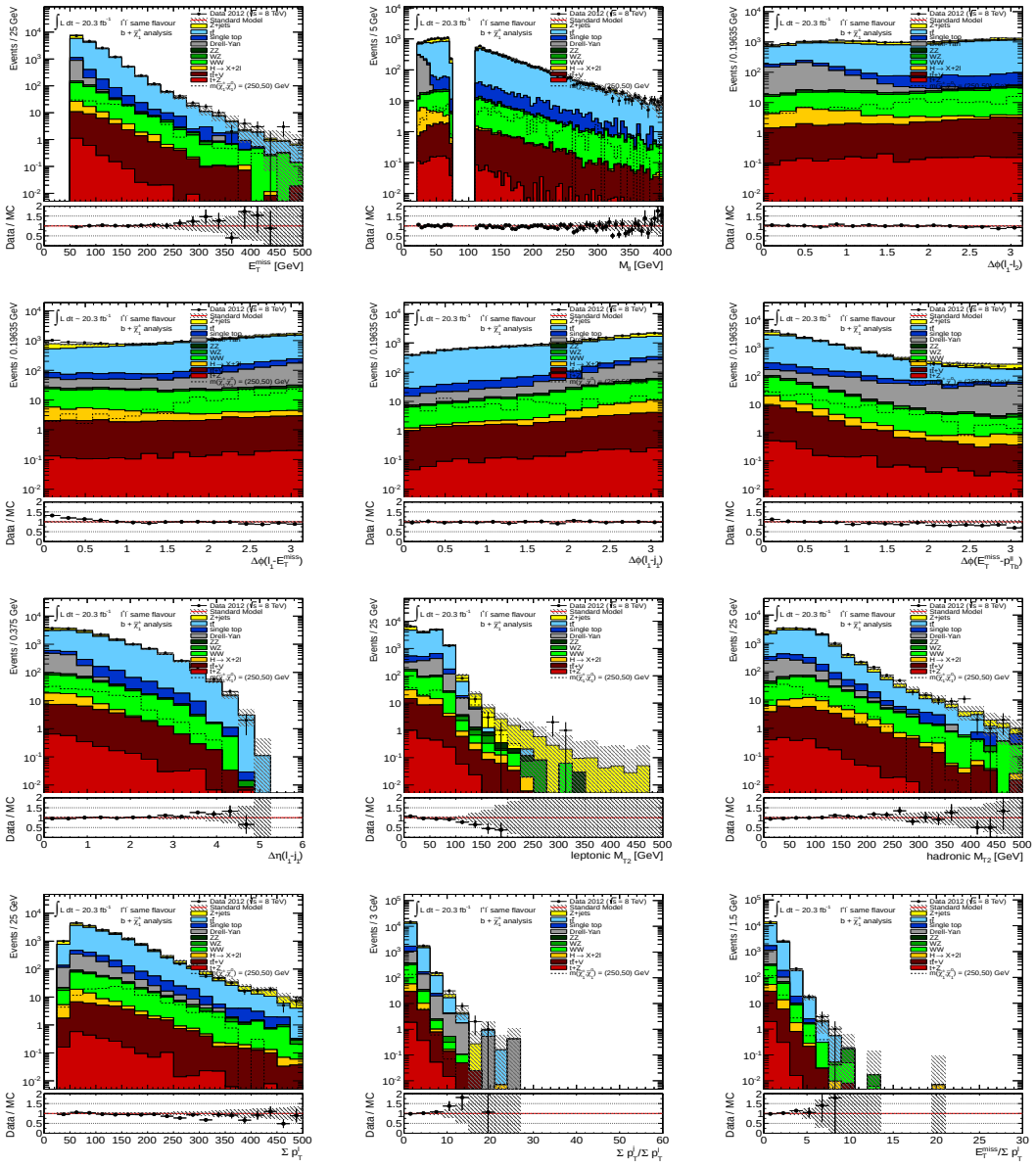

Figure 5.13: Distributions of several variables after cuts LC1 for SF channel in data and in Monte Carlo, all 12 input variables to the MVA. From top left to bottom right: , m_{ll}, $\Delta\phi(l_1-l_2)$, $\Delta\phi(-l_1)$, $\Delta\phi(j_1-l_1)$, $\Delta\phi(-p_{Tb}^{ll})$, $\Delta\eta(l_1-l_2)$, leptonic M_{T2}, hadronic M_{T2}, $\sum_{i=1,2} p_T^{l_i}$, $\sum_{i=1,2} p_T^{j_i}/\sum_{i=1,2} p_T^{l_i}$, $/\sum_{i=1,2} p_T^{l_i}$. For comparison, the distributions for the reference signal point with a scalar top mass of 300 GeV and $m(\tilde{\chi}_1^{\pm}, \tilde{\chi}_1^0) =$ (250,50) GeV are also shown. Only statistical errors are shown.

CHAPTER 6

Sensitivity and Systematics

After learning in the training phase for the different signal reference point and for all the background sources, a set of probabilistic weight is determined. In the subsequent application procedure the BDTG classifier response distributions are produced for each background, for each event sample in the signal grid and for the data. All signal datasets different from the reference ones, and the data, were totally independent on the training. Figure 6.1 shows these distributions for the different background sources for DF and SF channels in case of cuts MC1 and LC2 using the two signal reference points considered above in the trainings. $\tilde{t}t$ is the dominant background in the whole BDTG value range, for both cases, followed by Wt and Z for MET triggered events. Z is the second source of background for Lepton triggered events .

6.1 Signal Region and Expected Sensitivity

To discriminate the signal from the background, signal regions (SR) are selected where the signal is expected to show a distinctive behavior. SR are selected in such a way that they cut away the background, but still leave a significant amount of signal events. Final definition of Signal region is based upon the "significance" for each Reference point. The cut on the BDTG value (t_{cut}) is chosen based on BDTG classifier response distributions for each reference point. By optimizing significance value, the best cuts and the SR is chosen.

The final definition of the SRs in the analysis was done as described in the following:

- The "significance"' for each training point is defines as:

$$\xi = \frac{N_S}{\sqrt{N_S + N_B + (\Delta N_B)^2_{syst}}} \tag{6.1}$$

  where N_S and N_B are the numbers of signal and background events which survived the cut, respectively. It was computed as a function of t_{cut} for each point over the entire signal grid. The term $(\Delta N_B)_{syst}$ takes into account the presence of a systematic uncertainty on background, roughly estimated as 50% of N_B, which is a reasonable assumption.

- The BDTG classifier cut value (t_{cut}) to be applied for each point over the signal grid, for DF and SF channels separately. The t_{cut} value was chosen, which maximized the significance for the relative reference point with the most suitable choice of preliminary cuts.

- for MET triggered events, a relevant background source surviving the BDTG cut is represented by $Z \to \tau\tau$ events, in which τ's produce a soft lepton in the final state. In order to reject them, events falling in SRs are required to have at least one b-tagged jet.

The SRs considered for this analysis are listed in table 6.1. Finally, for DF and SF separately, for each point over the signal grid, the SR with the highest significance was chosen for the calculation of the limits.

The index of the best SR chosen on significance basis for each point of the grid is reported in figure 6.2 and in figure 6.3 respectively for MET triggered and Lepton triggered events, in case of DF and SF channels, together with the corresponding expected signal yields and significances. It is important to specify that in the final

Table 6.1: Signal regions considered for this analysis

Signal Region	Reference Point	Preselection cuts	t_{cut}	b-jets
SR_1^{DF}	RPA	MC1	-0.49	≥ 1
SR_2^{DF}	RPB	MC1	-0.39	≥ 1
SR_3^{DF}	RPC	MC1	-0.57	≥ 1
SR_4^{DF}	RPD	LC1	-0.38	-
SR_5^{DF}	RPE	LC1	0.36	-
SR_6^{DF}	RPG	LC2	0.20	-
SR_1^{SF}	RPA	MC1	-0.53	≥ 1
SR_2^{SF}	RPB	MC1	-0.53	≥ 1
SR_3^{SF}	RPC	MC1	-0.45	≥ 1
SR_4^{SF}	RPE	LC1	-0.25	-
SR_5^{SF}	RPF	LC2	-0.09	-

limit setting procedure the HistFitter package was allowed to perform independently the choice of the best SR for each signal point on the basis of the lowest computed CLs_{exp} value. The expected background rates in the SRs for DF and SF channels are reported in table 6.2 and 6.3, respectively. When no event is observed, an upper limit can be estimated at 95% C.L. assuming Poisson probabilities. Based on expected background rates in the SRs, following observations can be made:

- The $t\tilde{t}$ and $t\tilde{t}$+boson(s) dominate in almost all SRs.
- The Z+jets contribution is strongly suppressed by the cut on BDTG value and it is more relevant for SF channels.
- For MET triggered events, the Z+jets contribution is suppressed by b-jet requirement.
- The diboson contribution is present in several signal regions for both DF and SF channels.

In figure 6.4 and 6.5 BDTG, E_T^{miss}, M_{T2} and m_{ll} distributions are shown for data and Monte Carlo events in SR_4^{DF} and SR_2^{SF} respectively.

Table 6.2: Expected number of background events in the DF signal regions for $20.1fb^{-1}$ for MET triggered events and $20.3fb^{-1}$ for Lepton triggered events. Only the Monte Carlo statistical errors are reported here.

Process	SR_1^{DF}	SR_2^{DF}	SR_3^{DF}	SR_4^{DF}	SR_5^{DF}	SR_6^{DF}
$t\tilde{t}$	4.56 ± 0.86	2.63 ± 0.57	1.51 ± 0.46	2.84 ±0.62	4.28 ± 0.74	0.76 ± 0.25
$t\tilde{t}W$, $t\tilde{t}Z$, $t\tilde{t}WW$	0.13 ± 0.03	0.07 ± 0.02	0.04 ± 0.02	0.39 ± 0.05	0.68 ± 0.07	0.42 ± 0.06
$Z + jets, DY$	0.29 ± 0.09	0.10 ± 0.05	0.08 ± 0.02	0.02 ± 0.01	0.01 ± 0.01	-
Wt, Zt	0.37 ± 0.37	-	0.02 ±0.02	0.11 ± 0.11	0.41 ±0.37	0.42 ± 0.37
WW, WZ, ZZ	-	-	-	1.00 ± 0.18	2.16 ± 0.27	1.46 ± 0.23
H	0.01 ± 0.01	-	-	-	-	-
total SM	5.37 ± 0.94	2.81 ± 0.57	1.65±0.46	4.35 ± 0.66	7.54 ± 0.87	3.07 ± 0.51

Table 6.3: Expected number of background events in the SF signal regions for $20.1fb^{-1}$ for MET triggered events and $20.3fb^{-1}$ for Lepton triggered events. Only the Monte Carlo statistical errors are reported here.

Process	SR_1^{SF}	SR_2^{SF}	SR_3^{SF}	SR_4^{SF}	SR_5^{SF}
$t\tilde{t}$	8.87 ± 1.04	7.20 ± 0.97	2.98 ± 0.62	2.95 ± 0.61	3.84 ± 0.70
$t\tilde{t}W$, $t\tilde{t}Z$, $t\tilde{t}WW$	0.19 ± 0.04	0.23 ± 0.04	0.12 ± 0.03	0.32 ± 0.05	0.33 ± 0.05
$Z + jets, DY$	0.77 ± 0.24	0.72 ± 0.25	0.72 ± 0.24	0.11 ± 0.05	0.33 ± 0.25
Wt, Zt	-	0.10 ± 0.08	-	0.09 ± 0.08	0.35 ± 0.34
WW, WZ, ZZ	0.09± 0.06	0.08± 0.05	0.01 ± 0.01	2.49 ± 0.31	0.56 ± 0.13
H	-	-	-	0.03 ± 0.02	-
total SM	9.92 ± 1.07	8.34± 1.01	3.85±0.67	6.00 ± 0.68	5.42 ± 0.83

6.2 Systematics

The prediction of all background expectations are subject to various systematic uncertainties. These systematic uncertainties can impact the expected event yields

in the control and signal regions as well as the extrapolation from the CRs to the SRs. It is crucial that these uncertainties are taken into account when interpreting an analysis. The systematic uncertainties can be grouped in two categories: experimental uncertainties, which pertain to detector-based sources of uncertainty, or object calibration; and theoretical uncertainties, which include the uncertainties associated with the cross-sections, PDFs and the luminosity, are few of them. This section describes the impact on the analysis of several sources of systematic uncertainties, which are handled following the latest combined performance group recommendations. In addition to them, also the statistical error coming from the limited MC statistics has to be considered.

Most part of systematics are estimated by comparing the results of the final analysis obtained with the nominal background and signal samples to the ones obtained with the systematically varied background and signal samples. We coherently used in the application phase the same training for the nominal and the systematically varied samples.

6.2.1 Experimental uncertainties

- Jet Energy Scale (JES): This uncertainty is asymmetric and associated with the jet energy scale calibration of jets to the hadronic scale. The JES calibration offers a correction to the calorimeter-measured energy, scaling it to better represent the energy of the particles in the jet.It is evaluated as a function of jet p_{T} and η by using the `MultijetJESUncertaintyProvider` implemented in the package `JetUncertainties-00-08-06` and then comparing the results obtained with the nominal jet energy scale corrections and the ones obtained using jets whose p_{T} and energy were scaled taking into account the JES uncertainty.

- Jet Energy Resolution (JER): A variation in the resolution of the jet energies can lead to migrations between bins in the jet multiplicity distribution and result in events passing or failing the control and signal region selections. This systematics implemented in the package `JetResolution -02-00-02`, following the recommendations of the JetEtMiss group.
- Pile-up: The scale factors to weight Monte Carlo events in order to take into account the harsh pile-up conditions at the LHC introduce another systematic uncertainty. This uncertainty is evaluated comparing the nominal results with those obtained by doing the pileup reweighing without the 10% rescaling. The resulting systematic uncertainty is symmetrized.
- Jet vertex fraction (JVF): Using tracking and vertexing information, a discriminant called Jet vertex fraction is defined which described the probability that a jet originated from a particular vertex. Since a cut on this discriminant is applied, a systematic uncertainty is introduced. A JVF cut to jets with $p_T < 50$ GeV and $|\eta| < 2.4$. Using the JVFUncertaintyTool, the uncertainty associated with the use of this cut is estimated, as implemented in `JVFUncertainty-00-00-04`.
- CellOut: The systematic uncertainty on the `CellOut` component of E_T^{miss}, which includes the energy scale of clusters not associated to objects and the effect of pileup, is evaluated using the code provided by the Jet/EtMiss group in `MissingETUtility-01-02-04`. Two parameters are associated with the E_T^{miss} cell-out uncertainty. One considers variations in the cell-out energy scale and the other variations in the cell-out energy resolutions. The uncertainties related to the energy scale and the energy resolution of unassociated clusters are evaluated separately and added in quadrature.

6.2.2 Theoretical uncertainties

- Generators and process modeling: An additional important systematic uncertainty for this analysis is the MC generator uncertainty. The generator uncertainty is estimated comparing different samples obtained with different generators. It is calculated as $\sigma_{TOT} = \sqrt{\sigma^2_{SYST} + \sigma^2_{STAT}}$, where σ_{SYST} is the differences of the number of events observed in the two generators and σ_{STAT} is the statistical uncertainty of the alternative generator only.

  For Z+jets the baseline SHERPA is compared with the ALPGEN sample. For dibosons (WW, ZZ and WZ), POWHEG is the baseline generator and SHERPA is used to compute systematics. A dedicated description of the theoretical uncertainties on $t\tilde{t}$, the dominant background, is described in the next paragraph.

- $t\tilde{t}$ theoretical uncertainties: For $t\tilde{t}$ the baseline is MC@NLO, and for generator systematics, Powheg+Jimmy sample is considered. The difference between Powheg+Pythia and Powheg+Jimmy is used to assess the uncertainty related to the description of the parton shower. Finally, the uncertainty related to the initial state radiation (ISR) and final state radiation (FSR) in $t\tilde{t}$ events is evaluated considering two different AcerMC samples with different settings and taking half of the difference between these samples as systematic uncertainty.

- Cross Section: The uncertainty related to the cross-section value is taken to be 5% for Z+jets [95]. For $t\tilde{t}$, we use the value of $\sigma_{t\tilde{t}} = 253^{+13}_{-15}$ pb at 8 TeV center of mass energy and for a top quark mass of $172.5/c^2$. For single top $\sigma = 22.4 \pm 1.5$ pb is used for the Wt channel at 8 TeV center of mass energy. The cross-section uncertainties for WW, ZZ and WZ are 6%, 5% and 7% respectively [96] [97]. For $t\tilde{t} + W$ and $t\tilde{t} + Z$ cross section values of 0.23± 0.07 pb and 0.21± 0.06 pb are used, respectively. The uncertainty for $t\tilde{t}$ production cross section do not play any role in the background estimate because this process is normalized

to data in appropriate control regions. The uncertainty on Z, dibosons, single top, $t\tilde{t}+W$ and $t\tilde{t}+Z$ cross sections contribute to the background uncertainty in the SR.

- Luminosity: An uncertainty is assigned to the integrated luminosity of a dataset. The luminosity is determined from the counting rates measured by the ATLAS luminosity detectors. The uncertainty on the luminosity [98] estimated for the whole dataset used in the analysis is 2.8% It is derived, following the same methodology as that detailed in [99], from a preliminary calibration of the luminosity scale derived from beam-separation scans performed in November 2012.

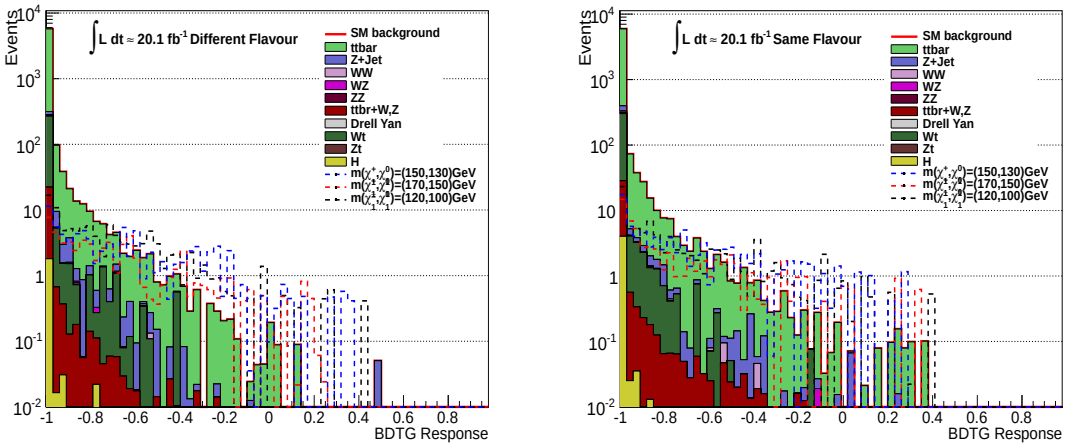

(a) (b)

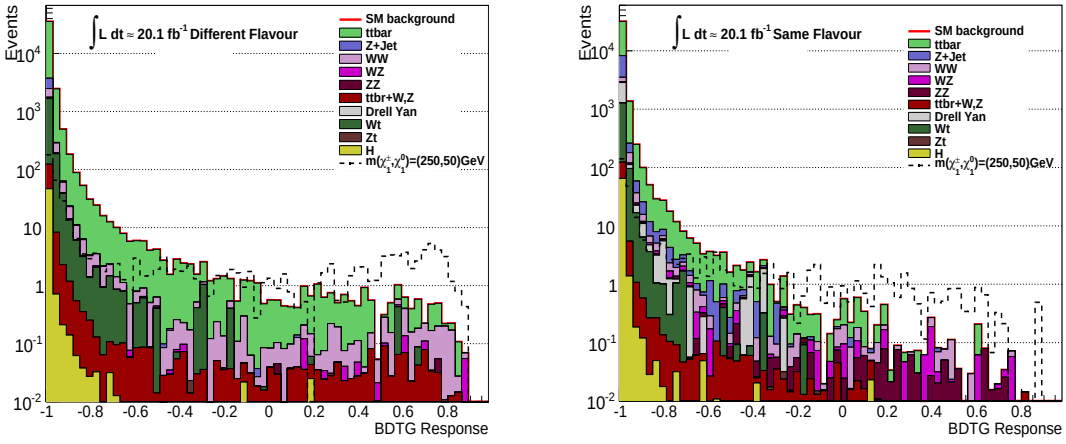

(c) (d)

Figure 6.1: BDTG classifier response distributions for different background processes after cuts MC1 for DF (a) and SF (b) channels and LC2 for for DF (c) and SF (d) channels using the signal reference point with a scalar top mass of 300 GeV and $m(\tilde{\chi}_1^{\pm}, \tilde{\chi}_1^0) = (150,130)$ GeV (top) and the signal reference point with a scalar top mass of 300 GeV and $m(\tilde{\chi}_1^{\pm}, \tilde{\chi}_1^0) = (250,50)$ GeV (bottom) in the trainings. BDTG response for several signal points is represented by the dashed histograms in the plots.

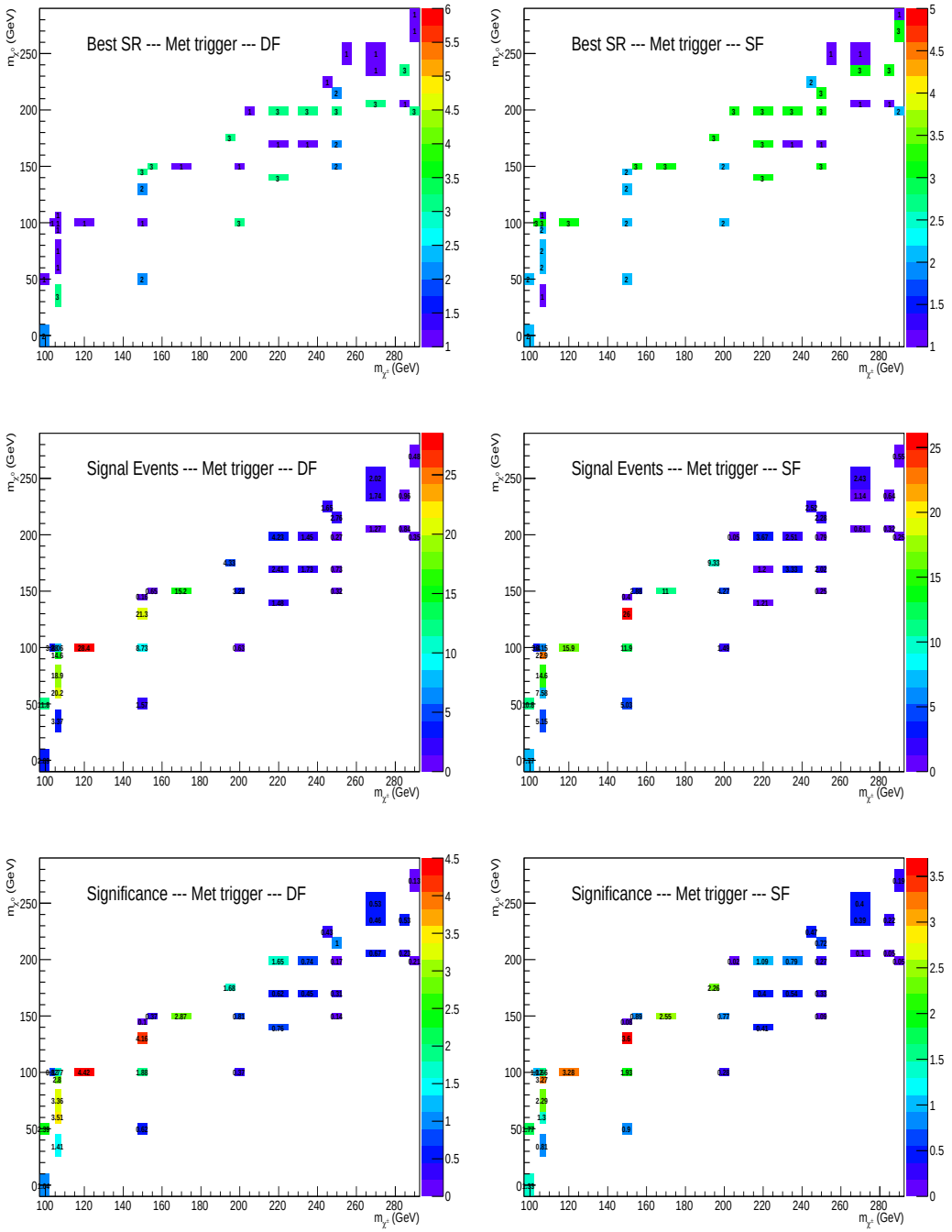

Figure 6.2: MET triggered events. Plots on top: index of the best (chosen on the significance basis) SR among the ones defined in table 6.1 for each point of the signal grid, for DF (left) and SF (right). Plots in the middle: expected number of signal events in the best signal region, for DF (left) and SF (right). Plots on bottom: significance in the best signal region, for DF (left) and SF (right).

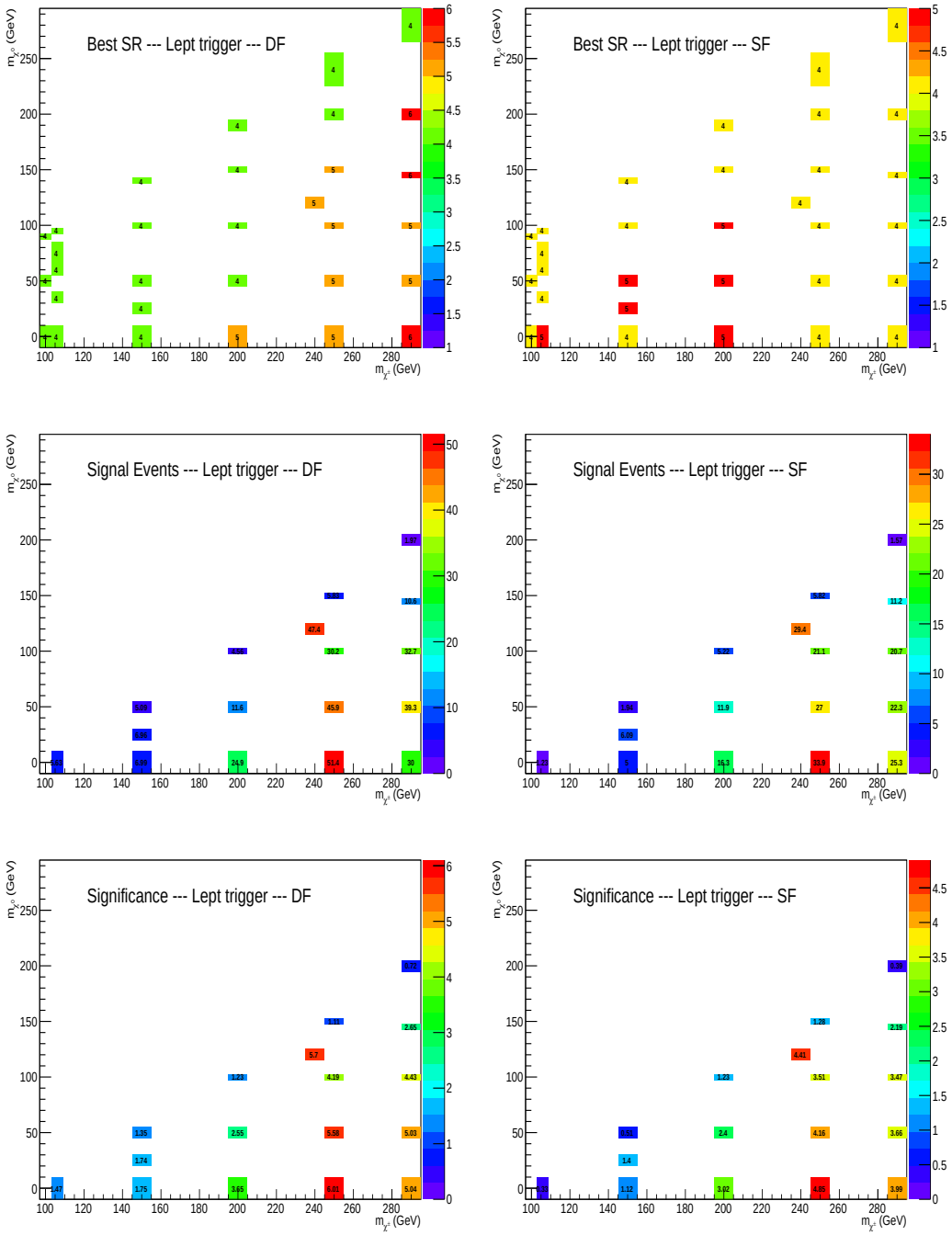

Figure 6.3: Lepton triggered events. Plots on top: index of the best (chosen on the significance basis) SR among the ones defined in table 6.1 for each point of the signal grid, for DF (left) and SF (right). Plots in the middle: expected number of signal events in the best signal region, for DF (left) and SF (right). Plots on bottom: significance in the best signal region, for DF (left) and SF (right).

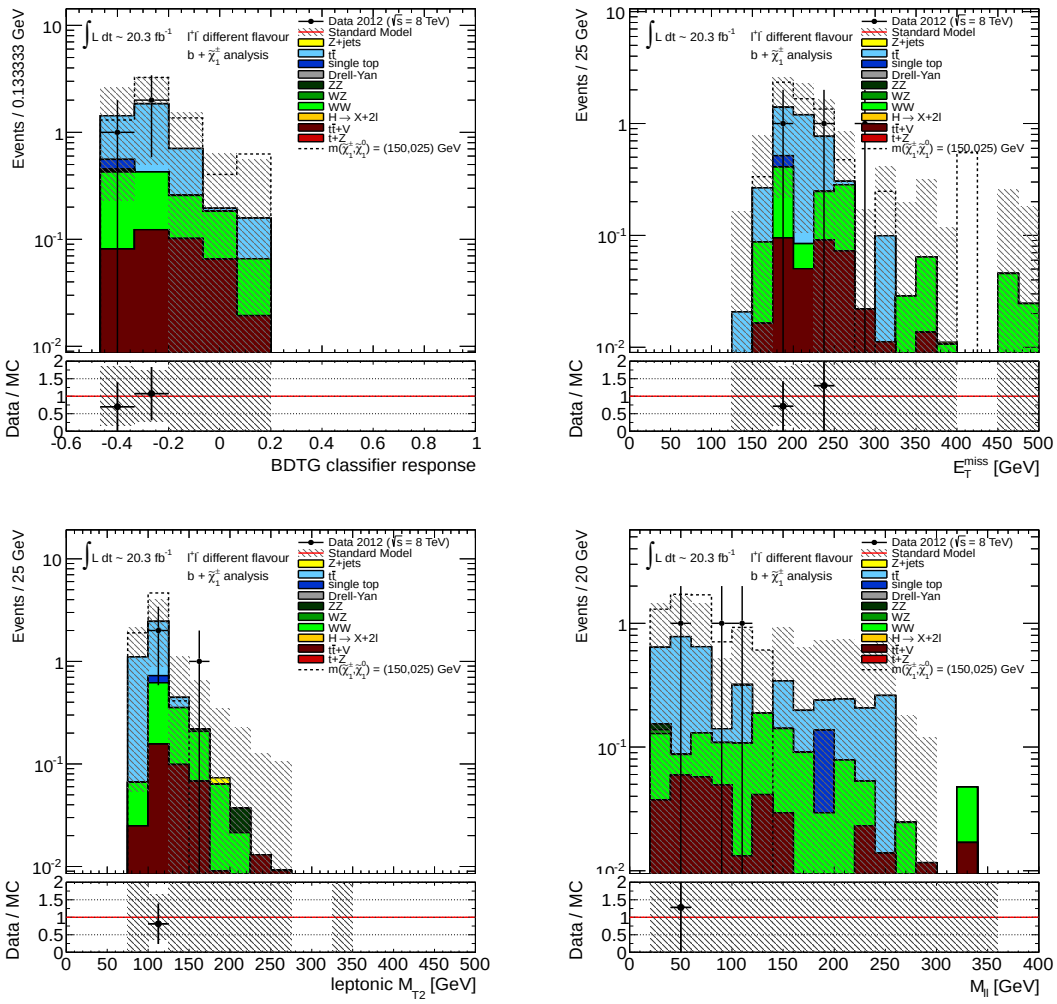

Figure 6.4: BDTG, E_T^{miss}, M_{T2} and m_{ll} distributions of data and Monte Carlo for events in SR_4^{DF}

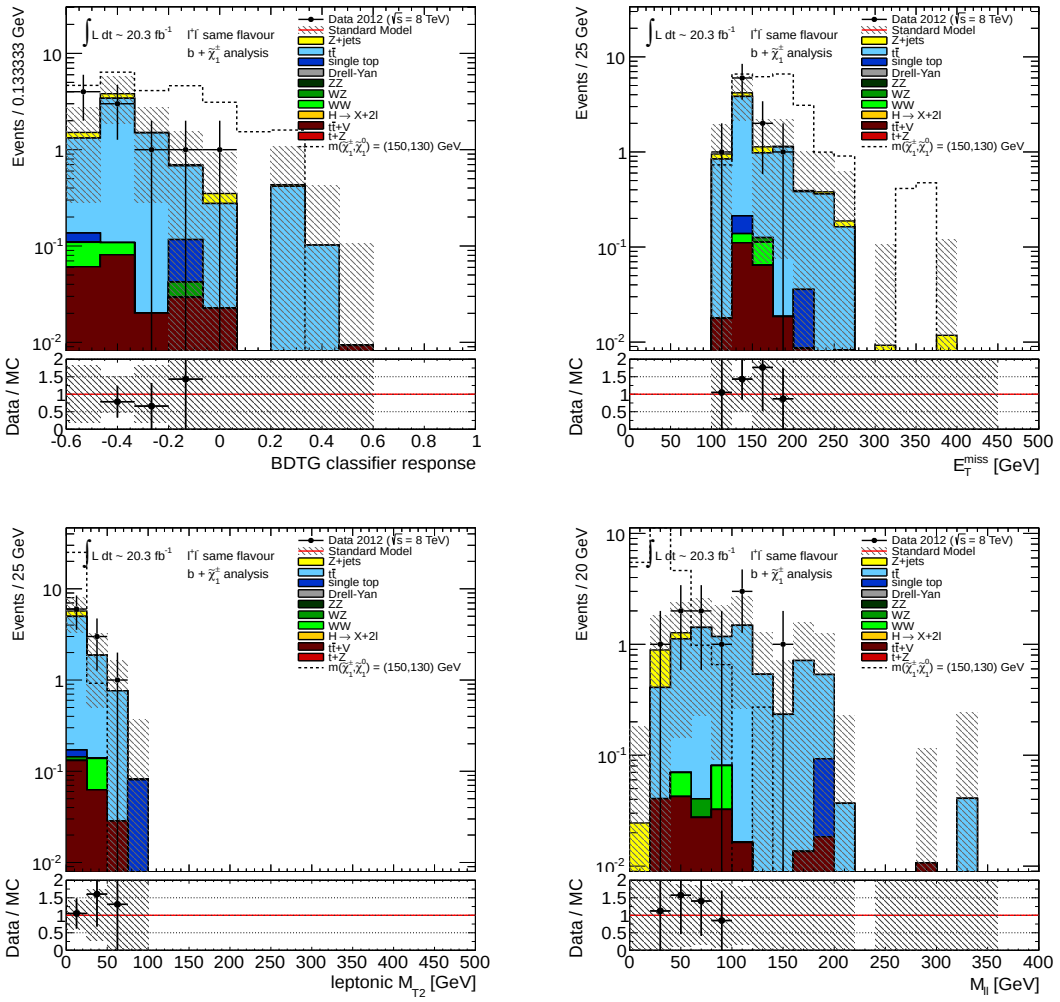

Figure 6.5: BDTG, E_T^{miss}, M_{T2} and m_{ll} distributions of data and Monte Carlo for events in SR_2^{SF}

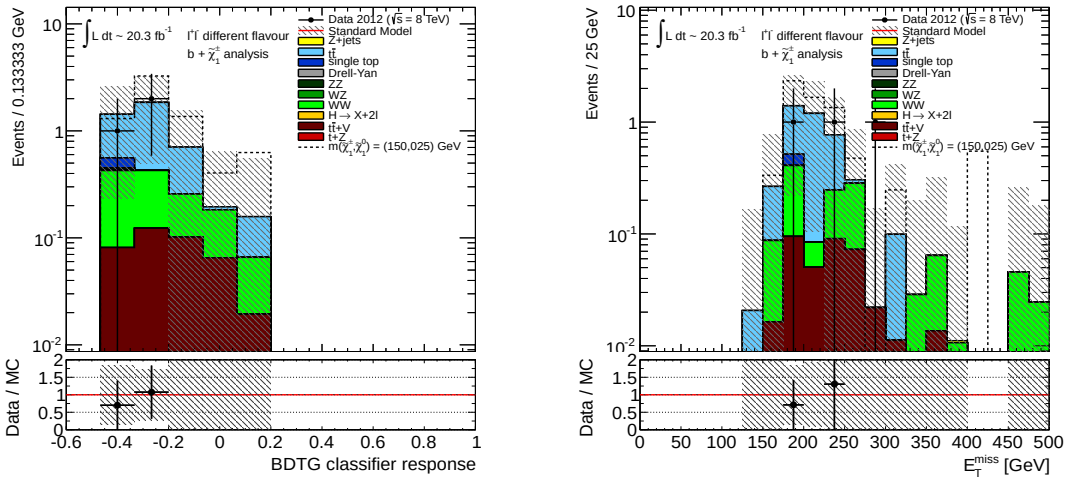

(a) (b)

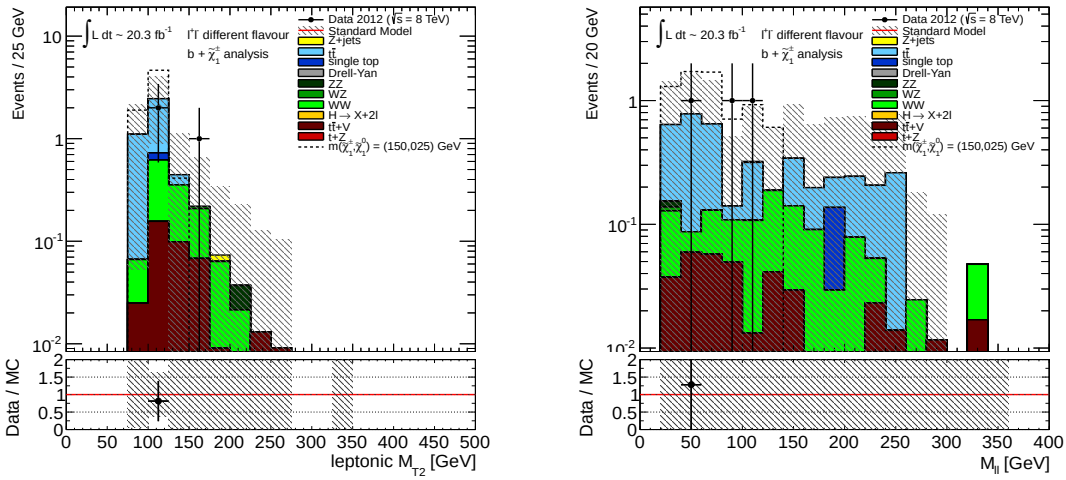

(c) (d)

Figure 6.6: BDTG, E_T^{miss}, M_{T2} and m_{ll} distributions of data and Monte Carlo for events in SR_4^{DF}

CHAPTER 7

Background Estimation

Estimation of the SM backgrounds based only on MC simulations lead to significant systematic uncertainties due to generator modelling, imperfections in simulations and statistical effects. Therefore, in order to estimate the background contributions to the signal regions, a data driven approach is taken. MC predictions of dominant backgrounds are normalized in control regions (CR). Several CRs are designed to be similar in kinematics, but orthogonal to the SRs and enhanced in the particular background of interest. The resulting MC prediction is then used to extrapolate the background components from these CRs to the SRs. CRs are defined to be enriched with the specific background processes they are designed to constrain. These CRs are also used to provide a constraint on the systematic uncertainties on the background estimation in the signal region.

The extrapolation from CR to SR is cross-checked by comparing the estimated background to data in predefined validation regions (VRs). Each VR has a similar definition to that of the control and signal regions, but contains a statistically independent sample of events. It is also important that each VR is dominated by events produced by the background associated to the estimate it is designed to test. By extrapolating that background estimate from the CR to the VR the validity of the extrapolation method is substantiated.

7.1 $t\tilde{t}$ background

The $t\tilde{t}$ background is expected to be the dominant SM background contribution to the SRs. The normalization of this background is determined by using the number of observed events in a CR, in which the amount of expected signal events is negligibly small. For each SR, one CR is defined, which is populated mostly by $t\tilde{t}$ background. Low cross-section background sources (WW, WZ, ZZ, Wt, Z+jets, Drell-Yan, $t\tilde{t}$ W and $t\tilde{t}$ Z, $t\tilde{t}$ WW, H) are estimated through MC simulations. The backgrounds with fake leptons are determined with a data-driven (DD) technique. The number of observed events in data in a given control region is related to the background yield by the equation

$$N^{obs} = \mu_T N_T^{MC}(CR) + N_{others}^{MC}(CR) + N_{fakes}^{DD}(CR) \tag{7.1}$$

where $N_T^{MC}(CR)$ is the yield predicted by MC in the CR for $t\tilde{t}$, μ_T is the scale (or normalization) factor to be applied to this MC background in order to fit the data, $N_{others}^{MC}(CR)$ is the MC yield for the sum of the other processes and $N_{fakes}^{DD}(CR)$ is the number of events with fake leptons, determined from data. After determining the scale factor, μ_T, from equation 7.1, the expected background in the SR is :

$$N_{bkg}(SR) = \mu_T N_T^{MC}(SR) + N_{others}^{MC}(SR) + N_{fakes}^{DD}(SR). \tag{7.2}$$

By applying this method, the normalization of $t\tilde{t}$ events in the different CRs and the corresponding SRs is derived from the data. The systematic uncertainties affects this normalization in the various regions and are taken into account to determine the uncertainty on the final background prediction.

The $t\tilde{t}$ background estimate is performed with the HistFitter package [100], a wrapper for the RooFit framework [101] and a high-level user-interface to perform

binned likelihood fits and evaluate their statistical interpretation. The package uses HistFactory, RooStats and RooFit. HistFitter allows for a correct treatment of systematics, taking properly into account their correlations. For each CR a likelihood fit is performed with the observed rate in the CR as constraint and the μ_T term as free parameter. The systematics uncertainties are described by nuisance parameters and each nuisance parameter is described by a gaussian centered on zero and of width one. Zero corresponds to the nominal rate in all regions, while ± 1 correspond to the " and " systematic variations. Systematic uncertainties which are one-sided are symmetrized. Different nuisance parameters are treated as uncorrelated.

$t\tilde{t}$ control regions are defined for all the channels as described below, taking into account the different BDTG distributions, both in shapes and in BDTG range extension, of $t\tilde{t}$ events and of the other background sources for the different reference points.

7.1.1 Control Region Definition

The choice of CRs is driven by the following motivations:

- To enhance the top background thus reaching a high top purity in the region (up to $\sim 94\%$ for DF and $\sim 93\%$ for SF in case of MET triggered events, and up to $\sim 87\%$ for DF and $\sim 83\%$ for SF in case of Lepton triggered events);
- To choose a region reasonably far from the SR to reduce the signal contamination to few percent level, but close enough to reduce the contributions of the systematic uncertainties;
- To select $t\tilde{t}$ events as much as possible similar to the ones which populate the SRs in order to extrapolate the normalization factor μ_T from each CR to the corresponding SR.

The CRs for DF and SF channel (MET triggered events and Lepton triggered events) are populated by events passing all cuts in the analysis, shown in table 7.1 and 7.2, respectively.

Table 7.1: Control regions considered for the DF channel

Control Region (CR)	BDTG values
CR_1^{DF}	within the region [-1.00,-0.90]
CR_2^{DF}	within the region [-1.00,-0.90]
CR_3^{DF}	within the region [-1.00,-0.90]
CR_4^{DF}	within the region [-0.96,-0.90]
CR_5^{DF}	within the region [-0.90,-0.80]
CR_6^{DF}	within the region [-0.95,-0.90]

Table 7.2: Control regions considered for SF channel.

Control Region (CR)	BDTG values
CR_1^{SF}	within the region [-1.00,-0.90]
CR_2^{SF}	within the region [-1.00,-0.90]
CR_3^{SF}	within the region [-1.00,-0.90]
CR_4^{SF}	within the region [-0.98,-0.90]
CR_5^{SF}	within the region [-0.98,-0.90]

In figure 7.1 and figure 7.2, different distributions (BDTG, E_T^{miss}, M_{T2} and m_{ll}) are shown for data and MC events in CR_1^{DF} and CR_1^{SF} respectively, while in figure 7.3 and figure 7.4 the same distributions are shown for data and MC events in CR_5^{DF} and CR_4^{SF} respectively.

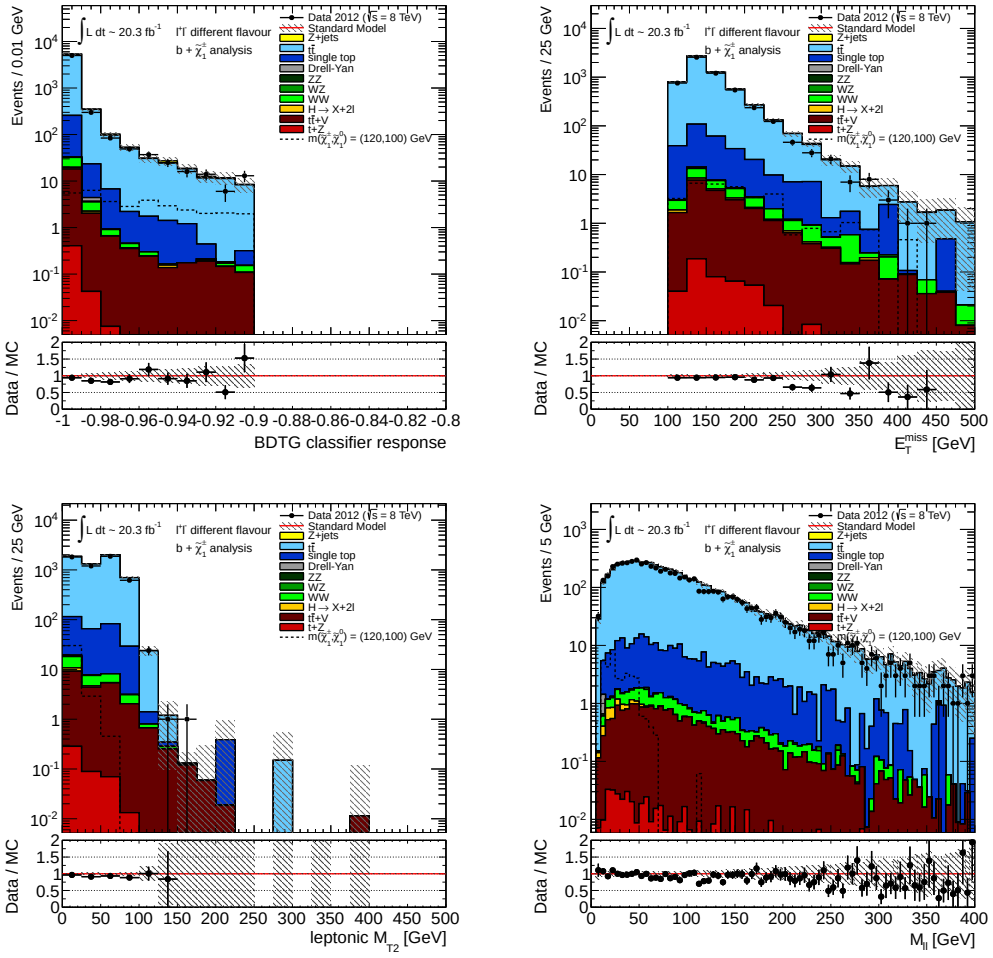

Figure 7.1: BDTG, E_T^{miss}, M_{T2} and m_{ll} distributions of data and Monte Carlo for events in CR_1^{DF}

The signal contamination in CRs is estimated to range from few % for many points of the signal grid up to $\sim$ 7% in CR_5^{DF}. In table 7.3 all contamination are estimated for all the reference signal points. When deriving limits with HistFitter, the signal contamination is properly taken into account in the profile likelihood fit.

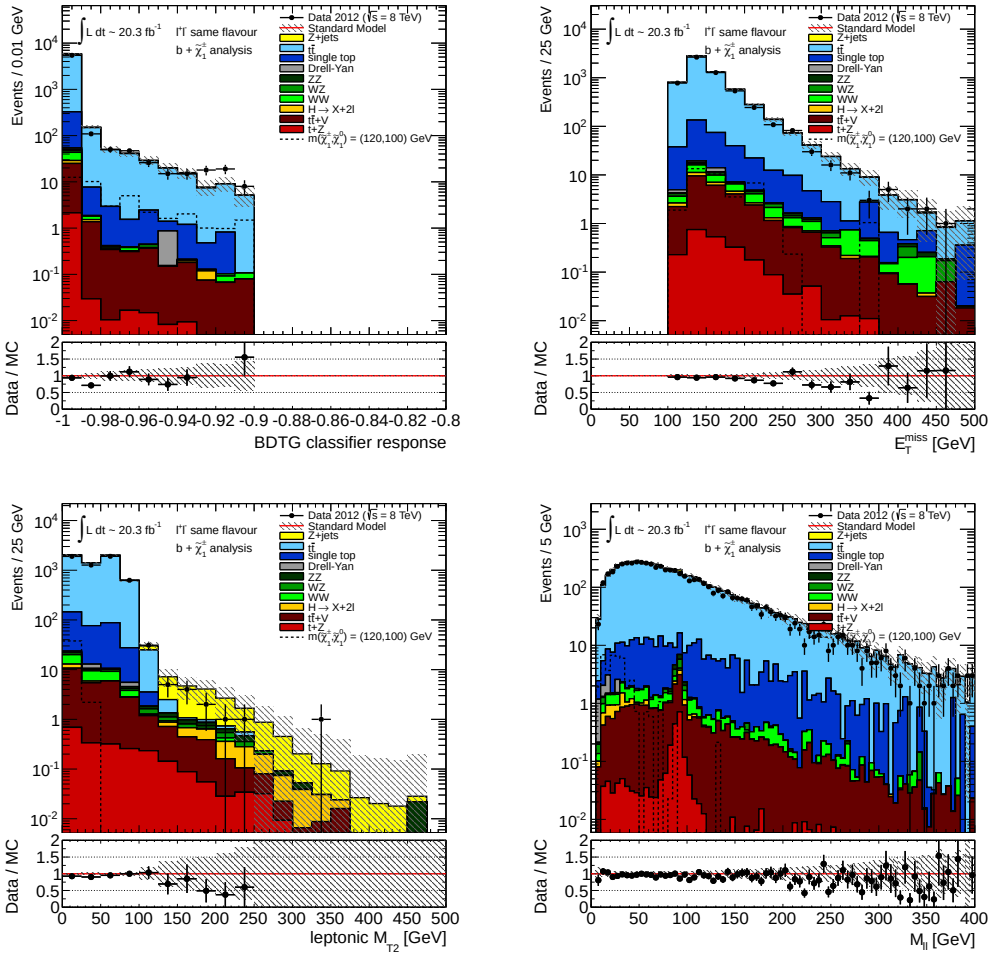

Figure 7.2: BDTG, E_T^{miss}, M_{T2} and m_{ll} distributions of data and Monte Carlo for events in CR_1^{SF}

7.1.2 Validation Region Definition

A dedicated VR for each SR has been introduced, in order to cross-check the agreement between the predicted background and the observed rate. To get the VR, a different BDTG range is chosen with the same preliminary cuts, but separate from the corresponding SR and CR. In order to preserve statistics in each VR it is kept close to the corresponding SR. VRs corresponding to each SR are listed in table 7.4 and 7.5.

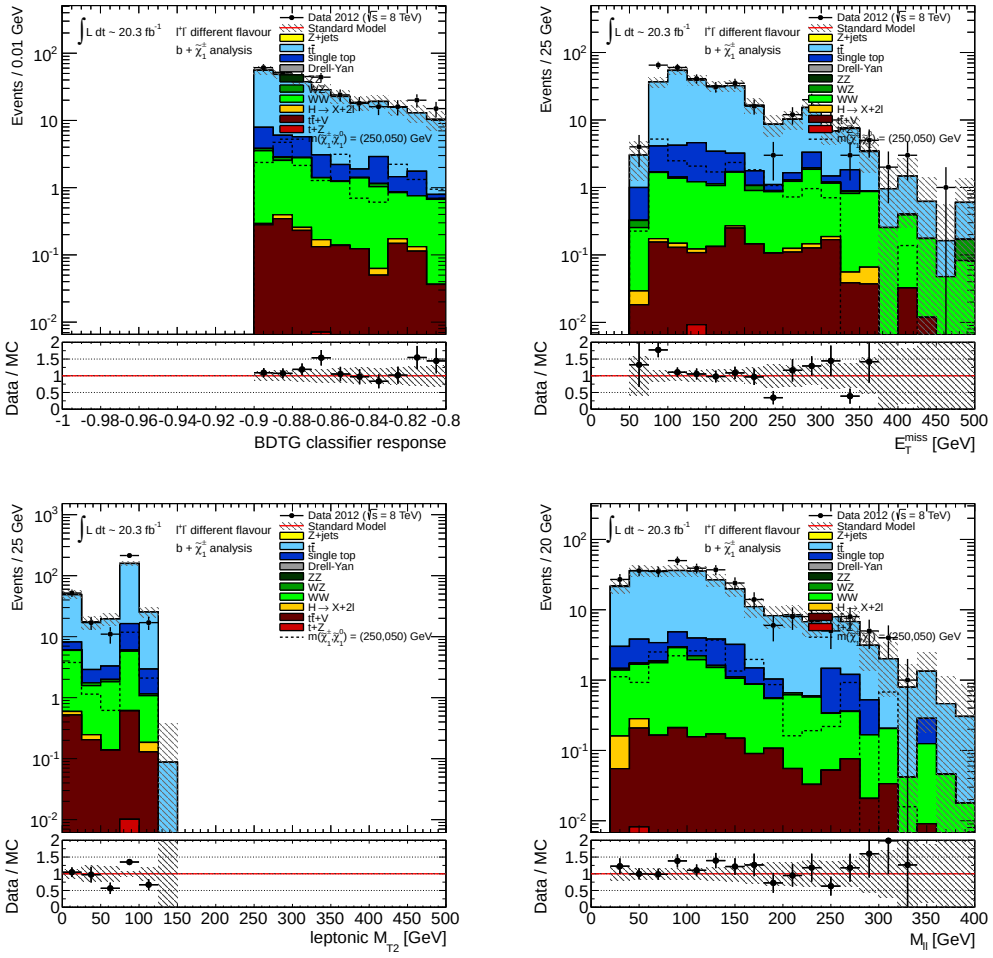

Figure 7.3: BDTG, E_T^{miss}, M_{T2} and m_{ll} distributions of data and Monte Carlo for events in CR_5^{DF}

7.2 Z+jets Background

The background from Z+jets and DY was considered only in case of same flavour leptons, since in the different flavour cases it was found negligible in all SRs. This background was estimated from Monte Carlo, in fact it is strongly suppressed by the Z veto cut in case of lepton triggered events and from the b-tag request in case of MET triggered events, leading to contributions in SRs always lower than ∼10%, except in SR_3^{SF}. The Z+jets rates in the different SRs and $t\tilde{t}$ CRs are discussed in

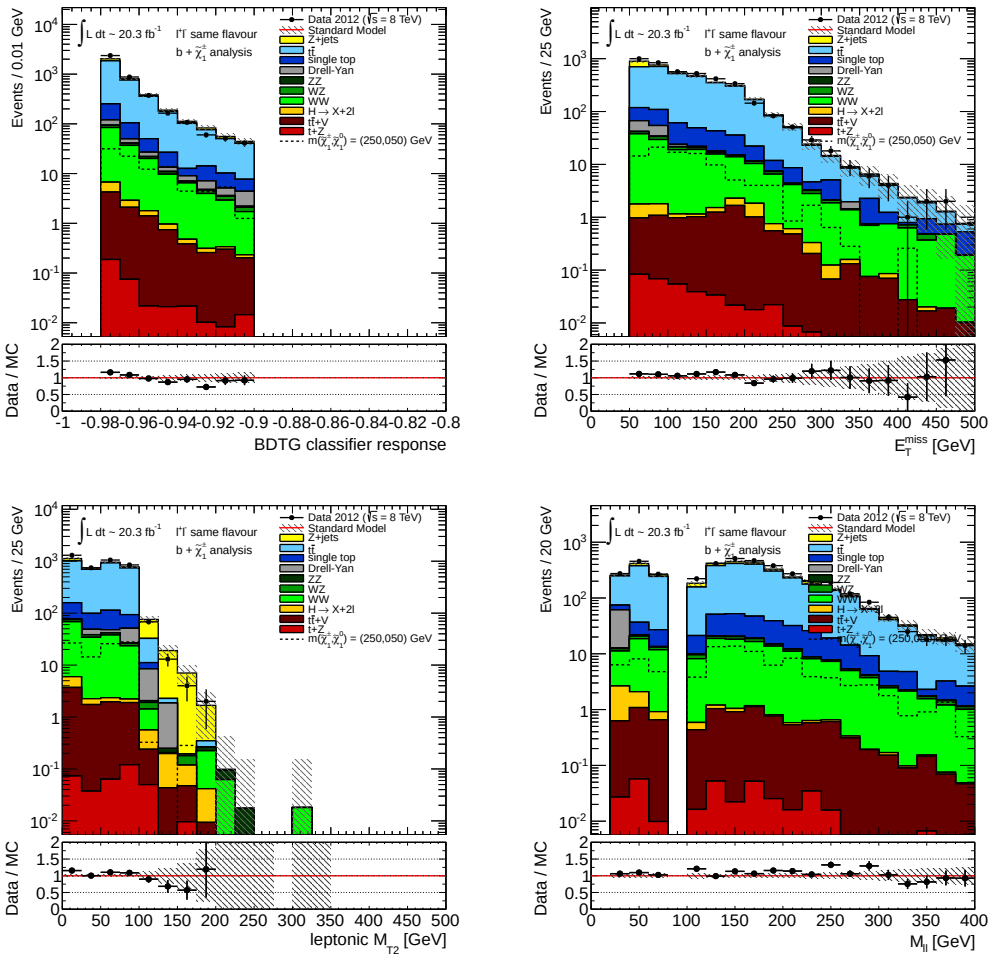

Figure 7.4: BDTG, E_T^{miss}, M_{T2} and m_{ll} distributions of data and Monte Carlo for events in CR_4^{SF}

the next chapter. Systematics include the cross section and luminosity uncertainties, JES, JER, the E_T^{miss} cellout term systematics, the pileup, the MC statistics and the contribution coming from the MC generator predictions, obtained by comparing the SHERPA baseline generator with ALPGEN.

Table 7.3: Signal contamination in CRs as obtained from MC. The corresponding reference signal points are considered for each estimate.

	CR_1^{DF}	CR_2^{DF}	CR_3^{DF}	CR_4^{DF}	CR_5^{DF}	CR_6^{DF}	CR_7^{DF}
Contamination	31.0%	20.5%	29.1%	19.0%	2.7%	2.4%	1.5%

	CR_1^{SF}	CR_2^{SF}	CR_3^{SF}	CR_4^{SF}
Contamination	23.8%	24.3%	10.1%	4.8%

Table 7.4: Validation regions considered for the DF channel

Validation Region (VR)	BDTG values
CR_1^{DF}	within the region [-0.90,-0.49]
CR_2^{DF}	within the region [-0.90,-0.39]
CR_3^{DF}	within the region [-0.90,-0.57]
CR_4^{DF}	within the region [-0.90,-0.38]
CR_5^{DF}	within the region [-0.90,-0.36]
CR_6^{DF}	within the region [-0.90,-0.20]

7.3 Diboson Backgrounds

The most relevant diboson backgrounds in the signal regions, in case of Lepton triggered events, is WW for DF , while for SF, WZ and ZZ are also present. The diboson rates are estimated by means of MC, taking advantage of the excellent agreement between data and MC in the latest diboson cross-section measurements from ATLAS [102] [103].

The expected final rates in the different signal and $t\tilde{t}$ CRs as obtained from POWHEG, together with the corresponding systematic errors. These errors include the theoretical and the experimental uncertainties. The contribution coming from the MC generator predictions are estimated by comparing the baseline POWHEG generator and SHERPA samples. For SHERPA, which is a leading order generator,

Table 7.5: Validation region considered for SF channel.

Validation Region (VR)	BDTG values
CR_1^{SF}	within the region [-0.90,-0.53]
CR_2^{SF}	within the region [-0.90,-0.53]
CR_3^{SF}	within the region [-0.90,-0.45]
CR_4^{SF}	within the region [-0.90,-0.25]
CR_5^{SF}	within the region [-0.90,-0.09]

the total cross-section is normalized to the reference cross- sections calculated with MCFM. For POWHEG, which is a NLO generator, the cross-sections as calculated by the generator itself are used.

In order to compare the shapes, the high tails of the BDTG value distributions of WW are shown in figure 7.5, for DF and SF channels after cut LC2 in case of RPG and RPF points, respectively. The distributions of the two generators show a good agreement, which concludes the simulation consistency of the kinematics of the WW system.

A similar comparison is done for WZ and ZZ in figure 7.6 for SF channels in case of RPD and RPB points after cuts LC1 and LC2 respectively. The comparison of different generators is not easy for these two processes, as it is influenced by the mass interval taken in each generator and by the prescriptions for the simulation of the interference structure of the $Z/\gamma^{\star}$ system. The results show a good agreement between the WZ distributions. In case of ZZ, the distributions are normalized to the same integral, and the shapes show a reasonable agreement between them.

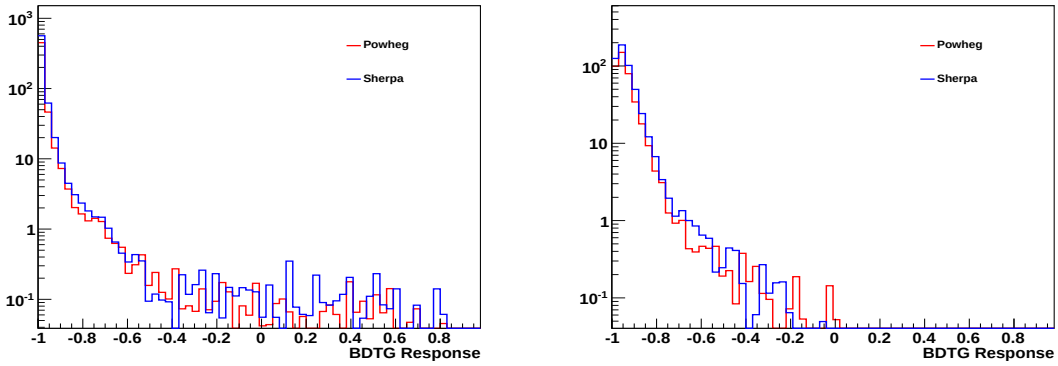

(a) (b)

Figure 7.5: BDTG classifier response distributions of WW with two different MC generators: SHERPA (blue line) and POWHEG (red line) for DF channel for RPG (a) and for SF channel for RPF (b) after cuts LC2

7.4 Single Top, $t\tilde{t}$+X and Higgs Backgrounds

For processes whose small cross sections make it difficult to select control samples in the data, the background estimate has to be based on the MC simulation. Single Top, $t\tilde{t}$+X and Higgs backgrounds are estimated by means of MC. For the single top, only the Wt process was considered, while the s-channel and t-channel contributions enters in the data driven estimate of processes with at least one fake or non isolated lepton. For Zt all contributions (Wt process, s-channel and t-channel) were considered. For $t\tilde{t}W$ and $t\tilde{t}Z$ the leading order MADGRAPH samples are used, and the different Higgs production processes and decays with two leptons in the final state are simulated with POWHEG. The expected rates in the different signal and $t\tilde{t}$ CRs for DF and SF are provided in next section together with the corresponding systematic errors.

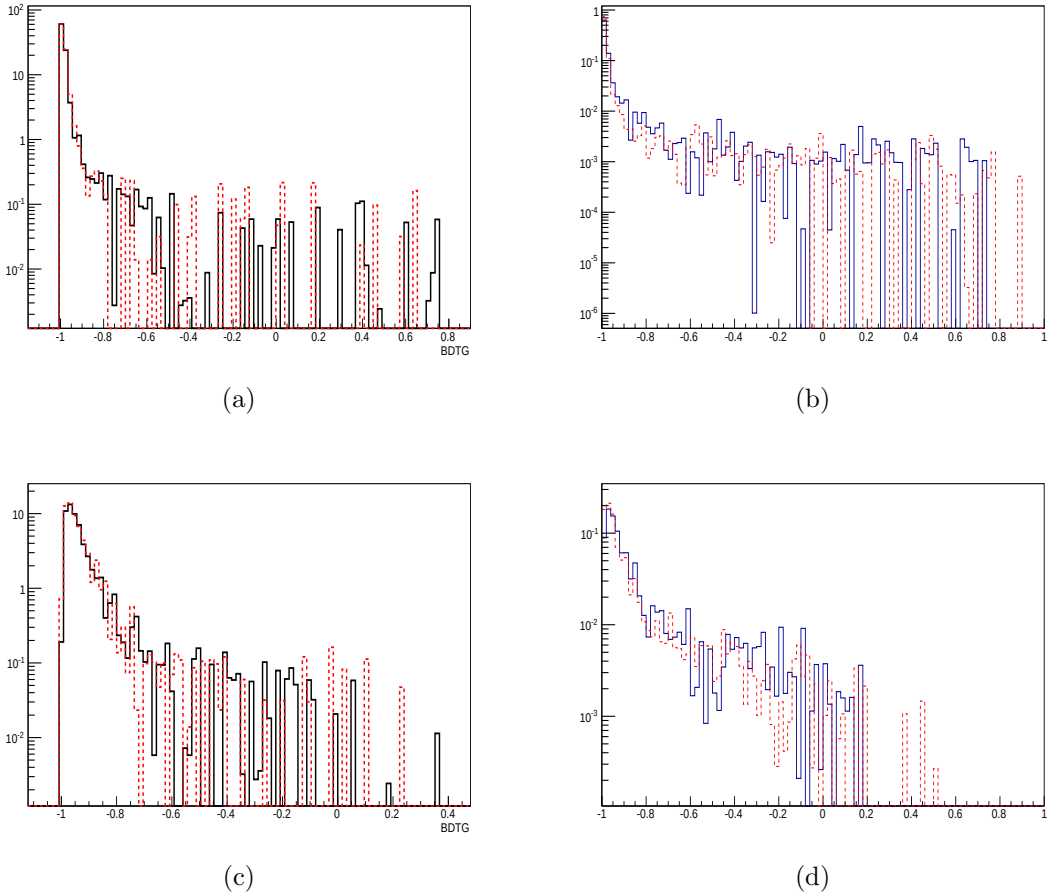

(a) (b)

(c) (d)

Figure 7.6: BDTG classifier response distributions of WZ (left) and ZZ (right) in SF channels with two different MC generators: SHERPA (black and blue lines) and POWHEG (red lines) after cuts (LC1) for RPE (top) and RPF (bottom).

7.5 Fake Lepton Background Estimation

In addition to backgrounds with two real leptons, there is also a background contribution from processes that have fewer than two real leptons and one or more fake leptons. This occurs when jets are incorrectly interpreted as leptons after the physics object cuts. Similarly jets that punch through into the muon system could potentially fake muons, though muon fakes more commonly originate from pions or kaons decaying in-fight as they traverse the detector, or otherwise from heavy flavour

decays. Such muons are usually poorly isolated, but can sometimes still pass the signal muon isolation requirements. The sources of fake leptons in dilepton events are QCD multijet events, such as $b\bar{b}$(+jets), $c\bar{c}$(+jets) etc, where two jets fake leptons, or from real-fake sources such as $t\tilde{t}$ and W/Z+jets, where one lepton is prompt and the other one is a misreconstructed jet. The background contribution arising from fake leptons is estimated using data-driven matrix method [104].

7.5.1 Matrix Method

The matrix method is used to estimated the reducible background, ie.background where at least one lepton is non-prompt or not genuinely isolated, as opposed to real leptons. This method works by dividing the dataset into two categories based on "loose" and "tight" lepton definition, which are then used to define selection efficiencies of real and fake leptons (electrons and muons), which in turn are used to calculate a probability for an event to have one or more fake leptons (depending on the number of leptons in the final state). The tight leptons pass all the standard electron/muon object selection criteria, while the loose leptons differ from the tight ones by looser isolation/selection criteria, where both, tight and loose, are analysis dependent.

The matrix method is described here in its simplest form where the estimation of the fake lepton contribution in a single lepton sample is undertaken, However, the methods can readily be generalized for estimation of the the fake lepton contribution with any number of leptons.

In case of one lepton final state we can define the number of leptons, which pass the loose selection, as $N^l = N^l_r + N^l_f$, where N^l_r and N^l_f are the number of real and fake leptons, respectively, passing the loose selection criteria. The same kind of relation holds also for tight leptons, namely $N^t = N^t_r + N^t_f$, where N^t_r and N^t_f are the number of real and fake leptons, respectively, passing the tight selection criteria.

The method relies on determination of the real and fake efficiencies, ϵ_{real} and ϵ_{fake}, from dedicated control samples. More specifically, the efficiencies for real or fake loose leptons to also satisfy the tight criteria is defined as

$$\epsilon_r = \frac{N_r^t}{N_r^l} \quad \text{and} \quad \epsilon_f = \frac{N_f^t}{N_f^l} \tag{7.3}$$

where the real and fake efficiencies, ϵ_r and ϵ_f, are the probabilities that a real or a fake loose lepton will pass also the tight criteria. The real lepton efficiency ϵ_{real} is measured using a CR consisting of events with a Z boson decaying to two leptons. The fake lepton efficiency ϵ_{fake} is measured from CRs, where the contribution of fake leptons is significantly higher. In these terms the number of tight leptons can be expressed as $N^t = \epsilon_r N_r^l + \epsilon_f N_f^l$.

Knowing the values of ϵ_r and ϵ_f and also counting N^l and N^t, we can solve the above equations to yield the fraction of fake leptons as

$$N_f^t = \frac{\epsilon_f}{\epsilon_r - \epsilon_f}(\epsilon_r N^l - N^t). \tag{7.4}$$

To apply this formula to each single data event i passing the loose or tight selection, it can be generalized as a weight w_i to apply to an event defined like,

$$w_i = \frac{\epsilon_f}{\epsilon_r - \epsilon_f}(\epsilon_r - \delta_i), \tag{7.5}$$

where δ_i is equal to 1, if the event i passes the tight lepton selection, and 0 otherwise. The weights w_i are built in such a way that the sum over all the data events gives N_f^t, i.e. $\sum w_i = N_f^t$.

From above relations one is able to obtain the following relations in the single lepton case.

$$N^l = (1-\epsilon_r)N_r^l + (1-\epsilon_f)N_f^l \tag{7.6}$$

$$N^t = \epsilon_r N_r^l + \epsilon_f N_f^l \tag{7.7}$$

The two previous relations may be represented in the form of a two dimensional matrix

$$\begin{pmatrix} N^t \\ N^l \end{pmatrix} = \begin{pmatrix} \epsilon_r & \epsilon_f \\ (1-\epsilon_r) & (1-\epsilon_f) \end{pmatrix} = \begin{pmatrix} N_r^l \\ N_f^l \end{pmatrix} \tag{7.8}$$

For the di-lepton case, an event will be composed of either two real leptons, two fake leptons, or one of each. An inclusive sample would therefore include events with the p_T -ordered lepton real-fake combinations: rr, rf, fr, ff. The relation described in equation 8.3 is expanded to the dilepton case, leads to a 4×4 matrix relating the possible loose-tight combinations to the real-fake event composition. Following these notations, by we denote leptons passing the tight selection; by "l " - leptons passing the loose (and also tight) selections, i.e. inclusive loose leptons; and by "L" loose selection but not the tight one, i.e. exclusive loose leptons. The full matrix is:

$$\begin{pmatrix} N^{tt} \\ N^{Lt} \\ N^{tL} \\ N^{LL} \end{pmatrix} = M \begin{pmatrix} N_{rr}^{ll} \\ N_{rf}^{ll} \\ N_{fr}^{ll} \\ N_{ff}^{ll} \end{pmatrix} \tag{7.9}$$

with

$$M = \begin{pmatrix} \epsilon_r^1\epsilon_r^2 & \epsilon_r^1\epsilon_f^2 & \epsilon_f^1\epsilon_r^2 & \epsilon_f^1\epsilon_f^2 \\ \epsilon_r^1(1-\epsilon_r^2) & \epsilon_r^1(1-\epsilon_f^2) & \epsilon_f^1(1-\epsilon_r^2) & \epsilon_f^1(1-\epsilon_f^2) \\ (1-\epsilon_r^1)\epsilon_r^2 & (1-\epsilon_r^1)\epsilon_f^2 & (1-\epsilon_f^1)\epsilon_r^2 & (1-\epsilon_f^1)\epsilon_f^2 \\ (1-\epsilon_r^1)(1-\epsilon_r^2) & (1-\epsilon_r^1)(1-\epsilon_f^2) & (1-\epsilon_f^1)(1-\epsilon_r^2) & (1-\epsilon_f^1)(1-\epsilon_f^2) \end{pmatrix} \tag{7.10}$$

We are interested in the contribution of the reducible background in a two lepton final state. Therefore, total fake-lepton events, i.e. the number of events with double-fake and fake-real tight leptons, N_{rf}^{tt}, N_{fr}^{tt} and N_{ff}^{tt} can be found as

$$N_{fake-total}^{tt} = N_{rf}^{tt} + N_{fr}^{tt} + N_{ff}^{tt} = \epsilon_r^1\epsilon_f^2 N_{rf}^{ll} + \epsilon_f^1\epsilon_r^2 N_{fr}^{ll} + \epsilon_f^1\epsilon_f^2 N_{ff}^{ll}, \tag{7.11}$$

where N_{rf}^{ll}, N_{fr}^{ll} and N_{ff}^{ll} can be found by solving the matrix equation 7.9 for N_{rr}^{ll}, N_{rf}^{ll}, N_{fr}^{ll} and N_{ff}^{ll}.

The number of fake di-lepton events contributing to the signal sample can be defined in terms of the real-fake event composition (equations 7.10 and 7.11). Di-lepton events taken from a control sample containing at least one loose (and not tight) lepton are weighted by the probability for such an event to fall into the tight selection, with the matrix method permitting the determination of these event-by-event probabilities, or fake weights. A fake weight is derived for each event in the loose-not-tight lepton samples, and the events are then weighted accordingly. This method is applied to data, not MC, and so the matrix method is extremely useful in that it allows for a data-driven approach to the fake lepton background determination. Because this background is taken completely from data and accounts for all fake lepton background, MC events passing the di-lepton signal selection must not be fakes.

In an application to a particular analysis (in order to reproduce the shapes of the distributions) similarly to the single lepton case, one needs to redefine the total number of fake events in equation 7.11 in the signal region into the weight w^i to be applied to each data event i passing the loose or the tight selection, that an event contains at least one fake, by redefining each of N^{ll}_{rf}, N^{ll}_{fr} and N^{ll}_{ff} as partial weights, w^i_{rf}, w^i_{fr} and w^i_{ff}, entering the total weight w^i. This weight w^i is given by the expression

$$w_i = \epsilon^1_r \epsilon^2_f w^i_{rf} + \epsilon^1_f \epsilon^2_r w^i_{fr} + \epsilon^1_f \epsilon^2_f w^i_{ff}, \tag{7.12}$$

where , w^i_{rf}, w^i_{fr} and w^i_{ff} defined as:

$$\alpha = \frac{1}{(\epsilon^1_r - \epsilon^1_f)(\epsilon^2_r - \epsilon^2_f)}. \tag{7.13}$$

$$w^i_{rf} = \alpha(-(1-\epsilon^1_f)(1-\epsilon^2_r)\delta_{12} + (1-\epsilon^1_f)\epsilon^2_r\delta_1 + \epsilon^1_f(1-\epsilon^2_r)\delta_2 - \epsilon^1_f\epsilon^2_r(1-\delta_{12})); \tag{7.14}$$

$$w^i_{fr} = \alpha(-(1-\epsilon^1_r)(1-\epsilon^2_f)\delta_{12} + (1-\epsilon^1_r)\epsilon^2_f\delta_1 + \epsilon^1_r(1-\epsilon^2_f)\delta_2 - \epsilon^1_r\epsilon^2_f(1-\delta_{12})); \tag{7.15}$$

$$w^i_{ff} = \quad \alpha((1-\epsilon^1_r)(1-\epsilon^2_r)\delta_{12} - (1-\epsilon^1_r)\epsilon^2_r\delta_1 - \epsilon^1_r(1-\epsilon^2_r)\delta_2 + \epsilon^1_r\epsilon^2_r(1-\delta_{12})); \tag{7.16}$$

here δ_{12} is 1, when both leptons pass the tight selection; δ_1 is 1, when the first lepton passes the selection, but the second doesn't; and δ_2 is 1 when the first lepton doesn't pass the selection and the second one passes.

7.5.2 Extraction of Leptons Efficiencies

The method relies on determination of the real and fake efficiencies, ϵ_r and ϵ_f, from dedicated control samples. The efficiencies for real or fake loose leptons to also satisfy the tight criteria is defined as:

$$\epsilon_r = \frac{N_{real}^{tight}}{N_{real}^{loose}}, \quad \epsilon_f = \frac{N_{fake}^{tight}}{N_{fake}^{loose}} \tag{7.17}$$

where N_{real}^{tight} and N_{fake}^{tight} are the numbers of real and fake lepton events passing the tight selection criteria.

Lepton efficiencies in general depend on their kinematic variables, which has to be taken into account. Ideally this has to be done by calculating the efficiencies in bins of multi-dimension space of dependence variables. But in reality, when statistics is low, one calculates the efficiencies depending on only one single parameter and, in order to count the dependence on other kinematic variables, the efficiencies are parametrized. For example, in case of efficiency dependence on lepton P_T and η, first ϵ is calculated as a $\epsilon(P_T)$ and the dependence on η is parametrized like

$$\epsilon(P_T, \eta) = \epsilon(P_T) \times \frac{\epsilon(\eta)}{< \epsilon_\eta >}. \tag{7.18}$$

where $< \epsilon_\eta >$ is the average efficiency.

Statistical error calculation in efficiency computation has been done by constructing a confidence level intervals. In this method one constructs an interval $[\epsilon_{lo}, \epsilon_{hi}]$, into which the measured efficiencies fall with a predefined probability. For the analysis this probability has been set to 0.683 to be the same as the standard variation. The asymmetric errors are then computed as

$$\delta\epsilon_{up} = \epsilon_{hi} - \epsilon_{nom} \tag{7.19}$$

$$\delta\epsilon_{down} = \epsilon_{nom} - \epsilon_{lo}, \tag{7.20}$$

where ϵ_{nom} is a nominal efficiency [105].

7.5.2.1 Extraction of Real Efficiencies

The matrix method relies on suitable CRs for determining the fake rate and real efficiency. These QCD-enriched CRs are typically characterized by low missing transverse energy and moderate jet activity.

To extract the real lepton efficiencies, a region with as few fake lepton contamination as possible has to be selected. The measurement is carried out with a tag-and-probe method in a dedicated $Z \rightarrow ll$ control region, using the full 8TeV dataset. In this method one of the leptons coming from the Z-boson, selected as a tight lepton, is used as the tag and the other lepton, selected as a loose lepton, is used as the probe. The fraction of probe leptons, which also pass the tight selection cuts, defines the real lepton efficiency, ϵ_r. The leptons should be oppositely signed and the invariant mass should in the Z-mass window of 80 to 100 GeV. A cut on the E_{miss} has been set to $E_{miss} \geq 20$ GeV.

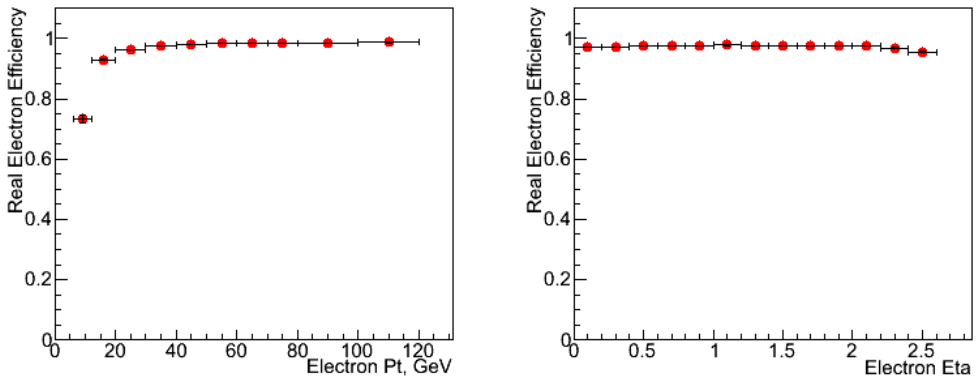

Figure 7.7: Real electron efficiencies calculated using $Z \rightarrow ee$ data sample. The "loose" electron is defined as the one passing baseline selection criteria and "tight" electron in addition passing MediumIso requirement.

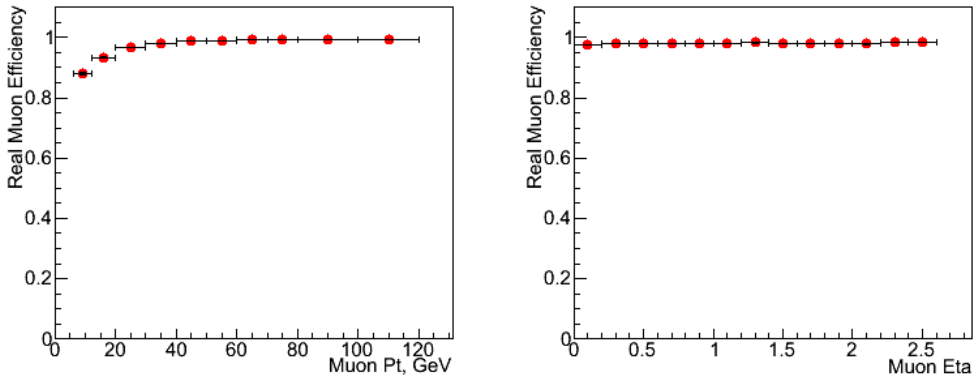

Figure 7.8: Real muon efficiencies calculated using $Z \to \mu\mu$ data sample. The "loose" muon is defined as the one passing baseline selection criteria and "tight" muon in addition passing MediumIso requerement.

Figure 7.7 shows real electron efficiencies calculated using $Z \to ee$ data sample and figure 7.8 shows real muon efficiencies calculated using $Z \to \mu\mu$ data sample as functions of p_T and η. It can be concluded from the plots, that the muon efficiency does not depend on η, while the electron efficiency shows some minimal dependency on the high η edge.

7.5.2.2 Extraction of Fake Efficiencies

To extract fake lepton efficiencies, real data is used by selecting a region enriched with fake leptons. Since realistic computer modeling of processes containing fake leptons is not possible, real data is used to extract fake lepton efficiencies. The fake lepton efficiencies is measured by selecting a region, which is enriched with fake leptons, which is characterized by low missing transverse energy and moderate jet activity. These requirements imply a cut on missing transverse energy $E_T^{miss} < 50$ GeV and having at least one jet with minimum p_T of 20 GeV. In addition, to remove

W+jets contamination, a cut on W transverse mass, $m_T < 10$ GeV, is set. Fake efficiency ϵ_f in a sample of pure fake events is given by

$$\epsilon_f = \frac{N^{tight}_{fake,Data}}{N^{loose}_{fake,Data}}, \tag{7.21}$$

where $N^{loose}_{fake,Data}$ is the number of events passing the loose selection and $N^{tight}_{fake,Data}$ is the number of events passing tight selection. But $N^{tight}_{fake,Data}$ and $N^{loose}_{fake,Data}$ in the real fake enriched regions contain also real leptons. This real lepton estimation is done using MC samples. Counting for this correction, the fake efficiency ϵ_f can be calculated as

$$\epsilon_f = \frac{N^{tight}_{fake,Data} - N^{tight}_{fake,MC}}{N^{loose}_{fake,Data} - N^{loose}_{fake,MC}}; \tag{7.22}$$

where $N^{tight}_{fake,MC}$ and $N^{loose}_{fake,MC}$ are total MC estimation from all real lepton sources taken into consideration.

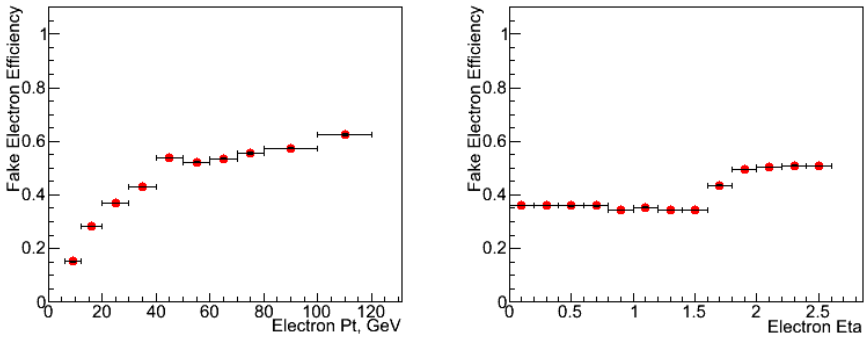

Figure 7.9: Fake electron efficiency calculated using QCD enriched data sample. The "loose" electron is defined as the one passing baseline selection criteria and "tight" one in addition passing MediumIso requirement.

Figures 7.9 and 7.10 show dependence of fake electron, ϵ^e_f, and muon, ϵ^μ_f, efficiencies on p_T and η, where the fake rate is quite high for both, electrons and muons.

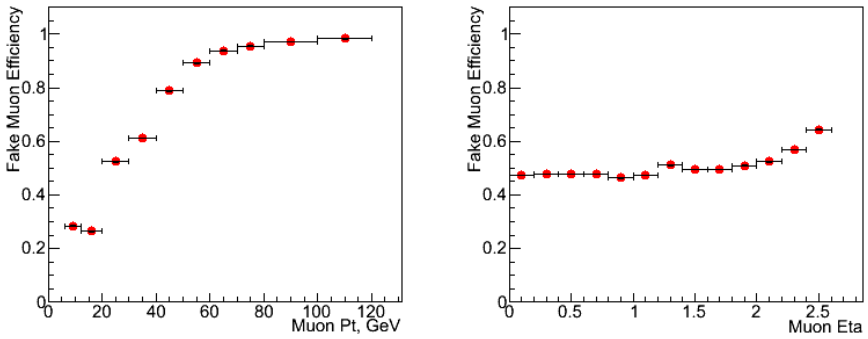

Figure 7.10: Fake muon efficiency calculated using QCD enriched data sample. The "loose" muon is defined as the one passing baseline selection criteria and "tight" one in addition passing MediumIso requirement.

The high fake rate for electrons is a hint of real electron contamination in the sample used to extract the fake rates. Similarly, the unrealistically high muon fake rates is observed, practically approaching 1 for muons with p_T higher than 60 GeV. This is because the sample used to evaluate muon fake rate at that p_T range is mostly composed of real muons despite the strong selection requirements. Further, fake rates of muons are seen above 0.5 in the p_T range of 30 to 60 GeV, which indicates that there is large real muon fraction in the sample used to extract muon fake rates. Therefore, in computation of fake muon weights for muons with $p_T > 40$ GeV, the fake rates were taken to be the same as for muons in the p_T interval of 30 to 40 GeV.

The consequence of the overestimation of the fake rate would be a corresponding overestimation of the fake lepton contamination in the selected events unless the selection requirements remove these events. But, further selection criteria will indeed cut out the fakes leptons completely, which, taking into account also the fact of overestimation of fake rates, insures us of the cleanness of the selected sample in terms of fake contamination.

7.5.3 Lepton Fake Weights

The fake weights is calculated by matrix method to the data sample using the extracted fake electron and muon rates and creating fake-ntuples. Figure 7.11 shows the corresponding fake lepton weights obtained by the matrix method for the data collected by the leptonic and by the MET triggers.

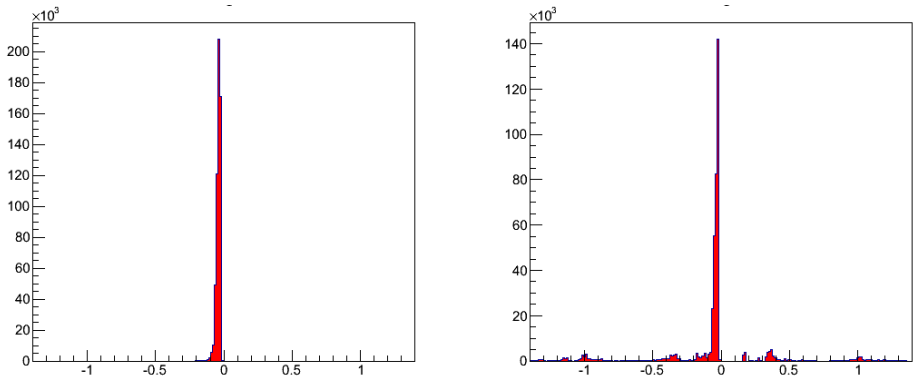

Figure 7.11: Fake lepton weights obtained by applying matrix method to the data sample using real and fake lepton efficiencies for data collected by the lepton triggers, left, and by the MET triggers, right.

The weight distribution for the case of leptonic triggers shows no positive weights, whereas MET trigger case instead shows some positive weights. This implies that there is no fake contamination in the sample for the case of leptonic triggers. The MET trigger has the potential possibility to contain some fake leptons, since the MET triggers allow passing soft leptons. The fake ntuples are further used in the analysis as a standard MC samples to describe the data and extract the signal by fitting.

7.5.3.1 Systematic Uncertainties

To estimate systematic uncertainty related with the fake lepton contamination in the SR coming from uncertainty of fake rate computation, the definitions of QCD enriched regions used to extract fake rates were changed by moving the cut on the transverse mass from $m_T < 10$ GeV to $m_T < 20$ GeV for both, electrons and muons, and calculating again the fake contamination in the selected data events. The obtained fake rates and, correspondingly, fake weights show only small difference with respect to the nominal case.

7.6 The background Fit Results

The results obtained with the background only fit mode of HistFitter are presented here, which provides the best estimate of the background yields in the SRs and VRs. This mode used the expected MC yields in all the regions and the observed yields in the CRs. If used in the background only fit configuration, the HistFitter package performs a likelihood fit for all CRs, excluding the SRs. No signal component is included in the likelihood. Then, the resulting normalization factors are extrapolated to the signal and validation regions.

The data in the CRs are used to determine the $t\tilde{t}$ normalization factors μ_T and yields in the CRs, SRs and VRs. No shape information is used, and a single bin for the BDTG distribution in each CR and in each SR and VR is considered. The fit doesn't constrain the nuisance parameters, whose central value is always very close to zero and the error very close to 1. Depending on each background sample, systematics are properly considered by exploiting the different options available in HistFitter. Between the two different methods to treat systematics in the fit, the one which applies one systematic at a time and runs the fit was chosen, and then used

calculate the error propagation due to systematics. Then, the final error on the fitted total background in the CRs, VRs and SRs are properly takes into account with the correlation matrix between the different errors.

The cross section uncertainty is modeled by an overall nuisance parameter. The generator systematics on $t\tilde{t}$ modeling are decomposed into several components: the ISR/FSR variations and the MC generator comparisons. In the fit a more accurate modeling is allowed, by introducing three nuisance parameters. Several information are listed in the following section, which describes the final output of the background only fit:

- The observed events in data and the expected background rates with their uncertainties before and after the background fit in each SR and the corresponding CR and VR, are listed in tables from 7.8 to 7.18. The fitted backgrounds are compatible both with MC predictions and observed data within uncertainties. The figure of merit is the fit error on the total background in the SRs or CRs. The observed and the total expected background events are also summarized for all SRs in table 7.6.
- The $t\tilde{t}$ normalization factors are summarized in table 7.7 as provided by the background only fit. As a consequence of the fact that each SR has its own dedicated CR, the normalization factors across the various SRs can be different in principle, and this could be due to the fact that MC might not perfectly model the variables on which the various CRs/SRs have different requirements. In this analysis the final results for MET trigger based SRs are all similar within errors, as can be observed in figure 7.12, and the same holds for the lepton trigger based SRs.
- For each individual background channel in the CRs and in the VRs, the breakdown in individual sources of the total systematic and statistical (terms "mc-

stat") uncertainty, before (based on MC expectations) and after the fit, are reported in tables from 1 to 44 (supplemental file).

- For each individual background channel in the SRs, the breakdown in individual sources of the total systematic and statistical (terms "mcstat") uncertainty, before (based on MC expectations) and after the fit, are reported in tables from 45 to 66 (supplemental file).

Table 7.6: Observed events and total expected background events from the background-only fit, for the different signal regions. The quoted errors take into account both statistical and systematic uncertainties.

	SR_1^{DF}	SR_2^{DF}	SR_3^{DF}	SR_4^{DF}	SR_5^{DF}	SR_6^{DF}
Observed events	5	1	1	3	8	4
Fitted bkg events	4.07 ± 1.45	2.06 ± 1.53	1.22 ± 0.88	4.09 ± 1.07	8.26 ± 4.44	3.34 ± 1.79

	SR_1^{SF}	SR_2^{SF}	SR_3^{SF}	SR_4^{SF}	SR_5^{SF}
Observed events	5	10	4	9	2
Fitted bkg events	7.25 ± 2.49	6.16 ± 1.48	2.95 ± 0.99	6.33 ± 1.57	5.50 ± 1.78

Table 7.7: $t\tilde{t}$ normalization factor provided by the HistFitter background only fit. The quoted errors take into account both statistical and systematic uncertainties.

	CR_1^{DF}	CR_2^{DF}	CR_3^{DF}	CR_4^{DF}	CR_5^{DF}	CR_6^{DF}
Scale factor	0.71 ± 0.10	0.72 ± 0.10	0.71 ± 0.10	0.91 ± 0.15	1.17 ± 0.20	1.37± 0.37

	CR_1^{SF}	CR_2^{SF}	CR_3^{SF}	CR_4^{SF}	CR_5^{SF}
Scale factor	0.70± 0.09	0.70 ± 0.09	0.70± 0.09	1.11± 0.16	1.02± 0.14

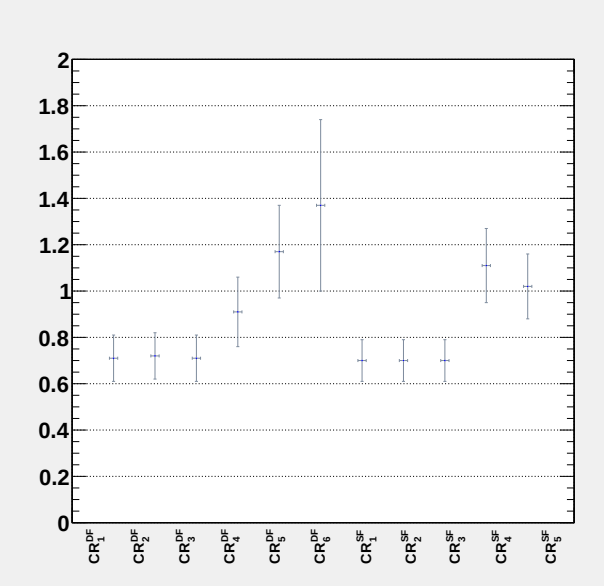

Figure 7.12: $t\tilde{t}$ normalization factors as provided by the background only fit.

Table 7.8: Background fit results for the SR_1^{DF}, VR_1^{DF} and CR_1^{DF} regions, for an integrated luminosity of 20.1 fb^{-1}. Nominal MC expectations (normalised to MC cross-sections) are given for comparison. The errors shown are the statistical plus systematic uncertainties.

channel	SR_1^{DF}	VR_1^{DF}	CR_1^{DF}
Observed events	5	93	5544
Fitted bkg events	4.07 ± 1.45	94.63 ± 21.41	5543.24 ± 75.11
Fitted tZ events	$0.00^{+0.00}_{-0.00}$	$0.01^{+0.01}_{-0.01}$	0.46 ± 0.46
Fitted Wt events	$0.37^{+0.49}_{-0.37}$	6.02 ± 2.49	252.73 ± 54.81
Fitted H events	$0.01^{+0.01}_{-0.01}$	$0.02^{+0.02}_{-0.02}$	1.86 ± 0.27
Fitted WW events	$0.00^{+0.11}_{-0.00}$	$0.14^{+0.26}_{-0.14}$	$14.12^{+29.20}_{-14.12}$
Fitted ZZ events	0.00 ± 0.00	$0.00^{+0.00}_{-0.00}$	$0.02^{+0.10}_{-0.02}$
Fitted WZ events	$0.00^{+0.00}_{-0.00}$	0.12 ± 0.11	$0.68^{+1.52}_{-0.68}$
Fitted $t\bar{t}W + t\bar{t}Z + t\bar{t}WW$ events	0.13 ± 0.05	0.81 ± 0.24	21.47 ± 4.80
Fitted DY events	0.00 ± 0.00	0.00 ± 0.00	$0.37^{+0.67}_{-0.37}$
Fitted Z events	$0.29^{+0.33}_{-0.29}$	$4.63^{+4.77}_{-4.63}$	37.59 ± 29.21
Fitted $t\bar{t}$ events	3.26 ± 1.25	46.79 ± 6.22	3960.37 ± 165.51
Fitted $Fakes$ events	0.00 ± 0.00	36.08 ± 19.83	1253.58 ± 125.24
MC exp. SM events	5.37 ± 2.05	113.37 ± 25.51	7127.54 ± 725.66
MC exp. tZ events	$0.00^{+0.00}_{-0.00}$	$0.01^{+0.01}_{-0.01}$	$0.46^{+0.46}_{-0.46}$
MC exp. Wt events	$0.37^{+0.49}_{-0.37}$	6.02 ± 2.50	252.75 ± 55.25
MC exp. H events	$0.01^{+0.01}_{-0.01}$	$0.02^{+0.02}_{-0.02}$	1.86 ± 0.27
MC exp. WW events	$0.00^{+0.11}_{-0.00}$	$0.14^{+0.26}_{-0.14}$	$14.04^{+29.20}_{-14.04}$
MC exp. ZZ events	0.00 ± 0.00	$0.00^{+0.00}_{-0.00}$	$0.02^{+0.10}_{-0.02}$
MC exp. WZ events	$0.00^{+0.00}_{-0.00}$	0.12 ± 0.11	$0.68^{+1.53}_{-0.68}$
MC exp. $t\bar{t}W + t\bar{t}Z + t\bar{t}WW$ events	0.13 ± 0.05	0.81 ± 0.24	21.47 ± 4.84
MC exp. DY events	0.00 ± 0.00	0.00 ± 0.00	$0.77^{+0.79}_{-0.77}$
MC exp. Z events	$0.29^{+0.33}_{-0.29}$	$4.64^{+4.80}_{-4.64}$	37.61 ± 29.40
MC exp. $t\bar{t}$ events	4.56 ± 1.86	65.53 ± 14.74	5544.34 ± 698.04
data-driven exp. $Fakes$ events	0.00 ± 0.00	36.08 ± 19.83	1253.55 ± 126.02

Table 7.9: Background fit results for the SR_2^{DF}, VR_2^{DF} and CR_2^{DF} regions, for an integrated luminosity of 20.1 fb^{-1}. Nominal MC expectations (normalised to MC cross-sections) are given for comparison. The errors shown are the statistical plus systematic uncertainties.

channel	SR_2^{DF}	VR_2^{DF}	CR_2^{DF}
Observed events	1	80	5561
Fitted bkg events	2.06 ± 1.53	89.34 ± 19.00	5559.87 ± 75.28
Fitted tZ events	$0.00^{+0.00}_{-0.00}$	$0.01^{+0.01}_{-0.01}$	0.46 ± 0.46
Fitted Wt events	$0.00^{+0.49}_{-0.00}$	5.41 ± 2.19	253.71 ± 55.03
Fitted H events	$0.00^{+0.01}_{-0.00}$	0.03 ± 0.03	1.86 ± 0.27
Fitted WW events	0.00 ± 0.00	$0.19^{+0.37}_{-0.19}$	$14.11^{+29.27}_{-14.11}$
Fitted ZZ events	0.00 ± 0.00	$0.00^{+0.00}_{-0.00}$	$0.02^{+0.10}_{-0.02}$
Fitted WZ events	$0.00^{+0.00}_{-0.00}$	0.13 ± 0.08	$0.67^{+1.49}_{-0.67}$
Fitted $t\bar{t}W + t\bar{t}Z + t\bar{t}WW$ events	0.07 ± 0.03	0.82 ± 0.24	21.52 ± 4.82
Fitted DY events	0.00 ± 0.00	0.00 ± 0.00	$0.37^{+0.67}_{-0.37}$
Fitted Z events	$0.10^{+0.26}_{-0.10}$	$4.54^{+4.75}_{-4.54}$	37.86 ± 29.59
Fitted $t\bar{t}$ events	1.88 ± 1.07	51.39 ± 6.42	3966.55 ± 166.09
Fitted $Fakes$ events	0.00 ± 0.00	26.82 ± 17.17	1262.74 ± 125.71
MC exp. SM events	2.81 ± 2.10	109.72 ± 23.69	7133.62 ± 725.39
MC exp. tZ events	$0.00^{+0.00}_{-0.00}$	$0.01^{+0.01}_{-0.01}$	$0.46^{+0.46}_{-0.46}$
MC exp. Wt events	$0.00^{+0.50}_{-0.00}$	5.41 ± 2.19	253.73 ± 55.49
MC exp. H events	$0.00^{+0.01}_{-0.00}$	0.03 ± 0.03	1.86 ± 0.27
MC exp. WW events	0.00 ± 0.00	$0.19^{+0.37}_{-0.19}$	$13.99^{+29.19}_{-13.99}$
MC exp. ZZ events	0.00 ± 0.00	$0.00^{+0.00}_{-0.00}$	$0.02^{+0.10}_{-0.02}$
MC exp. WZ events	$0.00^{+0.00}_{-0.00}$	0.13 ± 0.08	$0.67^{+1.49}_{-0.67}$
MC exp. $t\bar{t}W + t\bar{t}Z + t\bar{t}WW$ events	0.07 ± 0.03	0.82 ± 0.24	21.52 ± 4.85
MC exp. DY events	0.00 ± 0.00	0.00 ± 0.00	$0.77^{+0.79}_{-0.77}$
MC exp. Z events	$0.10^{+0.26}_{-0.10}$	$4.55^{+4.78}_{-4.55}$	37.89 ± 29.78
MC exp. $t\bar{t}$ events	2.63 ± 1.64	71.76 ± 15.06	5540.04 ± 697.79
data-driven exp. $Fakes$ events	0.00 ± 0.00	26.82 ± 17.17	1262.67 ± 126.48

Table 7.10: Background fit results for the SR_3^{DF}, VR_3^{DF} and CR_3^{DF} regions, for an integrated luminosity of 20.1 fb^{-1}. Nominal MC expectations (normalised to MC cross-sections) are given for comparison. The errors shown are the statistical plus systematic uncertainties.

channel	SR_3^{DF}	VR_3^{DF}	CR_3^{DF}
Observed events	1	34	5607
Fitted bkg events	1.22 ± 0.88	39.00 ± 10.53	5605.73 ± 75.65
Fitted tZ events	$0.00^{+0.00}_{-0.00}$	$0.00^{+0.00}_{-0.00}$	0.46 ± 0.46
Fitted Wt events	$0.02^{+0.13}_{-0.02}$	4.08 ± 1.76	255.18 ± 54.93
Fitted H events	0.00 ± 0.00	0.03 ± 0.03	1.86 ± 0.27
Fitted WW events	$0.00^{+0.05}_{-0.00}$	0.14 ± 0.11	$13.89^{+29.30}_{-13.89}$
Fitted ZZ events	0.00 ± 0.00	0.00 ± 0.00	$0.02^{+0.10}_{-0.02}$
Fitted WZ events	$0.00^{+0.01}_{-0.00}$	$0.01^{+0.01}_{-0.01}$	$0.79^{+1.57}_{-0.79}$
Fitted $t\bar{t}W + t\bar{t}Z + t\bar{t}WW$ events	0.04 ± 0.02	0.42 ± 0.15	21.96 ± 4.92
Fitted DY events	0.00 ± 0.00	0.00 ± 0.00	$0.37^{+0.67}_{-0.37}$
Fitted Z events	$0.08^{+0.10}_{-0.08}$	$2.25^{+2.36}_{-2.25}$	40.26 ± 31.81
Fitted $t\bar{t}$ events	1.08 ± 0.88	23.39 ± 3.46	3990.16 ± 167.39
Fitted $Fakes$ events	0.00 ± 0.00	$8.68^{+9.29}_{-8.68}$	1280.78 ± 126.62
MC exp. SM events	1.65 ± 1.28	48.32 ± 13.02	7196.17 ± 732.23
MC exp. tZ events	$0.00^{+0.00}_{-0.00}$	$0.00^{+0.00}_{-0.00}$	$0.46^{+0.46}_{-0.46}$
MC exp. Wt events	$0.02^{+0.13}_{-0.02}$	4.07 ± 1.76	255.05 ± 55.37
MC exp. H events	0.00 ± 0.00	0.03 ± 0.03	1.86 ± 0.27
MC exp. WW events	$0.00^{+0.05}_{-0.00}$	0.14 ± 0.12	$14.03^{+29.39}_{-14.03}$
MC exp. ZZ events	0.00 ± 0.00	0.00 ± 0.00	$0.03^{+0.10}_{-0.03}$
MC exp. WZ events	$0.00^{+0.01}_{-0.00}$	$0.01^{+0.01}_{-0.01}$	$0.79^{+1.58}_{-0.79}$
MC exp. $t\bar{t}W + t\bar{t}Z + t\bar{t}WW$ events	0.04 ± 0.02	0.42 ± 0.15	21.95 ± 4.95
MC exp. DY events	0.00 ± 0.00	0.00 ± 0.00	$0.77^{+0.79}_{-0.77}$
MC exp. Z events	$0.08^{+0.10}_{-0.08}$	$2.24^{+2.38}_{-2.24}$	40.22 ± 32.01
MC exp. $t\bar{t}$ events	1.51 ± 1.27	32.72 ± 7.72	5580.19 ± 704.67
data-driven exp. $Fakes$ events	0.00 ± 0.00	$8.68^{+9.29}_{-8.68}$	1280.82 ± 127.39

Table 7.11: Background fit results for the SR_4^{DF}, VR_4^{DF} and CR_4^{DF} regions, for an integrated luminosity of 20.3 fb^{-1}. Nominal MC expectations (normalised to MC cross-sections) are given for comparison. The errors shown are the statistical plus systematic uncertainties.

channel	SR_4^{DF}	VR_4^{DF}	CR_4^{DF}
Observed events	3	973	2281
Fitted bkg events	4.09 ± 1.07	850.99 ± 219.10	2281.01 ± 118.54
Fitted tZ events	$0.00^{+0.00}_{-0.00}$	$0.16^{+0.17}_{-0.16}$	0.39 ± 0.39
Fitted Wt events	$0.11^{+0.15}_{-0.11}$	55.39 ± 13.90	125.66 ± 29.33
Fitted H events	0.00 ± 0.00	1.72 ± 0.28	3.48 ± 0.52
Fitted WW events	0.97 ± 0.23	60.22 ± 13.03	83.12 ± 25.14
Fitted ZZ events	$0.02^{+0.02}_{-0.02}$	0.11 ± 0.09	0.14 ± 0.04
Fitted WZ events	$0.01^{+0.01}_{-0.01}$	3.92 ± 1.93	7.04 ± 1.03
Fitted $t\bar{t}W + t\bar{t}Z + t\bar{t}WW$ events	0.39 ± 0.11	9.48 ± 2.23	13.89 ± 3.25
Fitted DY events	0.00 ± 0.00	0.00 ± 0.00	0.00 ± 0.00
Fitted Z events	$0.02^{+0.02}_{-0.02}$	33.49 ± 19.85	90.54 ± 44.07
Fitted $t\bar{t}$ events	2.59 ± 0.98	686.50 ± 215.66	1956.76 ± 135.37
Fitted $Fakes$ events	0.00 ± 0.00	0.00 ± 0.00	0.00 ± 0.00
MC exp. SM events	4.35 ± 1.38	919.53 ± 291.33	2474.07 ± 381.48
MC exp. tZ events	$0.00^{+0.00}_{-0.00}$	$0.16^{+0.17}_{-0.16}$	$0.39^{+0.39}_{-0.39}$
MC exp. Wt events	$0.11^{+0.15}_{-0.11}$	55.39 ± 13.98	125.66 ± 29.52
MC exp. H events	0.00 ± 0.00	1.72 ± 0.28	3.48 ± 0.52
MC exp. WW events	0.97 ± 0.23	60.22 ± 13.11	83.11 ± 25.31
MC exp. ZZ events	$0.02^{+0.02}_{-0.02}$	0.11 ± 0.09	0.14 ± 0.04
MC exp. WZ events	$0.01^{+0.01}_{-0.01}$	3.92 ± 1.95	7.04 ± 1.04
MC exp. $t\bar{t}W + t\bar{t}Z + t\bar{t}WW$ events	0.39 ± 0.11	9.48 ± 2.24	13.89 ± 3.27
MC exp. DY events	0.00 ± 0.00	0.00 ± 0.00	0.00 ± 0.00
MC exp. Z events	$0.02^{+0.02}_{-0.02}$	33.49 ± 19.98	90.54 ± 44.36
MC exp. $t\bar{t}$ events	2.84 ± 1.27	755.03 ± 283.19	2149.82 ± 358.22
data-driven exp. $Fakes$ events	0.00 ± 0.00	0.00 ± 0.00	0.00 ± 0.00

Table 7.12: Background fit results for the SR_5^{DF}, VR_5^{DF} and CR_5^{DF} regions, for an integrated luminosity of 20.3 fb^{-1}. Nominal MC expectations (normalised to MC cross-sections) are given for comparison. The errors shown are the statistical plus systematic uncertainties.

channel	SR_5^{DF}	VR_5^{DF}	CR_5^{DF}
Observed events	8	192	311
Fitted bkg events	8.26 ± 4.44	159.46 ± 18.82	311.09 ± 18.47
Fitted tZ events	$0.00^{+0.00}_{-0.00}$	$0.04^{+0.04}_{-0.04}$	$0.02^{+0.02}_{-0.02}$
Fitted Wt events	0.41 ± 0.39	8.51 ± 3.87	16.72 ± 4.75
Fitted H events	$0.00^{+0.01}_{-0.00}$	0.14 ± 0.06	0.18 ± 0.06
Fitted WW events	1.91 ± 1.45	9.71 ± 2.02	14.41 ± 6.35
Fitted ZZ events	$0.02^{+0.02}_{-0.02}$	0.02 ± 0.02	$0.01^{+0.01}_{-0.01}$
Fitted WZ events	$0.23^{+0.25}_{-0.23}$	$0.41^{+0.53}_{-0.41}$	$0.75^{+0.86}_{-0.75}$
Fitted $t\bar{t}W + t\bar{t}Z + t\bar{t}WW$ events	0.68 ± 0.17	1.72 ± 0.41	1.58 ± 0.38
Fitted DY events	0.00 ± 0.00	0.00 ± 0.00	0.00 ± 0.00
Fitted Z events	$0.01^{+0.01}_{-0.01}$	$0.26^{+0.26}_{-0.26}$	$1.03^{+1.05}_{-1.03}$
Fitted $t\bar{t}$ events	5.00 ± 4.19	138.65 ± 17.56	276.38 ± 20.22
Fitted $Fakes$ events	0.00 ± 0.00	0.00 ± 0.00	0.00 ± 0.00
MC exp. SM events	7.54 ± 4.29	139.08 ± 29.06	270.32 ± 39.34
MC exp. tZ events	$0.00^{+0.00}_{-0.00}$	$0.04^{+0.04}_{-0.04}$	$0.02^{+0.02}_{-0.02}$
MC exp. Wt events	0.41 ± 0.39	8.51 ± 3.89	16.71 ± 4.78
MC exp. H events	$0.00^{+0.01}_{-0.00}$	0.14 ± 0.06	0.18 ± 0.06
MC exp. WW events	1.91 ± 1.46	9.71 ± 2.04	14.41 ± 6.39
MC exp. ZZ events	$0.02^{+0.02}_{-0.02}$	0.02 ± 0.02	$0.01^{+0.02}_{-0.01}$
MC exp. WZ events	$0.23^{+0.25}_{-0.23}$	$0.41^{+0.53}_{-0.41}$	$0.75^{+0.87}_{-0.75}$
MC exp. $t\bar{t}W + t\bar{t}Z + t\bar{t}WW$ events	0.68 ± 0.17	1.72 ± 0.41	1.58 ± 0.38
MC exp. DY events	0.00 ± 0.00	0.00 ± 0.00	0.00 ± 0.00
MC exp. Z events	$0.01^{+0.01}_{-0.01}$	$0.25^{+0.26}_{-0.25}$	$1.03^{+1.06}_{-1.03}$
MC exp. $t\bar{t}$ events	4.28 ± 3.98	118.28 ± 27.19	235.62 ± 38.55
data-driven exp. $Fakes$ events	0.00 ± 0.00	0.00 ± 0.00	0.00 ± 0.00

Table 7.13: Background fit results for the SR_6^{DF}, VR_6^{DF} and CR_6^{DF} regions, for an integrated luminosity of 20.3 fb^{-1}. Nominal MC expectations (normalised to MC cross-sections) are given for comparison. The errors shown are the statistical plus systematic uncertainties.

channel	SR_6^{DF}	VR_6^{DF}	CR_6^{DF}
Observed events	4	228	498
Fitted bkg events	3.34 ± 1.79	243.91 ± 34.74	498.66 ± 27.62
Fitted tZ events	$0.01^{+0.01}_{-0.01}$	$0.06^{+0.06}_{-0.06}$	$0.05^{+0.05}_{-0.05}$
Fitted Wt events	0.41 ± 0.39	13.44 ± 5.78	29.58 ± 7.81
Fitted H events	$0.00^{+0.01}_{-0.00}$	0.33 ± 0.10	0.64 ± 0.20
Fitted WW events	1.23 ± 0.71	21.07 ± 5.38	27.18 ± 10.71
Fitted ZZ events	$0.02^{+0.03}_{-0.02}$	0.03 ± 0.02	0.04 ± 0.03
Fitted WZ events	$0.21^{+0.24}_{-0.21}$	$1.05^{+1.07}_{-1.05}$	1.92 ± 0.61
Fitted $t\bar{t}W + t\bar{t}Z + t\bar{t}WW$ events	0.42 ± 0.12	2.63 ± 0.61	2.79 ± 0.69
Fitted DY events	0.00 ± 0.00	0.00 ± 0.00	0.00 ± 0.00
Fitted Z events	0.00 ± 0.00	$2.57^{+2.59}_{-2.57}$	$5.97^{+8.47}_{-5.97}$
Fitted $t\bar{t}$ events	$1.03^{+1.56}_{-1.03}$	202.73 ± 33.02	430.48 ± 32.27
Fitted $Fakes$ events	0.00 ± 0.00	0.00 ± 0.00	0.00 ± 0.00
MC exp. SM events	3.07 ± 1.51	188.44 ± 48.61	379.71 ± 79.99
MC exp. tZ events	$0.01^{+0.01}_{-0.01}$	$0.06^{+0.06}_{-0.06}$	$0.05^{+0.05}_{-0.05}$
MC exp. Wt events	0.41 ± 0.39	13.47 ± 5.81	29.62 ± 7.84
MC exp. H events	$0.00^{+0.01}_{-0.00}$	0.33 ± 0.10	0.64 ± 0.20
MC exp. WW events	1.23 ± 0.71	21.10 ± 5.41	27.23 ± 10.78
MC exp. ZZ events	$0.02^{+0.03}_{-0.02}$	0.03 ± 0.02	0.04 ± 0.03
MC exp. WZ events	$0.21^{+0.24}_{-0.21}$	$1.05^{+1.08}_{-1.05}$	1.92 ± 0.62
MC exp. $t\bar{t}W + t\bar{t}Z + t\bar{t}WW$ events	0.42 ± 0.12	2.63 ± 0.62	2.80 ± 0.69
MC exp. DY events	0.00 ± 0.00	0.00 ± 0.00	0.00 ± 0.00
MC exp. Z events	0.00 ± 0.00	$2.57^{+2.62}_{-2.57}$	$6.00^{+8.58}_{-6.00}$
MC exp. $t\bar{t}$ events	$0.76^{+1.21}_{-0.76}$	147.21 ± 46.02	311.43 ± 76.22
data-driven exp. $Fakes$ events	0.00 ± 0.00	0.00 ± 0.00	0.00 ± 0.00

Table 7.14: Background fit results for the SR_1^{SF}, VR_1^{SF} and CR_1^{SF} regions, for an integrated luminosity of 20.1 fb^{-1}. Nominal MC expectations (normalised to MC cross-sections) are given for comparison. The errors shown are the statistical plus systematic uncertainties.

channel	SR_1^{SF}	VR_1^{SF}	CR_1^{SF}
Observed events	5	80	5747
Fitted bkg events	7.25 ± 2.49	81.27 ± 19.78	5746.26 ± 76.35
Fitted tZ events	$0.00^{+0.00}_{-0.00}$	$0.01^{+0.01}_{-0.01}$	2.20 ± 2.19
Fitted Wt events	0.00 ± 0.00	4.32 ± 1.73	282.63 ± 61.02
Fitted H events	$0.00^{+0.00}_{-0.00}$	$0.00^{+0.02}_{-0.00}$	4.11 ± 0.40
Fitted WW events	$0.08^{+0.09}_{-0.08}$	$0.04^{+0.23}_{-0.04}$	$14.80^{+28.84}_{-14.80}$
Fitted ZZ events	$0.00^{+0.01}_{-0.00}$	$0.00^{+0.03}_{-0.00}$	$2.96^{+3.63}_{-2.96}$
Fitted WZ events	$0.01^{+0.09}_{-0.01}$	$0.08^{+0.39}_{-0.08}$	$4.69^{+5.11}_{-4.69}$
Fitted $t\bar{t}W + t\bar{t}Z + t\bar{t}WW$ events	0.19 ± 0.07	0.90 ± 0.23	25.42 ± 5.70
Fitted DY events	0.00 ± 0.00	0.00 ± 0.00	4.28 ± 1.59
Fitted Z events	$0.77^{+0.90}_{-0.77}$	$1.43^{+1.55}_{-1.43}$	70.17 ± 42.00
Fitted $t\bar{t}$ events	6.20 ± 2.25	47.95 ± 9.70	3957.13 ± 176.30
Fitted $Fakes$ events	0.00 ± 0.00	26.54 ± 17.17	1377.87 ± 131.13
MC exp. SM events	9.92 ± 3.94	101.87 ± 24.49	7448.16 ± 724.55
MC exp. tZ events	$0.00^{+0.00}_{-0.00}$	$0.01^{+0.01}_{-0.01}$	2.20 ± 2.20
MC exp. Wt events	0.00 ± 0.00	4.32 ± 1.74	282.63 ± 61.50
MC exp. H events	$0.00^{+0.00}_{-0.00}$	$0.00^{+0.02}_{-0.00}$	4.11 ± 0.40
MC exp. WW events	$0.08^{+0.09}_{-0.08}$	$0.04^{+0.23}_{-0.04}$	$14.81^{+28.90}_{-14.81}$
MC exp. ZZ events	$0.00^{+0.01}_{-0.00}$	$0.00^{+0.03}_{-0.00}$	$2.96^{+3.65}_{-2.96}$
MC exp. WZ events	$0.01^{+0.09}_{-0.01}$	$0.08^{+0.39}_{-0.08}$	$4.69^{+5.14}_{-4.69}$
MC exp. $t\bar{t}W + t\bar{t}Z + t\bar{t}WW$ events	0.19 ± 0.07	0.90 ± 0.23	25.42 ± 5.73
MC exp. DY events	0.00 ± 0.00	0.00 ± 0.00	4.29 ± 1.60
MC exp. Z events	$0.77^{+0.90}_{-0.77}$	$1.43^{+1.56}_{-1.43}$	70.17 ± 42.27
MC exp. $t\bar{t}$ events	8.87 ± 3.70	68.55 ± 17.10	5659.02 ± 694.10
data-driven exp. $Fakes$ events	0.00 ± 0.00	26.54 ± 17.17	1377.87 ± 131.95

Table 7.15: Background fit results for the SR_2^{SF}, VR_2^{SF} and CR_2^{SF} regions, for an integrated luminosity of 20.1 fb^{-1}. Nominal MC expectations (normalised to MC cross-sections) are given for comparison. The errors shown are the statistical plus systematic uncertainties.

channel	SR_2^{SF}	VR_2^{SF}	CR_2^{SF}
Observed events	10	74	5748
Fitted bkg events	6.16 ± 1.48	74.06 ± 17.45	5747.37 ± 76.28
Fitted tZ events	$0.00^{+0.00}_{-0.00}$	$0.01^{+0.02}_{-0.01}$	2.20 ± 2.18
Fitted Wt events	$0.10^{+0.33}_{-0.10}$	5.65 ± 2.34	280.84 ± 60.36
Fitted H events	0.00 ± 0.00	$0.02^{+0.03}_{-0.02}$	4.10 ± 0.41
Fitted WW events	$0.07^{+0.11}_{-0.07}$	$0.11^{+0.24}_{-0.11}$	$14.71^{+28.82}_{-14.71}$
Fitted ZZ events	0.00 ± 0.00	$0.00^{+0.03}_{-0.00}$	$2.96^{+3.64}_{-2.96}$
Fitted WZ events	$0.01^{+0.14}_{-0.01}$	$0.08^{+0.31}_{-0.08}$	$4.68^{+5.13}_{-4.68}$
Fitted $t\bar{t}W + t\bar{t}Z + t\bar{t}WW$ events	0.23 ± 0.08	0.87 ± 0.25	25.42 ± 5.69
Fitted DY events	0.00 ± 0.00	$0.02^{+0.09}_{-0.02}$	4.26 ± 1.56
Fitted Z events	$0.72^{+0.76}_{-0.72}$	$2.78^{+2.93}_{-2.78}$	68.86 ± 40.72
Fitted $t\bar{t}$ events	5.03 ± 1.10	47.57 ± 9.24	3951.70 ± 176.00
Fitted $Fakes$ events	0.00 ± 0.00	16.95 ± 14.02	1387.64 ± 131.57
MC exp. SM events	8.34 ± 2.40	94.58 ± 23.12	7456.86 ± 723.67
MC exp. tZ events	$0.00^{+0.00}_{-0.00}$	$0.01^{+0.02}_{-0.01}$	2.20 ± 2.19
MC exp. Wt events	$0.10^{+0.33}_{-0.10}$	5.65 ± 2.35	280.85 ± 60.83
MC exp. H events	0.00 ± 0.00	$0.02^{+0.03}_{-0.02}$	4.10 ± 0.41
MC exp. WW events	$0.07^{+0.11}_{-0.07}$	$0.11^{+0.24}_{-0.11}$	$14.74^{+28.91}_{-14.74}$
MC exp. ZZ events	0.00 ± 0.00	$0.00^{+0.03}_{-0.00}$	$2.96^{+3.67}_{-2.96}$
MC exp. WZ events	$0.01^{+0.14}_{-0.01}$	$0.08^{+0.32}_{-0.08}$	$4.68^{+5.17}_{-4.68}$
MC exp. $t\bar{t}W + t\bar{t}Z + t\bar{t}WW$ events	0.23 ± 0.08	0.87 ± 0.25	25.42 ± 5.73
MC exp. DY events	0.00 ± 0.00	$0.02^{+0.09}_{-0.02}$	4.27 ± 1.56
MC exp. Z events	$0.72^{+0.77}_{-0.72}$	$2.78^{+2.95}_{-2.78}$	68.86 ± 40.98
MC exp. $t\bar{t}$ events	7.20 ± 2.08	68.09 ± 16.95	5661.14 ± 693.95
data-driven exp. $Fakes$ events	0.00 ± 0.00	16.95 ± 14.02	1387.64 ± 132.40

Table 7.16: Background fit results for the SR_3^{SF}, VR_3^{SF} and CR_3^{SF} regions, for an integrated luminosity of 20.1 fb^{-1}. Nominal MC expectations (normalised to MC cross-sections) are given for comparison. The errors shown are the statistical plus systematic uncertainties.

channel	SR_3^{SF}	VR_3^{SF}	CR_3^{SF}
Observed events	4	83	5745
Fitted bkg events	2.95 ± 0.99	87.26 ± 20.18	5744.80 ± 76.24
Fitted tZ events	0.00 ± 0.00	$0.01^{+0.01}_{-0.01}$	2.20 ± 2.19
Fitted Wt events	$0.00^{+0.04}_{-0.00}$	5.12 ± 2.18	281.74 ± 60.70
Fitted H events	$0.00^{+0.00}_{-0.00}$	$0.02^{+0.03}_{-0.02}$	4.10 ± 0.41
Fitted WW events	$0.00^{+0.06}_{-0.00}$	$0.17^{+0.27}_{-0.17}$	$14.72^{+28.72}_{-14.72}$
Fitted ZZ events	$0.00^{+0.01}_{-0.00}$	$0.00^{+0.04}_{-0.00}$	$2.96^{+3.63}_{-2.96}$
Fitted WZ events	$0.01^{+0.06}_{-0.01}$	$0.08^{+0.53}_{-0.08}$	$4.69^{+4.99}_{-4.69}$
Fitted $t\bar{t}W + t\bar{t}Z + t\bar{t}WW$ events	0.12 ± 0.05	1.03 ± 0.27	25.36 ± 5.68
Fitted DY events	0.00 ± 0.00	0.00 ± 0.00	4.28 ± 1.59
Fitted Z events	$0.72^{+0.78}_{-0.72}$	$2.56^{+2.68}_{-2.56}$	69.08 ± 40.96
Fitted $t\bar{t}$ events	2.08 ± 0.63	51.73 ± 9.57	3957.84 ± 175.79
Fitted $Fakes$ events	0.00 ± 0.00	26.55 ± 17.17	1377.82 ± 131.12
MC exp. SM events	3.85 ± 1.35	109.44 ± 25.80	7446.55 ± 723.55
MC exp. tZ events	0.00 ± 0.00	$0.01^{+0.01}_{-0.01}$	2.20 ± 2.20
MC exp. Wt events	$0.00^{+0.04}_{-0.00}$	5.12 ± 2.19	281.74 ± 61.15
MC exp. H events	$0.00^{+0.00}_{-0.00}$	$0.02^{+0.03}_{-0.02}$	4.10 ± 0.41
MC exp. WW events	$0.00^{+0.06}_{-0.00}$	$0.17^{+0.27}_{-0.17}$	$14.76^{+28.87}_{-14.76}$
MC exp. ZZ events	$0.00^{+0.01}_{-0.00}$	$0.00^{+0.04}_{-0.00}$	$2.96^{+3.65}_{-2.96}$
MC exp. WZ events	$0.01^{+0.06}_{-0.01}$	$0.08^{+0.53}_{-0.08}$	$4.69^{+5.03}_{-4.69}$
MC exp. $t\bar{t}W + t\bar{t}Z + t\bar{t}WW$ events	0.12 ± 0.05	1.03 ± 0.28	25.36 ± 5.72
MC exp. DY events	0.00 ± 0.00	0.00 ± 0.00	4.29 ± 1.60
MC exp. Z events	$0.72^{+0.78}_{-0.72}$	$2.56^{+2.69}_{-2.56}$	69.08 ± 41.23
MC exp. $t\bar{t}$ events	2.98 ± 1.07	73.92 ± 17.99	5659.54 ± 693.59
data-driven exp. $Fakes$ events	0.00 ± 0.00	26.55 ± 17.17	1377.83 ± 131.95

Table 7.17: Background fit results for the SR_4^{SF}, VR_4^{SF} and CR_4^{SF} regions, for an integrated luminosity of 20.3 fb^{-1}. Nominal MC expectations (normalised to MC cross-sections) are given for comparison. The errors shown are the statistical plus systematic uncertainties.

channel	SR_4^{SF}	VR_4^{SF}	CR_4^{SF}
Observed events	9	237	4035
Fitted bkg events	6.33 ± 1.57	260.75 ± 27.18	4034.85 ± 64.70
Fitted tZ events	$0.01^{+0.02}_{-0.01}$	$0.09^{+0.10}_{-0.09}$	$0.36^{+0.36}_{-0.36}$
Fitted Wt events	$0.08^{+0.13}_{-0.08}$	10.70 ± 4.55	243.24 ± 52.13
Fitted H events	0.03 ± 0.03	0.34 ± 0.08	4.09 ± 0.68
Fitted WW events	0.93 ± 0.52	9.40 ± 1.39	152.57 ± 61.16
Fitted ZZ events	0.83 ± 0.47	1.64 ± 0.54	3.23 ± 1.54
Fitted WZ events	0.74 ± 0.50	2.92 ± 0.70	16.75 ± 3.07
Fitted $t\bar{t}W + t\bar{t}Z + t\bar{t}WW$ events	0.32 ± 0.09	1.67 ± 0.40	9.27 ± 2.13
Fitted DY events	$0.00^{+0.53}_{-0.00}$	16.08 ± 4.13	49.51 ± 17.59
Fitted Z events	$0.11^{+0.23}_{-0.11}$	24.20 ± 13.12	288.88 ± 124.78
Fitted $t\bar{t}$ events	3.27 ± 1.03	193.69 ± 16.13	3266.96 ± 176.21
Fitted $Fakes$ events	0.00 ± 0.00	0.00 ± 0.00	0.00 ± 0.00
MC exp. SM events	6.00 ± 1.64	241.08 ± 36.77	3706.41 ± 414.05
MC exp. tZ events	$0.01^{+0.02}_{-0.01}$	$0.09^{+0.10}_{-0.09}$	$0.36^{+0.36}_{-0.36}$
MC exp. Wt events	$0.08^{+0.13}_{-0.08}$	10.67 ± 4.56	242.97 ± 52.45
MC exp. H events	0.03 ± 0.03	0.34 ± 0.09	4.08 ± 0.68
MC exp. WW events	0.92 ± 0.53	9.39 ± 1.39	152.18 ± 61.55
MC exp. ZZ events	0.83 ± 0.47	1.64 ± 0.54	3.23 ± 1.55
MC exp. WZ events	0.74 ± 0.50	2.92 ± 0.70	16.74 ± 3.09
MC exp. $t\bar{t}W + t\bar{t}Z + t\bar{t}WW$ events	0.32 ± 0.09	1.67 ± 0.40	9.27 ± 2.14
MC exp. DY events	$0.00^{+0.53}_{-0.00}$	16.07 ± 4.14	49.42 ± 17.69
MC exp. Z events	$0.11^{+0.23}_{-0.11}$	24.11 ± 13.20	289.37 ± 125.66
MC exp. $t\bar{t}$ events	2.95 ± 1.09	174.17 ± 27.69	2938.79 ± 362.75
data-driven exp. $Fakes$ events	0.00 ± 0.00	0.00 ± 0.00	0.00 ± 0.00

Table 7.18: Background fit results for the SR_5^{SF}, VR_5^{SF} and CR_5^{SF} regions, for an integrated luminosity of 20.3 fb^{-1}. Nominal MC expectations (normalised to MC cross-sections) are given for comparison. The errors shown are the statistical plus systematic uncertainties.

channel	SR_5^{SF}	VR_5^{SF}	CR_5^{SF}
Observed events	2	1909	14936
Fitted bkg events	5.50 ± 1.78	2056.37 ± 106.63	14935.96 ± 129.93
Fitted tZ events	$0.01^{+0.01}_{-0.01}$	$0.23^{+0.23}_{-0.23}$	1.77 ± 1.76
Fitted Wt events	$0.34^{+0.35}_{-0.34}$	112.97 ± 24.20	580.31 ± 123.44
Fitted H events	0.00 ± 0.00	1.61 ± 0.26	24.27 ± 2.14
Fitted WW events	0.24 ± 0.24	61.91 ± 24.50	304.03 ± 85.59
Fitted ZZ events	$0.19^{+0.21}_{-0.19}$	3.61 ± 1.64	4.68 ± 3.81
Fitted WZ events	$0.13^{+0.24}_{-0.13}$	10.28 ± 1.36	39.27 ± 4.80
Fitted $t\bar{t}W + t\bar{t}Z + t\bar{t}WW$ events	0.33 ± 0.10	6.32 ± 1.43	36.85 ± 8.28
Fitted DY events	$0.23^{+0.27}_{-0.23}$	35.53 ± 9.68	292.99 ± 70.71
Fitted Z events	$0.10^{+0.13}_{-0.10}$	80.72 ± 27.39	1275.39 ± 352.95
Fitted $t\bar{t}$ events	3.92 ± 1.63	1743.20 ± 105.44	12376.40 ± 474.61
Fitted $Fakes$ events	0.00 ± 0.00	0.00 ± 0.00	0.00 ± 0.00
MC exp. SM events	5.42 ± 1.92	2021.95 ± 244.83	14687.67 ± 1665.52
MC exp. tZ events	$0.01^{+0.01}_{-0.01}$	$0.23^{+0.23}_{-0.23}$	1.77 ± 1.76
MC exp. Wt events	$0.34^{+0.35}_{-0.34}$	112.96 ± 24.35	580.16 ± 124.26
MC exp. H events	0.00 ± 0.00	1.61 ± 0.26	24.26 ± 2.15
MC exp. WW events	0.24 ± 0.24	61.89 ± 24.66	303.91 ± 86.15
MC exp. ZZ events	$0.19^{+0.21}_{-0.19}$	3.60 ± 1.65	4.68 ± 3.84
MC exp. WZ events	$0.13^{+0.24}_{-0.13}$	10.27 ± 1.36	39.26 ± 4.83
MC exp. $t\bar{t}W + t\bar{t}Z + t\bar{t}WW$ events	0.33 ± 0.10	6.32 ± 1.44	36.84 ± 8.33
MC exp. DY events	$0.23^{+0.27}_{-0.23}$	35.53 ± 9.72	292.89 ± 71.13
MC exp. Z events	$0.10^{+0.13}_{-0.10}$	80.71 ± 27.56	1274.94 ± 355.40
MC exp. $t\bar{t}$ events	3.84 ± 1.77	1708.83 ± 231.42	12128.96 ± 1531.30
data-driven exp. $Fakes$ events	0.00 ± 0.00	0.00 ± 0.00	0.00 ± 0.00

CHAPTER 8

Interpretation of Experimental Results

As noted in the previous chapter, the agreement is good between the observed number of events and the predicted SM backgrounds. These experimental results in the signal region will be translated into exclusion limits using hypothesis tests. The statistical treatment for the analysis is based on the profile likelihood method implemented using HistFitter [100]. The next section describes the details of the interpretation of the data and the exclusion limits.

The exclusion fit mode in HistFitter tests the background+signal hypothesis. Both signal and control regions for the various expected backgrounds are used. In this configuration, VR are not configured, as consequent hypothesis tests do not distinguish between control and validation regions. The signal contribution in all the signal and control regions is taken into account as predicted by the signal model under study. The exclusion limits are set using the confidence limits (CLs) value, which represents the probability for the given observation to be compatible with the signal + background hypothesis and is used to test the exclusion of new physics hypothesis.

Two types of CLs values are considered: CLs_{exp} is obtained when the total fitted background is used as "data" in the signal regions, and provides an estimate of the expected sensitivity of the analysis; CLs_{obs} is obtained when the observed data is used in the signal regions. CLs values below 0.05 allow to exclude the given signal model under test at 95% confidence level. Therefore, one cannot exclude a signal model if

there is any set of auxiliary measurement values where the CLs value is greater than 5%.

Each of the SRs performs best in a specific model parameter region. In order to obtain the best combined exclusion limit, for each grid point a mapping is constructed by selecting the SR with the lowest CLs_{exp}. This is done without considering observed data in order to avoid any bias in the measurement. The mapping of signal points to SRs on the basis of the lowest CLs_{exp} is shown in figure 8.1 for DF and SF channels.

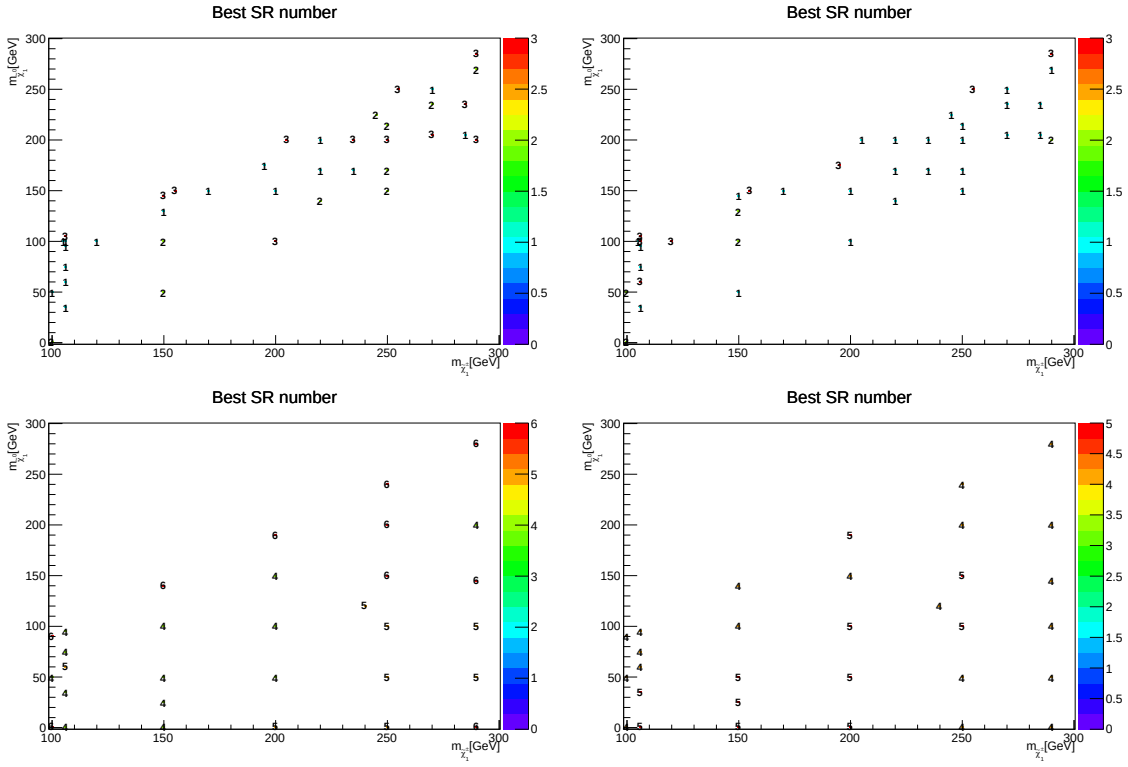

Figure 8.1: Index of the best expected SR per signal point over the grid chosen by HistFitter for MET trigger (top) and Lepton trigger (bottom): DF(left) and SF(right) channels. This mapping is used for the final exclusion limits.

Figure 8.1 shows the best expected SR which can be different from the one reported in figure 6.2 and 6.3 for some signal points over the grid. The difference can be due to the following effects:

- Due to the different background estimates. Since in figure 6.2 and 6.3 the background is fixed to the MC expected number of events. There is no correction applied from the fit.
- Presence of different systematics. Since the systematic error on background events in figure 6.2 and 6.3 is "arbitrarily", fixed at the reasonable assumption of 50%. In figure 8.1, all the systematics are properly taken into account on signal and background.
- The different criterion to select the best SR. HistFitter computes the limits on the basis of CLs, while figure 6.2 and 6.3 relies on a simplified significance definition.

Then, for each signal grid point, taking into account the best SR assigned to it, the number of events observed in SF and DF channels are compared with the SM background and to the SM background plus signal expectations (hypothesis test) and contour exclusion plots are produced.

In the context of the analysis, the likelihood function can be written as a product of Poisson distribution functions for SR(s) or CR(s) and accompanied by additional systematic uncertainty distributions N_{syst}:

$$\mathcal{L}(n, \theta^0 | \mu_{sig}, b, \theta) = \prod_{i \in SR} P(n_i | \lambda_i(\mu_{sig}, b, \theta)) \times \prod_{j \in CR} P(n_j | \lambda_j(\mu_{sig}, b, \theta)) \times N_{syst}(\theta^0, \theta). \tag{8.1}$$

The two factors in equation 8.1 reflect the Poisson measurements of n_i and n_j, which are the number of observed events in signal region and control region i and j, while λ_i and λ_j are the Poisson expectation values. The expectation values depend on the

background normalization factors b, the nuisance parameters θ modelling the systematic uncertainties as well as the signal strength μ_{sig} , with $\mu_{sig} = 1$ corresponding to the nominal signal under consideration and $\mu_{sig} = 0$ describing a background-only likelihood. Systematic uncertainties are included using the probability density function $N_{syst}(\theta^0, \theta)$, where θ_0 are the central values of the auxiliary measurements around which θ can be varied.

Uncertainties are properly taken into account in this calculation. The signal prediction uncertainties include the detector response uncertainties discussed, the luminosity, and finite MC statistical uncertainties. In the HistFitter, trees with nominal values and the corresponding variations due to systematic effects are given in input to the fit for each background and signal sample. The signal cross section uncertainty is not included, but limits are quoted for the nominal cross section and for the cross section changed by one standard deviation of the theoretical error. In order to estimate the cross section uncertainty, an envelope of cross section predictions is defined using the 68% CL ranges of CTEQ6.6 [106] (including the α_S uncertainty) and MRSTW2008 NNLO [107] PDF sets, together with independent variations of the factorization and renormalization scales by factors of two and of one half. The nominal cross section value is taken to be the midpoint of the envelope and the uncertainty assigned is half the full width of the envelope, closely following the PDF4LHC recommendations.

The uncertainties, both on signal and backgrounds, are modeled with a convolution of Gaussians. The correlation between signal and background in the detector uncertainties is described, while other uncertainties which act independently on the signal and on the background are referred to their specific samples.

The signal model independent limits at 95% of CL are derived by the product $\sigma \times \epsilon \times \mathcal{A}$, where σ is the non-SM cross section, ϵ the selection efficiency, and $\mathcal{A}$ the

acceptance of kinematic cuts. All signal related uncertainties are removed: signal theory uncertainties (e.g. on the signal cross section) and all experimental uncertainties on the signal (e.g. jet energy scale, luminosity, etc.). For the background the full list of uncertainties is taken into account. For each signal region, various numbers of signal events are tested using both the expected background (for the expected limit) and the observed number of events (for the observed limit). The number of signal events which corresponds to a CLs value just below 5% gives the upper limit. As an example, figure 8.2 shows the p-values, respectively for SR_1^{DF}, SR_1^{SF}, SR_5^{DF} and SR_4^{SF}, computed in a signal model independent way using the distributions for the only background hypothesis (Standard Model) and for signal plus background hypothesis as a function of the number of signal events. The CL_{s+b}, CL_b, and their ratio CL_s are shown for comparison together with the expected sensitivity (p-value corresponding to the CL_{s+b} median).

Then the upper limits on $\epsilon\sigma_{obs}$ are derived following the above procedure with the modification that the luminosity and its uncertainty are taken into account. The measured upper limits on the number of signal events are divided by the integrated luminosity, thus obtaining the upper limits on $\epsilon\sigma_{obs}$. In table 8.1 are reported (as obtained with 20000 toy simulations.): the 95% CL upper limits on the visible cross section ($\langle\epsilon\sigma\rangle^{95}_{\rm obs}$) and on the number of signal events ($S^{95}_{\rm obs}$); the 95% CL upper limit on the number of signal events ($S^{95}_{\rm exp}$), given the expected number (and $\pm1\sigma$ excursions on the expectation) of background events. The last two columns in table 8.1 indicate the CL_B value, i.e. the confidence level observed for the background-only hypothesis, and the discovery p-value ($p(s=0)$).

The exclusion limits at 95% CL in the $m(\tilde{\chi}_1^{\pm}) - m(\tilde{\chi}_1^0)$ plane for a 300 GeV mass stop are shown in figure 8.3 and in figure 8.4, as obtained by using the best signal

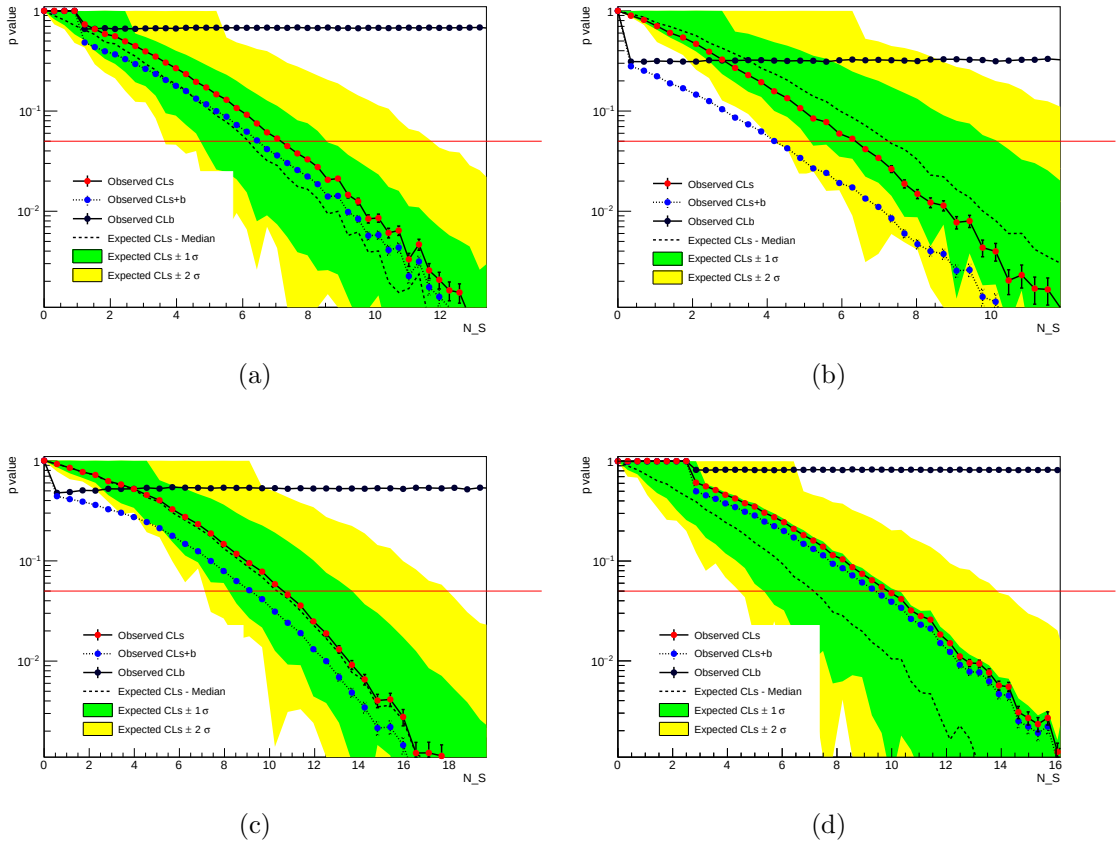

Figure 8.2: CL_{s+b}, CL_b, and CL_s p-values as a function of the number of signal events for SR_1^{DF} (a), SR_1^{SF} (b), SR_5^{DF} (c) and SR_4^{SF} (d).

regions for DF (top left) and SF (top right) and for their combination (bottom), for MET trigger and Lepton trigger respectively.

Figure 8.3 and 8.4 show the following contours:

- thick solid red line: observed limit in which all uncertainties are included in the fit as nuisance parameters, with the exception of the theoretical signal uncertainties (PDF, scales);
- long-dashed dark line: expected limit in which all uncertainties are included in the fit as nuisance parameters, with the exception of the theoretical signal uncertainties (PDF, scales);

Table 8.1: Left to right: observed events, total expected background events, 95% CL upper limits on the visible cross section ($\langle\epsilon\sigma\rangle^{95}_{\rm obs}$) and on the number of signal events ($S^{95}_{\rm obs}$). The fifth column ($S^{95}_{\rm exp}$) shows the 95% CL upper limit on the number of signal events, given the expected number (and $\pm1\sigma$ excursions on the expectation) of background events. The last two columns indicate the CL_B value, i.e. the confidence level observed for the background-only hypothesis, and the discovery p-value ($p(s = 0)$).

Signal channel	N_{obs}	N_{exp}	$\langle\epsilon\sigma\rangle^{95}_{\rm obs}$[fb]	$S^{95}_{\rm obs}$	$S^{95}_{\rm exp}$	CL_B	$p(s=0)$
$\mathrm{SR}^{\mathrm{DF}}_1$	5	4.07 ± 1.45	0.36	7.2	$6.2^{+2.4}_{-1.4}$	0.68	0.34
$\mathrm{SR}^{\mathrm{DF}}_2$	1	2.06 ± 1.53	0.20	3.9	$4.3^{+1.6}_{-0.5}$	0.40	0.78
$\mathrm{SR}^{\mathrm{DF}}_3$	1	1.22 ± 0.88	0.19	3.9	$3.9^{+1.6}_{-0.3}$	0.50	0.80
$\mathrm{SR}^{\mathrm{DF}}_4$	3	4.09 ± 1.07	0.24	4.8	$5.5^{+2.4}_{-1.3}$	0.35	0.73
$\mathrm{SR}^{\mathrm{DF}}_5$	8	8.26 ± 4.44	0.52	10.6	$10.3^{+3.3}_{-2.1}$	0.53	0.97
$\mathrm{SR}^{\mathrm{DF}}_6$	4	3.34 ± 1.79	0.35	7.1	$6.2^{+2.3}_{-1.4}$	0.65	0.40
$\mathrm{SR}^{\mathrm{SF}}_1$	5	7.25 ± 2.49	0.32	6.4	$7.2^{+2.9}_{-1.7}$	0.33	0.79
$\mathrm{SR}^{\mathrm{SF}}_2$	10	6.16 ± 1.48	0.55	11.1	$7.1^{+3.0}_{-1.8}$	0.90	0.10
$\mathrm{SR}^{\mathrm{SF}}_3$	4	2.95 ± 0.99	0.32	6.4	$5.3^{+2.1}_{-1.2}$	0.72	0.29
$\mathrm{SR}^{\mathrm{SF}}_4$	9	6.33 ± 1.57	0.49	9.9	$7.1^{+3.1}_{-1.8}$	0.82	0.18
$\mathrm{SR}^{\mathrm{SF}}_5$	2	5.50 ± 1.78	0.20	4.1	$5.9^{+2.4}_{-1.6}$	0.12	0.72

and the following uncertainty bands:

- thin dark-red dotted lines: $\pm1\sigma$ lines around observed limit. To produce them the limit calculation (a) is re-run increasing or decreasing the signal cross section by the theoretical signal uncertainties (PDF, scales).
- yellow band: $\pm1\sigma$ band around expected limit. The band contours are the $\pm1\sigma$ results of the fit (b).

The numbers shown in the plots are the observed CLs values: the signal points over the grid for which these values are > 0.05 cannot be excluded and stay outside the thick solid red line.

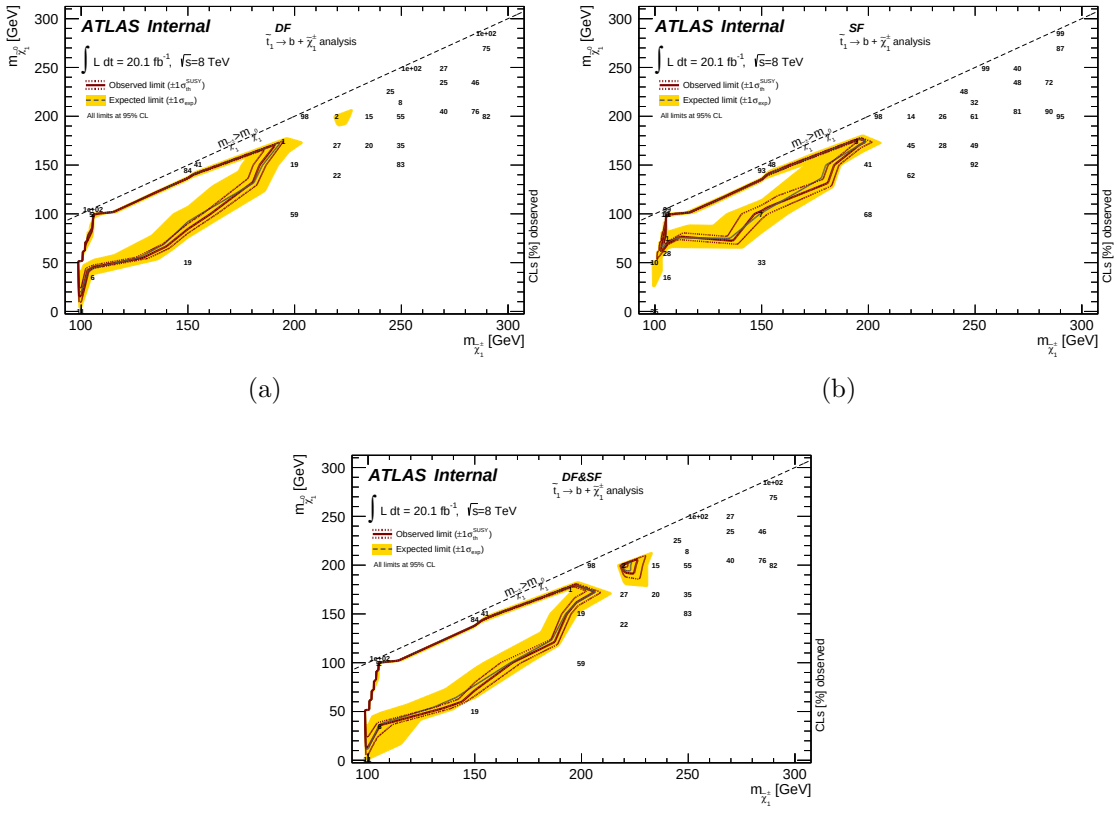

(a) (b)

(c)

Figure 8.3: Exclusion limits at 95% CL in the $m(\tilde{\chi}_1^\pm) - m(\tilde{\chi}_1^0)$ plane for a 300 GeV mass stop for DF channel (top left), SF channel (top right) and their combination (bottom) as obtained from MET triggered events. The numbers shown in the plots are the observed CLs values.

The combination of DF and SF channels results in an improvement over most part of the plane with respect to the limits obtained with DF and SF channels separately. As shown in figure 8.3 and in figure 8.4, indeed, for a given point in the plane $m(\tilde{\chi}_1^\pm) - m(\tilde{\chi}_1^0)$ the CLs value improves with respect to the case of DF channel after combining together DF and SF, especially in the region close to the "diagonal", thus resulting in a final combined exclusion contour closer to this line.

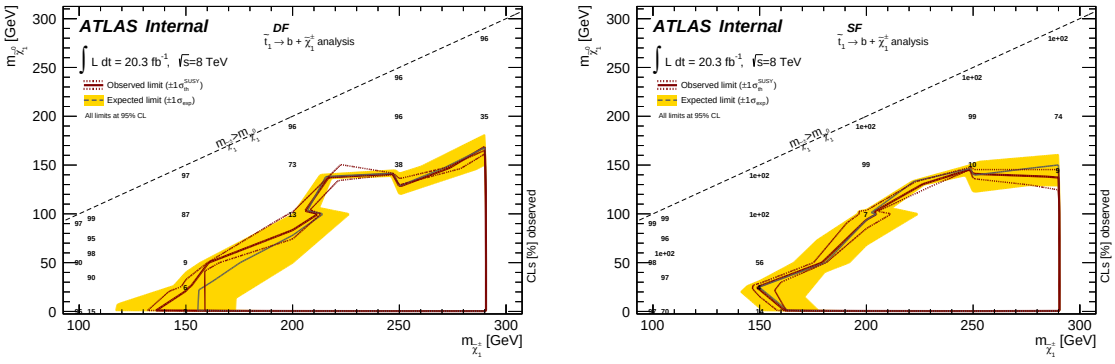

(a) (b)

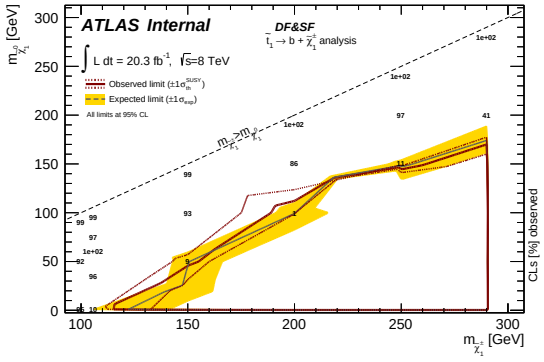

(c)

Figure 8.4: Exclusion limits at 95% CL in the $m(\tilde{\chi}_1^{\pm}) - m(\tilde{\chi}_1^0)$ plane for a 300 GeV mass stop for DF channel (top left), SF channel (top right) and their combination (bottom) as obtained from Lepton triggered events. The numbers shown in the plots are the observed CLs values.

The final exclusion limits at 95% CL in the $m(\tilde{\chi}_1^{\pm}) - m(\tilde{\chi}_1^0)$ plane for a 300 GeV mass stop, obtained from the combination of the MET trigger based and the Lepton trigger based analysis after using the best signal regions, are shown in figure 8.5.

8.1 Summary and Conclusions

A multivariate analysis was performed [108], searching for evidence of pair production of the top quark's heavy supersymmetric partner, each one later decaying into a b-jet and a $\tilde{\chi}_1^{\pm}$. Events with two oppositely charged leptons (electrons or

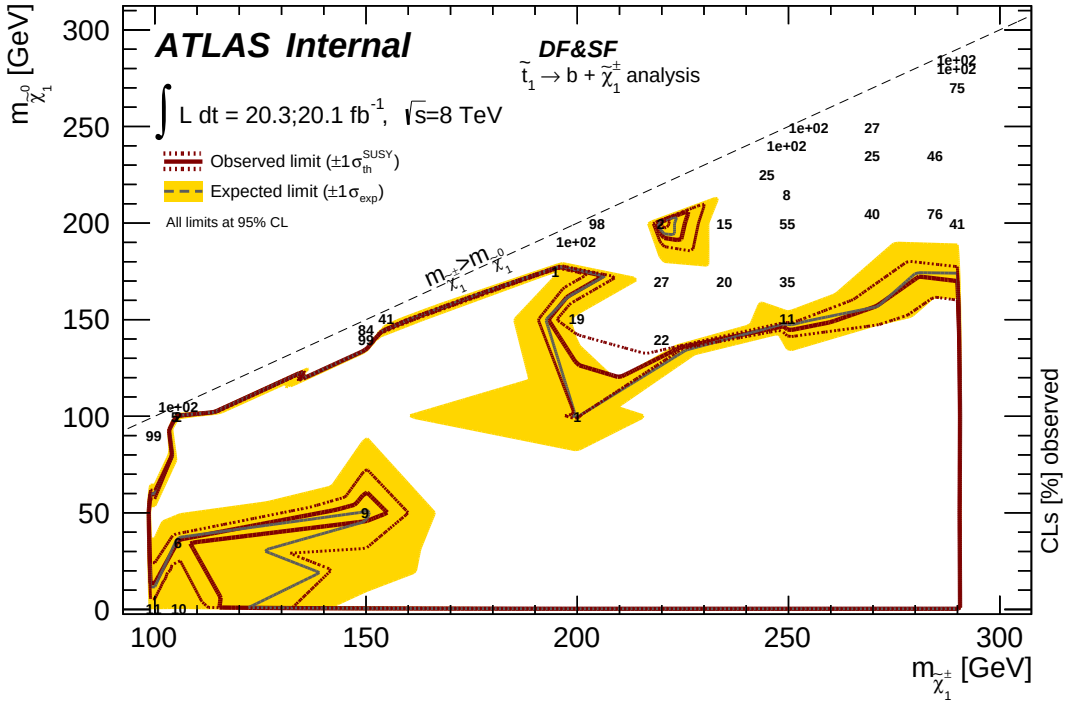

Figure 8.5: Exclusion limits at 95% CL in the $m(\tilde{\chi}_1^{\pm}) - m(\tilde{\chi}_1^0)$ plane for a 300 GeV mass stop obtained from the combination of the MET trigger based and the Lepton trigger based analyses. The numbers shown in the plots are the observed CLs values.

muons) were analyzed and the experimental data was compared to SM predictions in a variety of SRs. Results are in agreement with SM predictions across all SRs. The observations in the various SRs are used to produce 95% CL upper limits on $\tilde{t_1}$pair production assuming the decay $\tilde{t_1} \to b + \chi_1^{\pm}$, at 100% BR.

The analysis was performed with the ROOT integrated TMVA toolkit, using the BDTG method. All the proton proton data collected in 2012 by ATLAS at a center of mass energy of $\sqrt{s} = 8$ TeV were used for these results, corresponding to an integrated luminosity of 20.3 fb^1 for Lepton trigger and 20.1 fb^1 for MET trigger. No sign of a significant excess of events above those predicted by the SM was observed. Consequently, for a 300 GeV top squark decaying to a b-quark and

a chargino, exclusion limits were set for a range of neutralino masses as shown in figure 8.5.

BIBLIOGRAPHY

[1] Hideki Okawa, on behalf of the ATLAS Collaboration, "Interpretations of SUSY Searches in ATLAS with Simplified Models," in *Proceedings of the DPF-2011 Conference, Providence, RI*, August 8-13, 2011.

[2] J. Haffner, "The CERN accelerator complex., OPEN-PHO-ACCEL-2013-056-1," 2013. [Online]. Available: https://cds.cern.ch/record/1621894

[3] ATLAS Collaboration, G. Aad et al., "The ATLAS Experiment at the CERN Large Hadron Collider," *JINST 3*, vol. S08003, 2008.

[4] J. Goodson. [Online]. Available: http://www.jetgoodson.com/images/thesisImages/magnetSystems.png

[5] "ATLAS level-1 trigger: Technical Design Report ATLAS. CERN, Geneva," 1998.

[6] T. Gleisberg et al., "Event generation with SHERPA 1.1," *JHEP 02*, vol. 02, 2009. [Online]. Available: arXiv:0811.4622

[7] Peter W. Higgs, "Broken symmetries and the masses of gauge bosons," *Physical Reviews Letters*, vol. 13, pp. 507–508, 1964.

[8] F. Englert, R. Brout, "Broken symmetry and the mass of gauge vector mesons," *Physical Review Letters*, vol. 13, pp. 321–323, 1964.

[9] C. R. Hagen, G. S. Guralnik, T. W. B. Kibble, "Global conservation laws and massless particles," *Physical Review Letters*, vol. 13, pp. 385–587, 1964.

[10] Gerald S. Guarlnik, "The history of the guralnik, hagen and kibble development of the theory of spontaneous symmetry breaking and gauge particles," *International Journal of Modern Physics*, vol. A24, pp. 2601–2627, 2009.

[11] ATLAS Collaboration, G. Aad et al., "Observation of a new particle in the search for the standard model higgs boson with the atlas detector at the lhc," *Phys.Lett.*, vol. B716, pp. 1–29, 2012.

[12] CMS Collaboration and S. Chatrchyan et al., "Observation of a new boson at a mass of 125 gev with the cms experiment at the lhc," *Phys.Lett.*, vol. B716, pp. 30–61, 2012.

[13] ATLAS Collaboration, G. Aad et al., "Evidence for the spin-0 nature of the higgs boson using atlas data," *Phys.Lett.*, vol. B726(1-3), pp. 120–144, 2013.

[14] ATLAS Collaboration, "Measurements of Higgs boson production and couplings in diboson final states with the ATLAS detector at the LHC," *Phys.Lett.*, vol. B726(1-3), pp. 88–119, 2013.

[15] N. Arkani-Hamed, S. Dimopoulos, and G. Dvali, "The hierarchy problem and new dimensions at a millimeter," *Phys.Lett.*, vol. B429, pp. 263–272, 1998.

[16] Y. Golfand and E. Likhtman, "Extension of the Algebra of Poincare Group Generators and Violation of p Invariance," *JETP Lett.*, vol. 13, pp. 323–326, 1971.

[17] A. Neveu and J. H. Schwarz, "Factorizable dual model of pions," *Nucl. Phys.*, vol. B31, pp. 86–112, 1971.

[18] P. Ramond, "Dual Theory for Free Fermions," *Phys. Rev.*, vol. D3, pp. 2415–2418, 1971.

[19] A. Neveu and J. H. Schwarz, "Quark Model of Dual Pions," *Phys. Rev.*, vol. D4, pp. 1109–1111, 1971.

[20] J. Wess and B. Zumino, "Supergauge Transformations in Four-Dimensions," *Nucl. Phys.*, vol. B70, pp. 39–50, 1974.

[21] D. Volkov and V. Akulov, "Is the Neutrino a Goldstone Particle?" *Phys. Lett.*, vol. B46, pp. 109–110, 1973.

[22] J. Wess and B. Zumino, "A Lagrangian Model Invariant Under Supergauge Transformations," *Phys. Lett.*, vol. B49, pp. 52–54, 1974.

[23] Ugo Amaldi, Wim de Boer and Hermann Furstenau , "Comparison of grand unified theories with electroweak and strong coupling constants measured at LEP," *Phys. Lett.*, vol. B260, pp. 447–455, 1991.

[24] H. Nishino et al., "Search for Proton Decay via $p \to e^+\pi^0$ and $p \to \mu^+\pi^0$ in a Large Water Cherenkov Detector," *Phys.Rev.Lett.*, vol. 102, p. 141801, 2009.

[25] R. Haag, J. T. Lopuszanski, and M. Sohnius, "All possible generators of supersymmetries of the S-matrix," *Nuclear Physics*, vol. B88, pp. 257–274, 1975.

[26] P. Fayet, "Supersymmetry and Weak, Electromagnetic and Strong Interactions," *Phys.Lett.*, vol. B64, p. 159, 1976.

[27] G. R. Farrar and P. Fayet, "Phenomenology of the Production, Decay, and Detection of New Hadronic States Associated with Supersymmetry," *Phys.Lett.*, vol. B76, pp. 575–579, 1978.

[28] P. Fayet, "Relations Between the Masses of the Superpartners of Leptons and Quarks, the Goldstino Couplings and the Neutral Currents," *Phys.Lett.*, vol. B84, p. 416, 1979.

[29] S. Dimopoulos and H. Georgi, "Softly Broken Supersymmetry and SU(5)," *Nucl.Phys.*, vol. B193, p. 150, 1981.

[30] G. R. Farrar and P. Fayet, "Phenomenology of the production, decay, and detection of new hadronic states associated with supersymmetry," *Phys.Lett.*, vol. B76, pp. 575–579, 1978.

[31] Ali H. Chamseddine, Richard L. Arnowitt and Pran Nath, "Locally Supersymmetric Grand Unification," *Phys.Rev.Lett.*, vol. 49, p. 970, 1982.

[32] Riccardo Barbieri, S. Ferrara and Carlos A., "Gauge Models with Spontaneously Broken Local Supersymmetry," *Phys. Lett.*, vol. B119, p. 343, 1982.

[33] Luis E. Ibanez., "Locally supersymmetric SU(5) Grand Unification," *Phys. Lett.*, vol. B118, p. 73, 1982.

[34] Lawrence J. Hall, Joseph D. Lykken and Steven Weinberg, "Supergravity as the messenger of supersymmetry breaking," *Phys.Rev.*, vol. D27, pp. 2359–2378, 1983.

[35] Nobuyoshi Ohta., "Grand Unified Theories based on local supersymmetry," *Prog.Theor.Phys.*, vol. 70, p. 542, 1983.

[36] Gordon L. Kane, Christopher F. Kolda, Leszek Roszkowski and James D. Wells, "Study of constrained minimal supersymmetry," *Phys.Rev.*, vol. D49, pp. 6173–6210, 1994.

[37] Lisa Randall and Raman Sundrum, "Out of this world supersymmetry breaking," *Nucl.Phys.*, vol. B557, p. 79118, 1999. [Online]. Available: arXiv:hep-th/9810155

[38] Gian F. Giudice, Markus A. Luty, Hitoshi Murayama and Riccardo Rattazzi, "Gaugino mass without singlets," *JHEP*, vol. 9812, p. 27, 1998. [Online]. Available: arXiv:hep-ph/9810442

[39] LHC New Physics Working Group Collaboration, D. Alves et al., "Simplified Models for LHC New Physics Searches," *J.Phys.*, vol. G39, p. 105005, 2012. [Online]. Available: arXiv:1105.2838

[40] J. Alwall, P. Schuster, and N. Toro, "Simplified Models for a First Characterization of New Physics at the LHC," *Phys. Rev.*, vol. D79, 2009. [Online]. Available: arXiv:hep-ph/0810.3921

[41] L. Evans and P. Bryant, "LHC Machine," *JINST 3*, vol. S08001, 2008.

[42] CMS Collaboration, S. Chatrchyan et al., "The CMS experiment at the CERN LHC," *JINST 3*, vol. S08004, 2008.

[43] LHCb Collaboration, J. Alves, A. Augusto et al., "The LHCb Detector at the LHC," *JINST 3*, vol. S08005, 2008.

[44] ALICE Collaboration, K. Aamodt et al., "The ALICE experiment at the CERN LHC," *JINST 3*, vol. S08002, 2008.

[45] O.S. Bruning et al., "The LHC Main Ring," *LHC Design Report*, vol. 1, 2004.

[46] B.R. Webber, "A QCD Model for Jet Fragmentation Including Soft Gluon Interference," *Nucl.Phys.*, vol. B238, 1984.

[47] B. Andersson et al, "Parton fragmentation and string dynamics," *Nucl.Phys.*, vol. 97, 1983.

[48] T. Sjostrand, S. Mrenna, and P. Skands, "PYTHIA 6.4 physics and manual," *JHEP*, vol. 0605, p. 026, 2006.

[49] T. Sjostrand, S. Mrenna, P. Skands, "A Brief Introduction to PYTHIA 8.1." *Comput. Phys. Comm.*, vol. 178, p. 852, 2008. [Online]. Available: arXiv:0710.3820

[50] J. Alwall, M. Herquet, F. Maltoni, O. Mattelaer et al., "MadGraph 5: Going Beyond," *JHEP*, vol. 1106, p. 128, 2011. [Online]. Available: arXiv:1106.0522

[51] S. Frixione, P. Nason, and C. Oleari, "Matching NLO QCD computations with parton shower simulations: the POWHEG method," *JHEP*, vol. 11, p. 070, 2007. [Online]. Available: arXiv:0709.2092

[52] S. Alioli, P. Nason, C. Oleari, and E. Re, "A general framework for implementing NLO calculations in shower Monte Carlo programs: the POWHEG BOX," *JHEP*, vol. 06, p. 043, 2010. [Online]. Available: arXiv:1002.2581

[53] G. Corcella et al., "HERWIG 6: An event generator for hadron emission reactions with interfering gluons (including supersymmetric processes)," *JHEP*, vol. 01, p. 010, 2001.

[54] J. Butterworth, J. R. Forshaw, and M. Seymour, "Multiparton interactions in photoproduction at HERA," *Z.Phys.*, vol. C72, pp. 637–646, 1996.

[55] M. Mangano et al., "ALPGEN, a generator for hard multiparton processes in hadronic collisions," *JHEP*, vol. 07, p. 001, 2003.

[56] S. Frixione and B. R. Webber, "The MC@NLO 3.2 Event Generator," *Phys.Rept.*, vol. 97, 1983. [Online]. Available: arXiv:hep-ph/0601192

[57] T. Gleisberg et al., "Event generation with SHERPA 1.1," *JHEP*, vol. 0902, 2009. [Online]. Available: arXiv:0811.4622

[58] GEANT4 Collaboration, S. Agostinelli et al., "GEANT4: A simulation toolkit," *Nucl. Instrum. Meth.*, vol. A506, pp. 250–303, 2003.

[59] S.Darmora and G. Usai, "Cesium Calibration of the Intermediate Tile Calorimeter," *ATL-TILECAL-INT-2014-004*, 2014. [Online]. Available: http://cds.cern.ch/record/1697131

[60] ATLAS/Tile Calorimeter Collaboration, *Tile Calorimeter-Technical Design Report CERN/LHCC*, pp. 96–42, 1996.

[61] Medina C. et al., "Inter-calibration of the Intermediate Tile Calorimeter using 2009 cosmic rays data," *ATL-COM-TILECAL-2012-028*, 2011.

[62] R. Barbieri and G. Giudice, "Upper Bounds on Supersymmetric Particle Masses," *Nucl. Phys.*, vol. B306, p. 63, 1988.

[63] S. Weinberg, "Implications of dynamical symmetry breaking," *Phys. Rev.*, vol. D13, pp. 974–996, 1976.

[64] E. Gildener, "Gauge symmetry hierarchies," *Phys. Rev.*, vol. D14, p. 1667, 1976.

[65] S. Weinberg, "Implications of dynamical symmetry breaking: An addendum," *Phys. Rev.*, vol. D19, pp. 1227–1280, 1979.

[66] L. Susskind, "Dynamics of spontaneous symmetry breaking in the weinberg-salam theory," *Phys. Rev.*, vol. D20, pp. 2619–2625, 1979.

[67] CDF Collaboration, "Search for scalar top quark top production in pp collisions at $\sqrt{s} = 1.96$ TeV," *JHEP*, vol. 10, p. 158, 2012.

[68] ATLAS Collaboration, "Search for direct top squark pair production in final states with one isolated lepton, jets, and missing transverse momentum in $\sqrt{s}$ = 8 tev pp collisions using $21fb^{-1}$ of atlas data," *ATLAS-CONF-2013-037*. [Online]. Available: https://cdsweb.cern.ch/record/1532431

[69] ATLAS Collaboration, G. Aad et al., "Search for direct stop production in events with missing transverse momentum and two b-jets in $\sqrt{s}$ = 8 tev pp collisions using 21 fb^1 of atlas data," *ATLAS-CONF-2012-171*. [Online]. Available: https://cdsweb.cern.ch/record/1503233

[70] CMS Collaboration, "Search for light stop RPV supersymmetry with three or more leptons and b-tags," *CMS-PAS-SUS-13-003*. [Online]. Available: https://cdsweb.cern.ch/record/1525539

[71] CMS Collaboration and S. Chatrchyan et al., "Search for direct top squark pair production in events with a single isolated lepton, jets and missing transverse energy at $\sqrt{s}$ = 8 tev," *CMS-PAS-SUS-12-023*. [Online]. Available: https://cdsweb.cern.ch/record/1494074

[72] CMS Collaboration, "Scalar top quark search with jets and missing momentum in pp collisions at $\sqrt{s}$ = 7 tev," *CMS-PAS-SUS-11-030*. [Online]. Available: https://cdsweb.cern.ch/record/1494575

[73] W. Lukas, "Fast Simulation for ATLAS: Atlfast-II and ISF," *Journal of Physics: Conference Series 396*, vol. 2, 2012.

[74] J. Alwall, M. Herquet, F. Maltoni, O. Mattelaer, and T. Stelzer, "MadGraph 5 : Going Beyond," *JHEP*, vol. 06, p. 128, 2011. [Online]. Available: arXiv:1106.522

[75] T. Sjostrand, S. Mrenna, and P. Z. Skands, "PYTHIA 6.4 Physics and Manual," *JHEP*, vol. 05, 2006.

[76] P. M. Nadolsky et al., "Implications of CTEQ global analysis for collider observation," *Phys. Rev.*, vol. D78, 2008.

[77] P. Skands et al., "SUSY Les Houches Accord: Interfacing SUSY Spectrum Calculators, Decay Packages, and Event Generators," *JHEP*. [Online]. Available: http://arxiv.org/abs/hep-ph/0311123

[78] S. Frixione and B. R. Webber, "Matching NLO QCD computations and parton shower simulations," *JHEP*, vol. 06, p. 029, 2002.

[79] S. Frixione, E. Laenen, P. Motylinski, and B. R. Webber, "Single-top production in MC@NLO," *JHEP*, vol. 03, p. 092, 2006.

[80] M. Cacciari, G. P. Salam, and G. Soyez, "The anti-kt jet clustering algorithm," *JHEP*, vol. 04, p. 063, 2008. [Online]. Available: arXiv:0802.1189

[81] ATLAS collaboration, "Commissioning of the ATLAS high-performance b-tagging algorithms in the 7 TeV collision data," *ATLAS-CONF-2011-102*, 2011. [Online]. Available: http://cdsweb.cern.ch/record/1369219

[82] ATLAS collaboration, G. Aad et al., "Electron performance measurements with the ATLAS detector using the 2010 LHC proton-proton collision data," *Eur. Phys. J.*, vol. C72, p. 1909, 2012. [Online]. Available: arXiv:1110.3174

[83] ATLAS collaboration, "Muon reconstruction efficiency in reprocessed 2010 LHC proton-proton collision data recorded with the ATLAS detector," *ATLAS-CONF-2011-063*. [Online]. Available: https://cdsweb.cern.ch/record/1345743/

[84] ATLAS collaboration, G. Aad et al., "Performance of Missing Transverse Momentum Reconstruction in Proton-Proton Collisions at 7 TeV with ATLAS," *Eur. Phys. J.*, vol. C72, p. 1844, 2012. [Online]. Available: arXiv:1108.5602

[85] ATLAS collaboration. [Online]. Available: https://twiki.cern.ch/twiki/bin/viewauth/Atlas/TileTripReader

[86] A. collaboration. [Online]. Available: https://twiki.cern.ch/twiki/bin/viewauth/Atlas/TileOverflowAnalysis#Problematic_events

[87] ATLAS collaboration, G. Aad et al., "ATLAS Collaboration, Selection of jets produced in proton-proton collisions with the ATLAS detector using 2011 data," *ATLAS-CONF-2012-020*, 2011.

[88] A. J. Barr, E. Duchovni, M. J. Flowerdew, M. Hodgkinson, T. J. Khoo, I. Roth, A. Sfyrla, F. Siegert, K. Suruliz, A. Tua, and C. J. S. Young , "Search for squarks and gluinos in multi-jet final state with the ATLAS experiment in $\sqrt{s}$=7TeV proton-proton collisions: Supporting Documentation," *Tech. Rep. ATL-COM-PHYS-2011-984*, 2011.

[89] A. Hoecker, P. Speckmayer, J. Stelzer, J. Therhaag, E. von Toerne, and H. Voss, "TMVA 4 Toolkit for Multivariate Data Analysis with ROOT," *Users Guide, CERN-OPEN-2007-007*, 2009. [Online]. Available: arXiv:physics/0703039

[90] B. P. Roe, H.-J. Yang, J. Zhu, Y. Liu, I. Stancu, et al. , "Boosted decision trees, an alternative to artificial neural networks," *Nucl.Instrum.Meth.*, vol. A543, pp. 577–584, 2005.

[91] Chris Lester, David Summers, "Measuring masses of semi-invisibly decaying particles pair produced at hadron colliders," *Phys.Lett.*, vol. B463, pp. 99–103, 1999. [Online]. Available: http://arxiv.org/abs/hep-ph/9906349

[92] Alan Barr, Christopher Lester, Phil Stephens, "A variable for measuring masses at hadron colliders when missing energy is expected; mT2: the truth behind the glamour," *J.Phys*, vol. G29, pp. 2343–2363, 2003. [Online]. Available: http://arxiv.org/abs/hep-ph/0304226

[93] W. S. Cho, K. Choi, Y. G. Kim, and C. B. Park, "Measuring superparticle masses at hadron collider using the transverse mass kink," *JHEP*, vol. 02, p. 035, 2008. [Online]. Available: arXiv:0711.4526

[94] M. Burns, K. Kong, K. T. Matchev, and M. Park, "Using Subsystem mT2 for Complete Mass Determinations in Decay Chains with Missing Energy at Hadron Colliders," *JHEP*, vol. 03, p. 143, 2009. [Online]. Available: arXiv:0810.5576

[95] G. A. e. a. ATLAS collaboration, "Measurement of the $W \to \ell\nu$ and $Z/\gamma^* \to \ell\ell$ production cross sections in proton-proton collisions at $\sqrt{s} = 7$ TeV with the ATLAS detector," *JHEP*, vol. 1012, p. 060, 2010.

[96] S. Frixione and B. Webber, "Matching NLO QCD computations and parton shower simulations," *JHEP*, vol. 0206, p. 029, 2002.

[97] T. Binoth, M. Ciccolini, N. Kauer, and M. Kramer, "Gluon-induced W-boson pair production at the LHC," *JHEP*, vol. 0612, p. 046, 2006.

[98] A. Collaboration, "Preliminary Luminosity Determination in pp Collisions at $\sqrt{s} = 8$ TeV using the ATLAS Detector in 2012," *Tech. Rep. ATL-COM-LUM-2012-013*, 2013.

[99] G. A. e. a. ATLAS collaboration, "Improved luminosity determination in pp collisions at $\sqrt{s)} = 7$ TeV using the ATLAS detector at the LHC," *Eur. Phys. J*, vol. C73, 2013.

[100] ATLAS collaboration. [Online]. Available: http://twiki.cern.ch/twiki/bin/viewauth/AtlasProtected/SusyFitter

[101] ROOT Collaboration Collaboration, K. Cranmer, G. Lewis, L. Moneta, A. Shibata, and W. Verkerke, "HistFactory: A tool for creating statistical models for use with RooFit and RooStats," *Tech. Rep. CERN-OPEN-2012-016*, 2012. [Online]. Available: https://cdsweb.cern.ch/record/1456844

[102] G. A. e. a. ATLAS Collaboration, "Measurement of the total zz production cross section in proton-proton collisions at $\sqrt{s} = 8$ tev in 20 fb^1 with the atlas detector," *ATLAS-CONF-2013-020*. [Online]. Available: https://cdsweb.cern.ch/record/1525555

[103] A. Collaboration, "A measurement of wz production in proton-proton collisions at $\sqrt{s} = 8$ tev with the atlas detector," *ATLAS-CONF-2013-021*. [Online]. Available: https://cdsweb.cern.ch/record/1525557

[104] ATLAS collaboration, G. Aad et al., "Measurement of the top quark-pair production cross section with ATLAS in pp collisions at $\sqrt{s} = 7$ TeV," *Eur. Phys. J.*, vol. C71, p. 1577, 2011. [Online]. Available: arXiv:1012.1792

[105] G. Cowan, "Error analysis for effciency," *tech. rep.*, 2008. [Online]. Available: http://www.pp.rhul.ac.uk/~cowan/stat/notes/efferr.pdf

[106] E. Pavel and M. Nadolsky, "Implications of CTEQ global analysis for collider observables," *Phys. Rev.*, vol. D78, 2008.

[107] A.D. Martin, W.J. Stirling, R.S. Thorne, G. Watt, "Parton distributions for the LHC," *Eur. Phys. J.*, vol. C63, pp. 189–285, 2009.

[108] A. Malik et al., "Search for a heavy top partner decaying in b+chargino in final states with two leptons using a multivariate analysis technique," 2015. [Online]. Available: http://cds.cern.ch/record/2032460

BIOGRAPHICAL STATEMENT

Smita Darmora was born in Garhwal region of Himalaya, India. She received her Master of Science in Physics from Garhwal University. She further studied at the Indian Institute of Technology, Roorkee and earned her M.Phil. in Physics with specialization in Instrumentation. After receiving her masters degree she worked at Indian Institute of Petroleum, Dehradun.

In fall 2008, Smita started her Ph.D programme in Physics at The University of Texas at Arlington. Her research work focuses on Supersymmetry. For her dissertation, she worked in the ATLAS experiment at CERN, Geneva, from March, 2011 to April 2015. At CERN, she was involved with the TileCal and the SUSY group. She wishes to continue her work in the field of experimental high energy physics.